Tuning the viscoelasticity of *Escherichia coli* biofilms:

interplay between extrinsic and intrinsic factors

Adrien Sarlet

Univ.-Diss.

zur Erlangung des akademischen Grades

"doctor rerum naturalium"

(Dr. rer. nat.)

in der Wissenschaftsdisziplin Biochemie

eingereicht an der

Mathematisch-Naturwissenschaftlichen Fakultät

Institut für Biochemie und Biologie

der Universität Potsdam

Ort und Tag der Disputation:

Potsdam, 06.07.2023

Hauptbetreuerin: Prof. Dr. Kerstin Blank

Betreuerinnen: Dr. Cécile Bidan, Prof. Dr. Kerstin Blank

Gutachter*innen: Prof. Dr. Kerstin Blank, Prof. Dr. Salvatore Chiantia, Prof. Dr. Matthew Harrington

Abstract

Biofilms are heterogeneous structures made of microorganisms embedded in a self-secreted extracellular matrix. Because they cause complications in various fields of human life, most research has focused on the development of preventive anti-biofilm strategies. Recently, biofilms have been studied as sustainable living materials with a focus on tuning their mechanical properties. While this can be achieved by means of genetic engineering, regulations regarding genetically modified organisms restrict possible applications outside the lab. Alternative ways of controlling their materials properties are therefore desirable. Since biofilm formation is a defence mechanism against unfavourable conditions, the environment can in turn be leveraged to influence biofilm properties. In particular, their matrix is known to sequestrate metal ions to protect bacteria against toxicity. As a side effect, biofilms stiffen in presence of some metal cations and soften in presence of others. The specificity and the molecular determinants of cation-biofilm interactions vary between species. While *Escherichia coli* is a widely studied model organism, little is known concerning the interaction of *E. coli* biofilms with metal ions as well as possible consequences on biofilm properties. In this work, my aim was to tune the mechanical properties, specifically the viscoelasticity, of *E. coli* biofilms by acting on extrinsic and intrinsic factors.

To do so, I used *E. coli* strains that produce a matrix composed of curli amyloid and/or phosphoethanolamine-cellulose (pEtN-cellulose) fibres. The viscoelastic behaviour of the resulting biofilms was investigated with rheology. For each matrix composition, four metal salt solutions were tested against ultrapure water: $FeCl_3$, $AlCl_3$, $ZnCl_2$ and $CaCl_2$. Biofilms were grown on nutritive agar substrates for one week, harvested and mixed and incubated with one of the solutions or ultrapure water. Scraping the biofilms from the agar as well as mixing led to a partial destruction of the biofilm matrix architecture. Shear strain amplitude showed that the strain producing both fibres stiffened by a factor of two when exposed to the trivalent metal cations Al(III) and Fe(III) while no such response was observed for the bivalent cations Zn(II) and Ca(II). Strains producing only one matrix component did not show any stiffening in response to either cation, but even a small softening. Attempts to

reconstitute the matrix by co-culturing two strains, each producing one type of fibre, or by simply mixing them after biofilm growth did not yield any stiffening response.

As mixing may destroy the macroscopic architecture of the biofilm matrix and, therefore, affect the viscoelastic properties, rheology was compared to a non-destructive mechanical method to assess biofilm properties. In order to investigate further the contribution of each matrix component, also additional bacterial strains were introduced. These strains produce curli fibres in combination with non-modified cellulose, non-modified cellulose only or neither component. For rheology, biofilms were mixed but no solution was added. As a non-destructive method, microindentation was performed for the same strains, using biofilms in their native state and on their agar substrate. This allowed for a systematic comparison of the shear moduli obtained with rheology and the compressive moduli obtained with microindentation. Microindentation showed that biofilm stiffness is mainly determined by the presence of curli amyloid fibres. Such a clear distinction between biofilm matrices with and without curli was not seen with rheology, i.e. after homogenization and partial destruction of the matrix architecture. The comparison further suggests that curli fibres are more brittle and are thus more affected by biofilm homogenization. In light of these results, the magnitude of cation induced stiffening (or softening) may have to be reassessed, performing similar experiments on native biofilms.

To examine the molecular interactions between biofilms and metal cations, attenuated total reflectance - Fourier transform infrared spectroscopy (ATR-FTIR) was applied to the *E.coli* strains producing a matrix composed of curli amyloid and/or pEtN-cellulose fibres. Biofilms were measured in presence of each of the aforementioned metal cation solutions or ultrapure water. In the absence of metal cations, the spectra of three strains cannot be distinguished, suggesting that the spectra result from the bacteria rather than the matrices. In the presence of metal cations, a possible non-specific effect of the cations on lipids, i.e. bacterial membranes, was observed for the strain that does not produce pEtN-cellulose. Subsequently, ATR-FTIR experiments were performed on fibres purified from the strains producing only one type of fibres. No significant spectral differences were

seen when curli amyloid fibres were mixed with metal cations. Also, no indications were found for a possible effect of metal cations on the secondary structure of curli fibers. The spectra of the pEtN-cellulose fibres revealed an interaction between metal cations and the phosphate of the pEtN-modification. This negatively charged group on pEtN-cellulose is therefore a potential site for non-specific metal adsorption in the biofilm matrix. Notably, a NaCl control solution did not show a similar effect. The possible adsorption of metal cations on pEtN-cellulose may allow for counter-ion condensation along those fibres. For both bivalent and trivalent cations, Manning's criterion is verified while this is not the case for monovalent cations.

Further research is necessary to understand the role of curli amyloid fibres. Other amyloid structures are known to bind metal cations and metal complexation could explain the valence specificity observed at the rheology level. Rheology has also shown that stiffening requires both fibres to be produced by the same bacterium. This suggests that both fibres simultaneously interact with the same metal cation. More generally, this works underlines the possibility of tuning biofilm mechanics without the need for genetic engineering. Moreover, it emphasises the specific contributions of different matrix components, highlighting the importance of studying biofilms produced by different strains and species.

Table of contents

List of figures and tables

List of abbreviations

Aβ	:	Amyloid beta
AFM	:	Atomic force microscopy
A. lwoffii	:	*Acinetobacter lwoffii*
AP329	:	*E. coli* strain producing pEtN-cellulose
AP470	:	*E. coli* strain producing amyloid curli and non-modified cellulose
AP472	:	*E. coli* strain producing non-modified cellulose
AR198	:	*E. coli* strain producing neither amyloid curli nor cellulose
AR3110	:	*E. coli* strain producing pEtN-cellulose and amyloid curli
ATR-FTIR	:	Attenuated total reflectance - Fourier transform infrared spectroscopy
A. vinelandii	:	*Azotobacter vinelandii*
B. subtilis	:	*Bacillus subtilis*
c-di-GMP	:	Bis-(3'-5')-cyclic dimeric guanosine monophosphate
DOPA	:	Dihydroxyphenylalanine
E	:	Young's modulus
E. asburiae	:	*Enterobacter asburiae*
E. coli	:	*Escherichia coli*
EDTA	:	Ethylenediaminetetraacetic acid
EPS	:	Extracellular polymeric substance
FTIR	:	Fourier transform infrared spectroscopy
FWHH	:	Full width at half height
G'	:	Storage modulus
G'_0	:	Plateau value of the storage modulus
G"	:	Loss modulus
$G"_0$	:	Plateau value of the loss modulus
IQR	:	Interquartile range
IR	:	Infrared
K. pneumoniae	:	*Klebsiella pneumoniae*
LVE	:	Linear viscoelastic range
MSD	:	Mean-squared displacement
NMR	:	Nuclear magnetic resonance
OD	:	Optical density
P. aeruginosa	:	*Pseudomonas aeruginosa*
pEtN-cellulose	:	Phosphoethanolamine-modified cellulose

P. fluorescens	:	*Pseudomonas fluorescens*
P. putida	:	*Pseudomonas putida*
Re	:	Reynolds number
SDS	:	Sodium dodecyl sulfate
S. aureus	:	*Staphylococcus aureus*
S. epidermidis	:	*Staphylococcus epidermis*
SMFS	:	Single-molecule force spectroscopy
S. mutans	:	*Streptococcus mutans*
S. pyogenes	:	*Streptococcus pyogenes*
TFF	:	Human trefoil factor
Tris	:	Tris(hydroxymethyl)aminomethane
V. cholerae	:	*Vibrio cholerae*
W3110	:	*E. coli* strain producing amyloid curli
γ_F	:	Flow strain
γ_Y	:	Yield strain
τ_F	:	Flow stress
τ_Y	:	Yield stress

1. Introduction

Biofilms are heterogeneous structures made of microorganisms embedded in a self-secreted extracellular matrix. While biofilms can be produced by eukaryotic cells such as fungi[1,2], they are particularly predominant in prokaryotic organisms, where they are thought to represent the main form of active life[3]. Biofilms cause complications in various fields of human life, e.g. in the medical sector[4], the food[5] and the oil[6] industries . At first, most biofilm research focused on the development of preventive anti-biofilm strategies. More recently, biofilms have emerged as a potential source of sustainable materials. For example, biofilms were utilized for the formation of cement-like glue[7], aquaplastics[8] or 3D-printed living materials[9]. The composition of the biofilm matrix and the interaction between matrix components critically determines its mechanical properties. The matrix mainly consists of polysaccharides[10], proteins[11] and nucleic acids[12]. The type of protein and polysaccharide as well as their proportion vary remarkably, both between genera and between different species within the same genus[13]. Protein-based amyloid fibres are particularly widespread in microbial biofilms and were, for example, observed in *Pseudomonas sp.*, *Bacillus sp.* and in *Escherichia coli* biofilms, where they are referred to as curli fibres[14]. Curli fibres, encoded by the *csgBA* operon, are composed of several CsgA units that polymerise onto the CsgB nucleator protein[15]. In *E. coli* biofilms, which will be at the core of this work, the second main component of the matrix is phosphoethanolamine-modified cellulose (pEtN-cellulose)[16]. The matrix of the biofilm-forming *E. coli* K-12 strain AR3110 was estimated to contain 75% curli and 25% pEtN-cellulose[17].

Since biofilms are more and more regarded as materials *per se*, tuning their mechanics has recently become a field of interest. In addition to the matrix composition, environmental factors also influence the mechanical properties of biofilms. For instance, substrate water content, temperature, pH and nutrients may be utilized as possible control parameters for tuning *E. coli* biofilm properties during their growth[18,19]. Another possible leverage is the addition of specific metal ions. Metal ions frequently bind to protein or carbohydrate structures in biological materials[20], either forming mineralized composite materials[21–24] or sacrificial and self-healing bonds[25,26]. Bacterial biofilms

frequently occur in metallic pipes or at the surface of heavy metal containing wastewaters, suggesting a possible influence of metal ions on biofilm growth and properties. For *Enterobacter asburiae*, *Vitreoscilla sp.* and *Acinetobacter lwoffii*, metal ions promote biofilm formation[27]. In the case of *Staphylococcus epidermidis, Bacillus subtilis* and *Pseudomonas aeruginosa,* biofilms stiffen in the presence of metal cations[28]. Specifically, *B. subtilis* biofilms stiffen and erode slower in presence of Fe(III) and Cu(II)[29].

E. coli is one of the best studied model organisms. The composition and architecture of its matrix have at least partially been determined. However, while the influence of metal ions has been extensively studied in other species, very little is known for *E. coli* biofilms. The only documented effect is the triggering of rugose biofilm formation, visually characterised by a more wrinkled phenotype, in the presence of $FeCl_3$[30]. With the aim of altering biofilm properties, there is a clear lack of knowledge about how the addition of metal ions affects *E. coli* biofilms. This includes the influence of metal ions on matrix mechanics and the molecular interactions involved. The aim of my doctoral thesis is to fill this gap by studying the influence of metal cations on the viscoelastic properties of *E. coli* biofilms. To fully understand the role of cation-matrix interactions, this work will also investigate how the viscoelastic properties are influenced by matrix composition and biofilm macroscopic architecture. Finally, I will attempt to explain the macroscopic effects of metal cations on biofilm viscoelasticity at a molecular level.

2. State of the art

2.1. Biofilms as living materials

A biofilm can be defined as a population of microorganisms embedded in a self-secreted extracellular matrix. Biofilms represent the main form of active prokaryotic life[3]. Yet, reducing biofilm forming organisms to the sole domain of bacteria would be erroneous. Biofilms are almost as ancient and as varied as life itself. Stromatolites and other forms of microbialites are the oldest fossils found on Earth, some of which being more than one billion years old[31]. Nowadays, biofilm forming organisms are found in the eukaryotic domain, e.g. algae[32] and fungi[1,2]; in the archaeal domain; and in the bacterial domain, as will be described further on.

The diversity in biofilm forming bacteria is high. The Biofilms Structural Database, a collection of data relevant to the understanding of biofilm formation currently includes information from 42 bacterial species[33]. Among bacteria negatively impacting human health, species such as *Enterococcus faecalis*, *Escherichia coli*, *Klebsiella pneumoniae*, *Proteus mirabilis*, *Pseudomonas aeruginosa*, *Staphylococcus aureus*, *Staphylococcus epidermidis* and *Streptococcus viridans* have been shown to form biofilms on medical devices[34]. In addition, more than 60% of the microbial load on human skin is made of biofilm forming bacteria[35]. The proportion of biofilm producing bacteria appears to be high also in other sectors of human activities: ten different bacterial species possessing genes associated with biofilms could be isolated in a meat factory[36]. All things considered, 40 to 80% of prokaryotic cells on Earth are estimated to reside in biofilms[3].

This variety of biofilm-forming species results in a variety of matrix components. Polysaccharides are one of the two main types of matrix fibres. They serve multiple roles, such as aggregating the bacteria by acting as a glue, enhancing adhesion to the substrate, protecting the cells against environmental stresses or providing structure to the biofilm. One commonly found polysaccharide is alginate, present in *Pseudomonas aeruginosa* and *Azotobacter vinelandii*. Levan, another common polysaccharide, is found in *Pseudomonas syringae*, *Bacillus subtilis* and *Streptococcus mutans*[10]. Similarly, protein fibres often play a structural role but are also involved in adhesion or protection.

They can be divided between amyloid forming and non-forming protein fibres. Amyloid fibres are characterised by a cross-β structure and bind the dyes Congo red and thioflavin T. They include amyloid-like curli fibres found in *Enterobacteriaceae* such as *E. coli* and *Salmonella*, Fap fibres found in *P. aeruginosa*, *putida* and *fluorescens* as well as the phenol-soluble modulins from *S. epidermis* and *aureus*. Non-amyloids include the pili of *Mycobacterium tuberculosis*[14]. In addition to fibres, biofilm matrices also contain other proteins that do not form fibres as well as lipids and extracellular DNA.

2.2. Model organisms

Within the great diversity of biofilm producing bacteria, a few species have been studied in depth and are now considered as model organisms. In addition to *E. coli*, two will be introduced here since the properties of their biofilms will later be compared to the *E. coil* biofilms investigated in this work.

2.2.1. Bacillus subtilis

Bacillus subtilis is a Gram-positive soil dwelling bacterium. Research conducted on *B. subtilis* was key to understanding biofilm assembly[37]. As will be exemplified in later sections, the mechanical properties of *B. subtilis* biofilms were also thoroughly investigated. The polysaccharides composing its matrix are levan, a polymer of fructose, as well as the products of the *eps* operon, whose monosaccharidic composition is elusive[37]. The main protein component is made of fibres formed by TasA and TapA as a minor component. Their amyloid nature is still debated[14]. Another component of the matrix is the hydrophobin BaslA. The aforementioned matrix composition corresponds to the NCIB 3610 *B. subtilis* strain. Another strain, B-1, produces a matrix containing mainly gamma-polyglutamate[38].

2.2.2. Pseudomonas aeruginosa

Pseudomonas aeruginosa is a Gram-negative bacterium, known for forming biofilm infections in the lung of cystic fibrosis patients[39]. The matrix of *P. aeruginosa* biofilms contains the amyloid-like protein Fap as well as DNA. It also contains several polysaccharides: alginate, an acetylated polymer containing L-guluronic and D-mannuronic acids[13]; Pel, composed of cationic amino sugars including

N-acetylgalactosamine and *N*-acetylglucosamine[40]; and the pentasaccharide Psl, containing D-mannose, D-glucose and L-rhamnose monomers. In cystic fibrosis patients, polysaccharide production can vary, thereby influencing the mechanics of the biofilms[39].

2.2.3. Escherichia coli

Escherichia coli is a commensal aero-anaerobic Gram-negative bacterium present in the vertebrate gut[41]. The non-pathogenic K-12 strain of *E. coli* was first isolated from the faeces of a diphtheria patient in 1922 and has been studied in laboratories ever since[42]. This *E. coli* strain was among the first prokaryotic genomes to be completely sequenced as early as 1997[43]. Two other common *E. coli* laboratory strains, MG1655 and W3110, derive from K-12 but differ in having lost the fertility factor F and the phage λ (F-λ-)[44]. W3110 is capable of forming biofilms and produces a matrix mainly composed of curli amyloid fibres encoded by the *csgBAC* operon[45] (Figure 1A). W3110 has lost the ability to produce cellulose, otherwise encoded in the *yhjR-bcsQABZC* operon (Figure 1B). This function was restored when changing the codon 6 of *bcsQ* from TAG(stop) to TTG(leucine), thereby yielding the strain AR3110[46]. It was later shown that the cellulose is modified into pEtN-cellulose by the *bcsEFG* operon. Approximately half of the glucose residues are esterified on their carbon 6[16]. The W3110-based AR3110 strain thus produces both curli amyloid fibres and pEtN-cellulose. To obtain a strain that produces only pEtN-cellulose, curli production was inactivated in the strain AP329 (AR3110ΔcsgBA)[16]. The strains W3110, AR3110 and AP329 will be at the core of this work. Other sub-strains will be introduced when necessary.

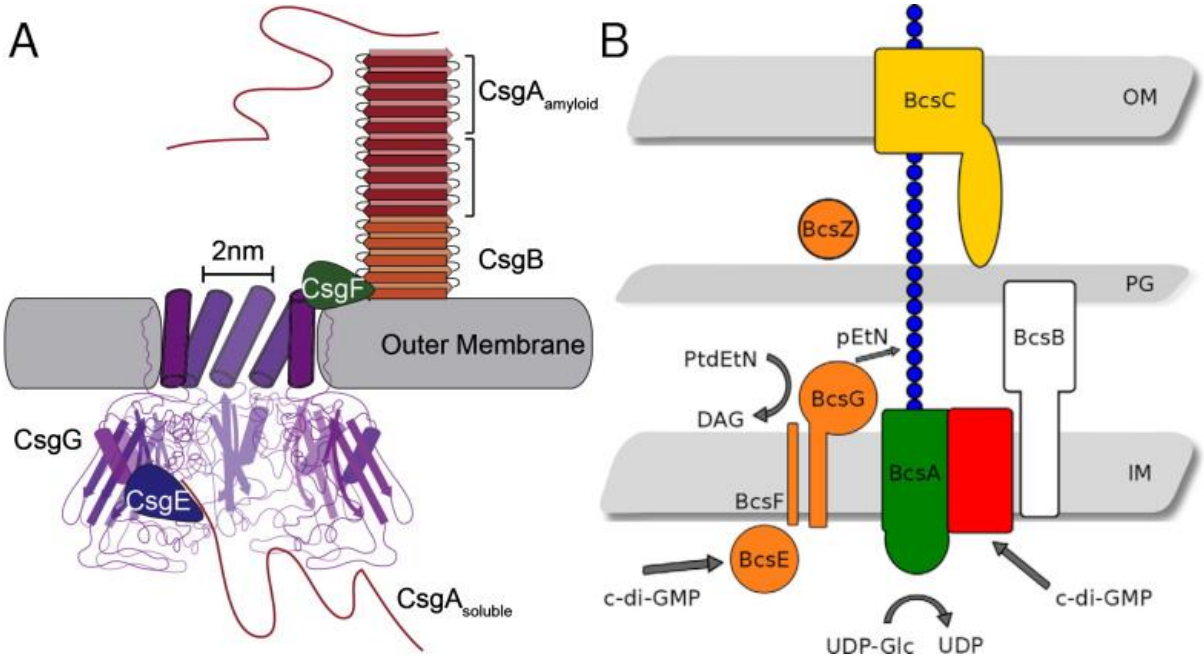

Figure 1. Production of key matrix fibres in *E. coli* biofilms. A: Model of the curli secretion apparatus[47]. CsgA subunits form amyloid fibres by polymerizing onto CsgB. CsgG forms a pore in the outer membrane. CsgE and CsgF interact directly with CsgG. CsgE directs the soluble CsgA into the pore while CsgF is required for amyloid fibre assembly. (Reprinted from Biochimica et Biophysica Acta (BBA) - Molecular Cell Research, 1843, Margery L. Evans, Matthew R. Chapman, Curli biogenesis: Order out of disorder, 1551-1558, Copyright (2014), with permission from Elsevier). B: Model representing the different Bcs proteins involved in cellulose synthesis, export and pEtN-modification. BcsA and BcsB form the channel. BcsG is thought to be involved in the pEtN-modification. The cytoplasmic BcsE binds c-di-GMP and interacts with BcsG via BcsF. BcsC could release the cellulose polymer through the outer membrane following hydrolysis by BcsZ[48]. (Reprinted under Creative Commons BY 4.0 licence).

The curli and cellulose operons are under the control of the transcriptional regulator CsgD[45], sometimes referred to as the master regulator of biofilm formation in *E. coli*[49]. In turn, CsgD allows for the integration of various environmental influences on biofilm formation. For instance, *csgD* expression is modulated in response to osmolarity by the interplay between EnvZ/OmpR and Cpx (high salt content medium) and by H-NS (high sucrose content). However, other environmental factors act upstream (e.g. oxidative stress is integrated via the sRNA ArcZ acting on *rpoS* coding for σS[50]) or downstream (e.g. temperature is integrated by Crl, a low-temperature induced protein promoting σS binding to the *csgBA* promoter[51]).

Curli fibres are composed of the minor subunit CsgB that acts as the nucleator for the polymerization of multiple CsgA major subunits. In absence of CsgB, CsgA are secreted but do not polymerize[15]. The *csgDEFG* operon is involved in the regulation and secretion of curli fibres. CsgG forms a pore-like structure while CsgE and CsgF play chaperone-like functions[47]. CsgA and CsgB share 30% sequence

identity[15], similar dimensions and structure. A β-helix with five repeated strand-loop-strand motifs forms the amyloid core and is preceded by a 22-residue unstructured tail at the N-terminus[52]. Curli fibres bind the amyloid specific dye thioflavin T[47]. They play a role in adhesion to eukaryotic cells and more generally in pathogenesis[15]. They can therefore be referred to as functional amyloids.

BcsA and BcsB form a channel for the co-synthetic secretion of cellulose[16]. The *bcsEFG* operon is responsible for the pEtN-modification. *bcsG* is indispensable and BcsG is probably directly involved in this natural modification of cellulose. BcsF shows strong interactions with BcsE and BcsG. BcsE is cytoplasmic and binds bis-(3'-5')-cyclic dimeric guanosine monophosphate (c-di-GMP), a signal transduction and regulation second messenger in bacteria[16,45]. A proposed pathway suggests that BcsF serves as a transmembrane connector between c-di-GMP-controlled BcsE and BcsG, which is responsible for the pEtN-modification[16].

Different matrix compositions, i.e. curli amyloid fibres (W3110), pEtN-cellulose (AP329) or both (AR3110), result in different macroscopic biofilm architectures. The most elaborated architecture is observed for the strain producing both fibres (AR3110). Between ridges (Figure 2A), the biofilm is approximately 60 µm thick and is divided vertically in two layers (Figure 2B). The fluorescence of thioflavin S, which indicates the presence of cellulose and curli, is intense in the top layer (40-50 µm) but absent in the bottom layer (20 µm). The top layer itself is divided vertically in three zones. A surface zone where the bacteria are encased in a pEtN-cellulose-curli composite matrix, a middle zone with vertical pillars of bacteria that are stabilised by pEtN-cellulose filaments forming a sheath and a lower zone mostly composed of horizontal chains of bacteria. The bottom layer is mainly composed of flagellated growing cells[46,50,53,54]. Ridges are made of a double layer that buckled up in the outer region of the biofilm. They are absent for colonies lacking pEtN-cellulose, curli or both. The macroscopic biofilm phenotypes further differ among strains lacking one or both types of fibres. For the strain producing pEtN-cellulose and no curli, small intertwined wrinkles are present in the centre of the biofilm[46]. On the other hand, when curli is produced in the absence of cellulose, the biofilm exhibits concentric rings[55]. At the cellular scale, the organisation of the fibres differs even more

between the two mutant strains. In the strain producing only cellulose, filaments of cellulose are observed, parallel to each other and perpendicular to the wrinkle line[53]. When only curli are present, the biofilm top layer is composed of small cells tightly surrounded in a "*honeycomb-like network*" of curli fibres[53].

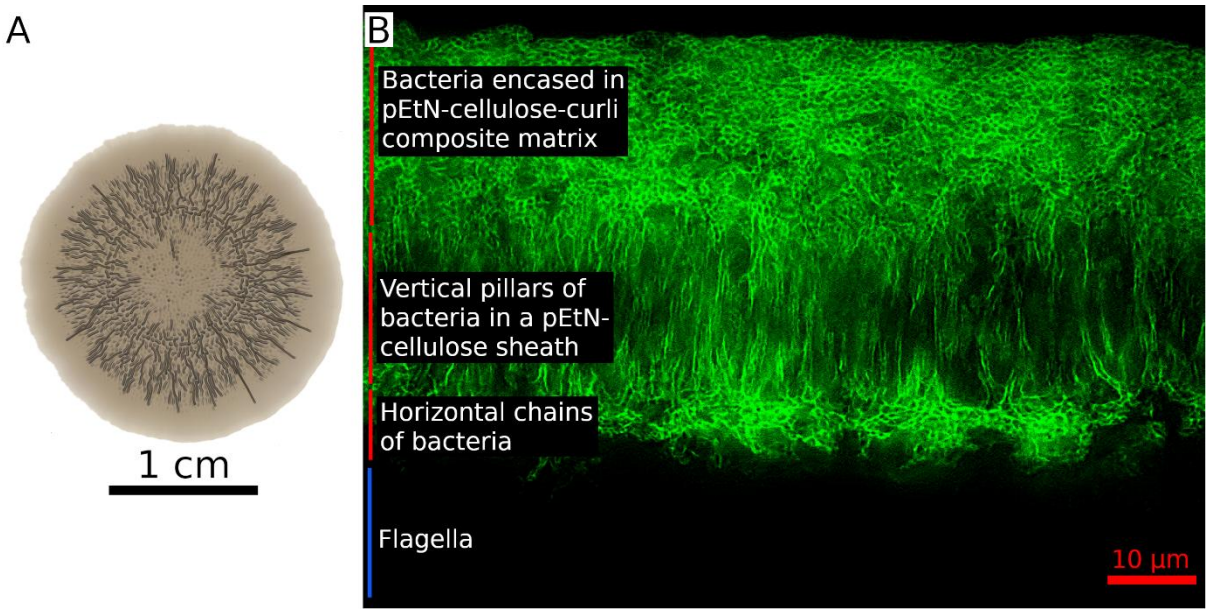

Figure 2. Phenotype of an *E. coli* AR3110 biofilm. A: Top view of the biofilm, grown for 5 days, at 28°C and on salt-free LB agar. Radial ridges are visible as well as the ring delimiting the central region. B: Vertical cross-section in the central region of a biofilm, grown for 5 days, at 28°C and on salt-free LB agar containing. The biofilm was stained with thioflavin S. The top layer is subdivided in three zones (red bars). In the surface zone, cells are embedded in a pEtN-cellulose-curli composite. The middle zone contains vertical pillars of cells, stabilised by pEtN-cellulose filaments. The lower zone contains horizontal chains of bacteria. The bottom layer contains mainly flagellated cells and does not bind thioflavin S. (Adapted from Klauck et al. 2018[54], reprinted under Creative Commons BY 4.0 licence).

2.3. Methods for biofilm characterization

Numerous methods have been used to investigate biofilm properties. Some of them will be introduced here with a stronger focus on the methods that are relevant to this work. Mechanical methods will be introduced first, followed by spectroscopy. The examples provided for each method will concern biofilm materials, although each method has a much wider area of application than biofilm studies.

2.3.1. Rheology

Whether they grow inside of biological cavities, such as the respiratory or the digestive track, or at the inner surface of pipes, biofilms frequently encounter shear forces. The science that studies the

deformation of a material in response to shear is rheology. Formally, the term *rheology* refers to the science itself, while the term *rheometry* refers to the experimental measurement methods. However, for the sake of simplicity, and as is often the case in practice, both will be indistinctly referred to as *rheology* in this work.

Rotational rheometers can be operated either in continuous or oscillatory rotation mode. When controlling the frequency of the oscillation, the viscoelastic properties of a material can be probed. They are usually expressed in the form of a storage modulus (G'), representing the elastic contribution, and the loss modulus (G''), accounting for the viscous contribution. The ability of oscillatory rheology to directly provide both viscoelastic moduli of a material comes with the limitation of measuring them only in bulk. In addition, when applied to biofilms, the sample preparation often involves scraping the biofilms from their substrate or removing them from a liquid interface, thereby potentially destroying their microscale matrix architecture[28]. Nevertheless, rotational rheology has been applied to biofilms produced by various bacterial species as diverse as *Pseudomonas spp.*[56], *A. vinelandii*[57], *S. mutans*[58] and *Vibrio cholerae*[59]. One way to circumvent the partial destruction of the matrix architecture is to grow the biofilms directly on the rheometer stage, as was demonstrated for several strains of *B. subtilis* and *S. epidermidis* [60,61]. Capillary peeling was recently introduced as a method to transfer an intact *V. cholerae* biofilm from its growth surface onto another surface, e.g. a rheometer stage[59]. When performing oscillatory rheology, the influence of the matrix composition[38] or expression level[39] on the mechanical properties of the biofilm can be investigated, as well as the effect of chemical perturbations[56,57]. Beyond oscillatory rheology, a rheometer was also used to measure biofilm adhesion to surfaces[61] and interfacial rheology was used to investigate the mechanical properties of biofilms at the air-liquid interface[19,62].

The lack of local information provided by bulk rheology as well as the partially destructive nature of the method can be overcome when using microrheology. Microrheology itself can be subdivided into passive and active microrheology. Passive microrheology involves tracking the position of microparticles added to the biofilm prior to or during growth. Also referred to as particle tracking,

the technique enables probing of biofilms at an early growth stage and at small length scales. The particles are driven by thermal energy and undergo Brownian motion. From their random trajectories, a mean-squared displacement (MSD) can be computed. The MSD is inversely proportional to the shear modulus of the environment[63]. However, this method is only suitable for soft (Table 1) biofilms[28]. Particle tracking was used to measure the viscoelastic properties in biofilms produced by *S. aureus*, *P. aeruginosa*[64] and *S. mutans* biofilms[65]. In order to probe viscoelastic properties of stiffer materials (Table 1), larger forces need to be applied and active microrheology becomes necessary. When actively applying a force on the microparticles, specific spatial points can be targeted. When using magnetic tweezers for particle actuation, the penetration depth of the magnetic field is the main limitation[28]. Magnetic tweezers were used to map the viscoelastic parameters of *E. coli* biofilms in three dimensions[66] (Figure 3). Alternately, optical tweezers can be used to apply a force on microparticles. This was used to measure the local viscoelasticity of levan-DNA mixtures, important components of biofilm matrices produced by various species[67].

Table 1. Overview of different microrheology techniques used for the characterization of biofilms[63].

Technique	Frequency range (Hz)	Shear modulus range (Pa)
Particle tracking	10^{0} - 10^{2}	10^{-5} - 10^{0}
Optical tweezers	10^{-1} - 10^{4}	10^{-3} - 10^{2}
Magnetic tweezers	10^{-2} - 10^{3}	10^{-3} - 10^{4}

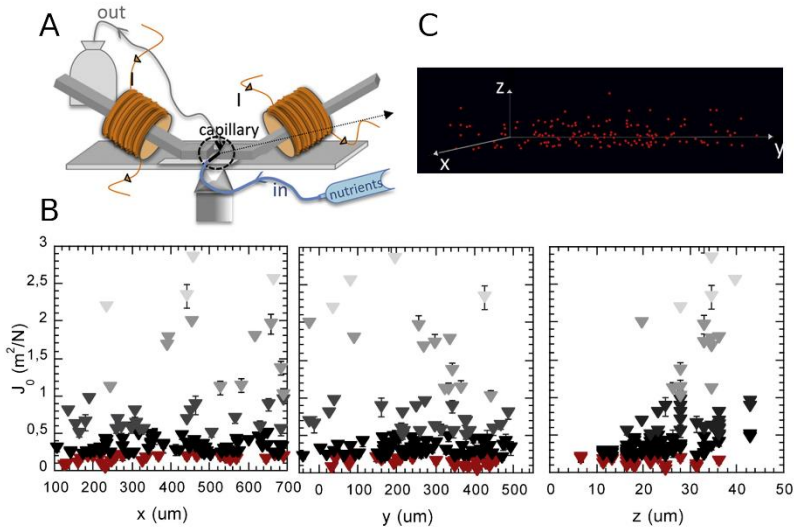

Figure 3. Magnetic tweezers-based microrheology to three-dimensionally map the elastic compliance of biofilms produced by *E. coli* MG1655. The biofilms were grown in a capillary under 1 mL h^{-1} nutrient flow, for 24 h and at 37°C. A: Capillary between the tweezers (black circle). The whole set-up is mounted on a microscope stage. B: Compliance mapped in three dimensions. The error bars represent twice the standard error of the mean. C: Three-dimensional view of the particle distribution. (The three parts of the figure were reprinted from Biophysical Journal, 103, Olivier Galy, Patricia Latour-Lambert, Kais Zrelli, Jean-Marc Ghigo, Christophe Beloin, Nelly Henry, Mapping of Bacterial Biofilm Local Mechanics by Magnetic Microparticle Actuation, 1400-1408, Copyright (2012), with permission from Elsevier).

2.3.2. Indentation

Just as a rheometer is used to investigate the relation between shear stress and shear strain, an indenter can be used to investigate the relation between compressive stress and strain, or between tensile stress and strain in case of adhesion of the probed material to the indenter. The corresponding elastic modulus is the Young's modulus (E). Depending on the size of the indenting tip, the method is referred to as micro- or nanoindentation. In both cases, an indenter locally compresses the material and the force acting on the indenter (ultimately providing a stress) is recorded together with its position (ultimately providing a strain).

Using microindentation, the cohesive strength was measured for *P. aeruginosa* biofilms[68] and tensile strength for *S. mutans* biofilms[69]. More generally, microcantilevers can be used to manipulate biofilms and derive mechanical properties also without indentation. This can be referred to as micromanipulation[28]. The strength of adhesion to a glass surface was investigated for *P. fluorescens* biofilms with a specially designed T-shaped cantilever[70]. In this case, the biofilm was pulled away from the surface rather than indented. Adhesive strength was investigated for *P. aeruginosa* and

S. epidermis biofilms submersed in liquid. The biofilms were pulled away from their support by suction through a capillary mounted on a micro-cantilever[71]. In each case, the set-up was custom-made.

Nanoindentation with an atomic force microscope (AFM) was also used for various biofilm-forming bacteria species to investigate the mechanical properties both of the biofilm and of the bacteria themselves. Mechanical properties of single bacteria were measured via nanoindentation for *P. aeruginosa*[72]. Viscoelastic properties were mapped for biofilms produced by *S. epidermis*[73] and *E. coli*[74]. AFM can further be used for single-molecule force spectroscopy (SMFS) and has been employed to study the mechanical properties of *E. coli* type I pili[75]. Furthermore, the bond between the adhesive *E. coli* type I Frimbriae subunit FimH and its mannose ligand was also probed with SMFS[76].

2.3.3. Fourier transform infrared spectroscopy

Fourier transform infrared spectroscopy (FTIR) is a technique that probes molecular vibrations. It associates functional groups with characteristic infrared (IR) absorption bands corresponding to their fundamental vibrations. The IR absorbance spectrum of a sample is a fingerprint of its chemical composition. Given a nonlinear molecule with n atoms, there are 3n-6 normal modes, i.e. fundamental vibrations. Yet, a normal mode absorbs incident IR light only if there is a change in the dipole moment of the molecule. This means that only asymmetric vibrations are IR active. Almost all chemical groups in a sample can be probed. However, the strongest absorptions are measured for groups with a permanent dipole[77]. The vibration frequency depends on the mass of the atoms involved in the bond and thus informs about the nature of the functional group. The frequency is also sensitive to the electronegativity of the neighbouring atoms as well as to hydrogen bonding. It thereby provides information about the environment of the group[77]. FTIR is non-perturbative, non-destructive, relatively inexpensive and quick to implement[78]. It possesses a high discriminating

power and can be used for bacterial strain typing in place of whole genome sequencing. In that case, FTIR has the additional advantage of analysing the presence of biochemical markers[78,79].

Three different types of spectral acquisition can be distinguished for microbial samples[78]. Attenuated total reflectance (ATR) makes use of a totally reflecting prism, onto which the samples are placed. An evanescent IR wave is generated, goes through the sample obliquely and is reflected back to the detector. This method is suitable for suspended cultures or biofilms with a smooth surface. It requires minimal sample preparation, is low-cost and has little sample thickness restrictions. However, it has a low throughput with only one spectrum per data acquisition. Considering that the biofilm has to be placed on the prism, samples are often homogenized so that the method cannot account for biofilm architecture or heterogeneity[78]. The second acquisition method is diffuse reflectance. It is suitable for samples producing high levels of scattering. Such samples are for instance freeze-dried, powdered or finely ground samples. The method has a high throughput but the cost is relatively high. The last acquisition method is the transmittance mode. It has a high signal-to-noise ratio, although lower than ATR. Unlike ATR, this method can provide spatial resolution, performing as a type of microscopy that yields spectral maps[78].

A major use of FTIR for biofilms is the study of the extracellular matrix composition. FTIR spectra of biofilm extracellular polymeric substance (EPS) produced by *P. fluorescens*, *A. lwoffii*, *Vitreoscilla sp*. and *K. pneumoniae* were measured and showed a dominant protein content, along with a high content of polysaccharides and small amounts of lipids[27]. In several species of *Streptococci* biofilms, FTIR spectra were compared and mapped for several chemical groups[80]. For a combination of *Enterobacter sp.* and *Aspergillus sp.*, FTIR was used to compare the composition of fungal-bacterial, fungal-only and bacterial-only biofilms[81]. In addition, the evolution of biofilm composition under the influence of environmental factors can be assessed. Using FTIR, the effect of temperature on matrix production was investigated for biofilms produced by *Salmonella enterica* serotype Virchow, containing both cellulose and curli fibres[82]. ATR-FTIR was also used to detect the presence of biofilms at the surface of composite-coated iron with the aim of determining whether the composite could

inhibit biofouling[83]. ATR-FTIR was further used to monitor time-resolved changes in carbohydrates, protein and DNA composition when exposing *E. coli* biofilms to zosteric acid, a possible inhibitor of biofilm formation[84]. Most importantly, FTIR allows to resolve specific components within the biofilm. For biofilms produced by a uropathogenic *E. coli* strain, the structure of Dr fimbriae, one type of adhesins, was characterized[85]. Finally, FTIR can also be used to study metal complexation. For *E. coli* biofilms, the functional groups interacting with Fe(III), Cd(II), Ni(II) and Cr(VI) were investigated with FTIR[86] (Figure 4).

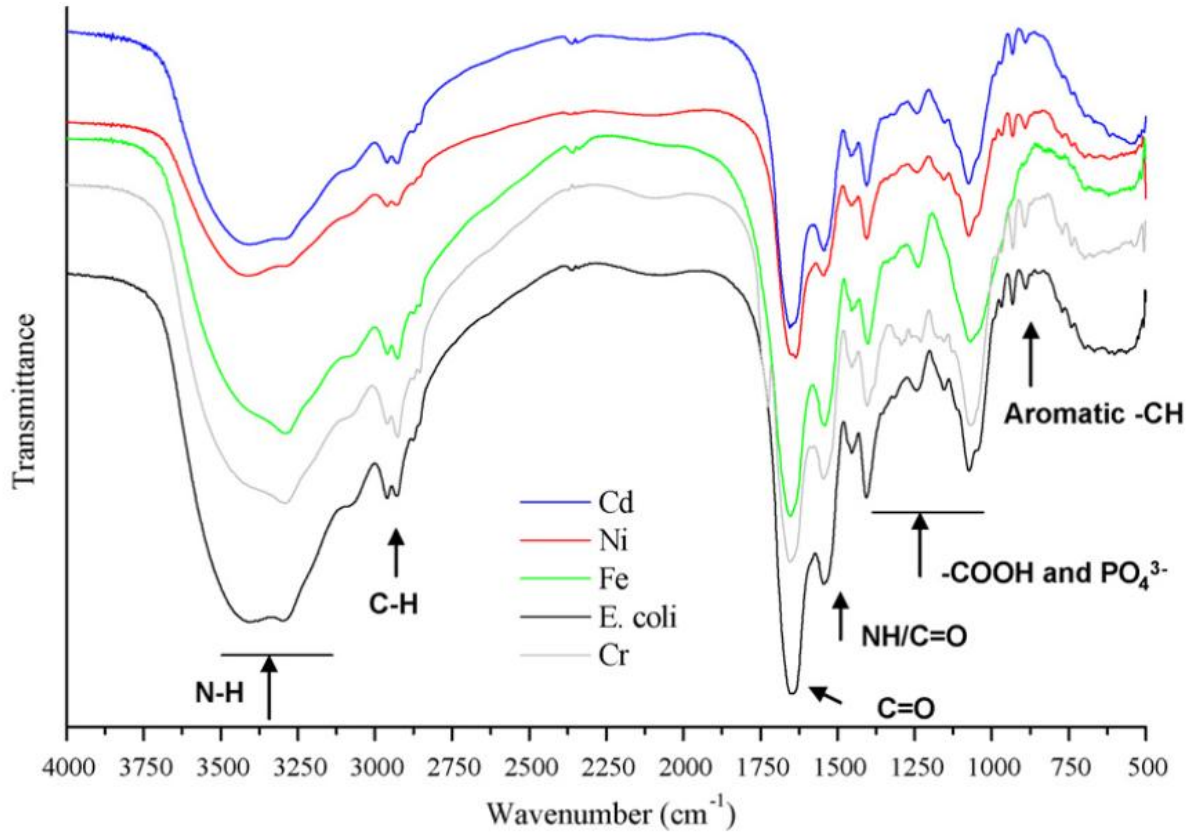

Figure 4. FTIR spectra of an *E. coli* biofilm grown on kaolin and with and without incubation with metal cations. The biofilms were harvested, centrifuged, dried and ground into a sample disk prior to the FTIR measurements. The peaks affected by the metal cations are indicated with arrows and identified based on the literature. (Reprinted from Chemical Engineering Journal, 149, Cristina Quintelas, Zélia Rocha, Bruna Silva, Bruna Fonseca, Hugo Figueiredo, Teresa Tavares, Removal of Cd(II), Cr(VI), Fe(III) and Ni(II) from aqueous solutions by an *E. coli* biofilm supported on kaolin, 319-324, Copyright (2009), with permission from Elsevier)

FTIR has also been used to investigate metal complexation by amyloids or cellulose, i.e. biological structures that are also relevant to this work. Specifically, the effect of Fe(III), Zn(II) and Cu(II) ions on

the secondary structure of amyloid beta (Aβ) peptides was investigated as these ions are suspected to play a role in amyloid aggregation observed in Alzheimer's disease[87]. FTIR was also applied to investigate coordination complexes between Fe(II) cations and microcrystalline cellulose or long cellulose fibres, revealing that coordination bonds form between Fe(II) and deprotonated or oxidized hydroxyl groups[88].

Among other spectroscopic techniques used for biofilm studies, Raman spectroscopy needs to be mentioned as a complementary vibrational spectroscopy technique. Also, UV-visible and fluorescence spectrophotometry are used as well as small angle x-ray scattering and nuclear magnetic resonance (NMR)[89]. Finally, genetic, mutagenesis and signalling pathway studies have greatly contributed to the understanding of biofilms[45,90–92]; however, these methods are outside the scope of this work and will not be discussed further.

2.4. Tuning biofilm properties

2.4.1. Environmental factors

While the influence of environmental factors on biofilm and EPS production has been investigated for a long time, mechanical properties have moved into focus only recently. One of the main environmental conditions directly influencing the morphology and mechanics of biofilms is the availability of water. When biofilms are grown on an agar plate, the agar concentration in the gel is inversely proportional to its water content. In general, biofilms grown on substrates with higher agar concentration tend to be smaller and stiffer than their counterparts grown on substrates with lower agar content. This was observed and explained for most model biofilm-producing bacteria. For example, it was shown that the substrate water content influences the morphology and the stiffness of *E. coli* biofilms. Substrates with low water content promote biofilm wrinkling and delamination, and lead to stiffer biofilms covering a smaller area, while substrates with high water content promote biofilm spreading kinetics[18]. In *V. cholerae*, the growth and surface coverage of biofilms is

driven by the osmotic pressure difference between the biofilm and the external environment, which was observed both for biofilms at air-solid interface and submerged biofilms[59]. In addition, the friction between the agar substrate and the biofilm plays a role. In a modelling study, Fei et al. assumed that the friction coefficient is proportional to the stiffness of the substrate, which increases with the agar concentration. Their model showed that stiffness and friction determine the wrinkling pattern of *V. cholerae* biofilms. Wrinkles initially appear in the central region and propagate outward on a soft and low-friction substrate, while they appear at the edge and propagate inward on a stiff and high-friction substrate[93]. However, the role of water in forming an osmotic gradient also needs to be taken into account, as shown by Yan et al.[94]. In addition, the water layer forming on the substrate also reduces the interfacial friction between the biofilm and the substrate, an hypothesis taken into account by Stecchini et al.[95]. In their experiments with *Bacillus cereus* biofilms, radial growth diminished with increasing agar content[95]. Interestingly, lower colony density values as well as thinner colonies were observed for lower agar concentration[95]. In *B. subtilis*, too, doubling the substrate agar concentration results in lower expansion velocity and smaller biofilms. A similar mechanism based on the increase of friction between the biofilm and the agar was proposed[96]. The substrate water content is thus a convenient way to tune both the spreading and the stiffness of the biofilm by acting on the friction between the film and its substrate. Finally, the possibility of controlling the water content is not limited to hydrogel substrates. When subjected to desiccation while grown on a sandy substrate, *Pseudomonas sp.* produce more EPS than when growing at high water potential. Moreover, sand amended with EPS retains significantly more water and dries more slowly, suggesting EPS production as a defence mechanism against desiccation[97]. Similarly, relative humidity can also be used to act on biofilm growth. The evaporative flux from the biofilm surface is the driving force for the flow of liquid in biofilm channels, which in turn transports nutrients. Therefore a lower relative humidity leads to more evaporation and thus increases growth[98].

In addition to substrate osmolarity, the substrate nutrient content also plays a role. For *P. aeruginosa* biofilms, high-nutrient environments lead to an increased EPS production compared to

biofilms grown in low-nutrient environments. Biofilms grown in more nutritive environments are also twice as stiff when compared to those grown in less nutritive environments[99]. It was observed for *B. subtilis* that increasing the nutrient concentration boosts the biofilm expansion rate, delays the time at which the expansion velocity reaches a maximum and delays the appearance of wrinkles. A 5-fold increase of the nutrient standard concentration led to higher expansion velocity than a 3-fold increase, i.e. no optimum in concentration was measured[96].

In natural conditions, biofilms rarely grow on nutritive hydrogel substrates. When colonizing drinking water or sewage pipes, or even the inside of medical catheters, biofilms regularly encounter shear forces induced by fluid flow. They have therefore developed mechanisms to cope with them, which can in turn be used to alter the morphology or the mechanics of the biofilms. The adaptation of biofilms to different flow conditions has long been investigated. Multi-species cultures of *K. pneumoniae*, *P. aeruginosa*, *P. fluorescens* and *Stenotrophomonas maltophilia* produce disk-like biofilms in laminar flow, while they produce biofilms elongated in the direction of the flow in turbulent conditions. In addition, biofilms grown in turbulent flow produce ripples that migrate downstream over time[100]. Similar experiments were performed for the sulphate-reducing *Desulfovibrio sp* and a similar influence of flow-velocities on biofilm shape was demonstrated. At high flow velocity (Reynolds number (Re) = 1200), *streamers* (biofilms elongated in the direction of the flow) were observed, while at low flow-velocity (Re = 120), clusters of biofilms were observed. Moreover, biofilms grown at higher Re were stiffer with a higher yield point (the yield stress beyond which the biofilm starts to flow)[101]. In certain strains of *S. epidermis*, it was shown that fluid shear alone induces the production of a biofilm matrix containing a polysaccharide intercellular adhesin, a poly-acetyl-glucosamine[102]. As described for solid substrates, nutrient availability (e.g. glucose) can also be used in liquid to tune biofilm growth, as was shown for *P. aeruginosa* grown in a microfluidic chip[103]. Antibiotics (ciprofloxacin) can also be used in a similar way[103].

Temperature is another factor, the influence of which has been investigated across many bacteria species. However, unlike substrate water content or shear, the influence of temperature on biofilm

formation varies significantly from one species to another. For *Vibrio parahaemolyticus*, biofilm formation is significantly higher at 25°C than at 15°C or 37°C. Moreover, the growth profile differs with temperature. At 15°C, biofilm formation increases continuously, while at 25°C, biofilm formation increases gradually and peaks after 12 hours[104]. Temperature also plays a role in biofilm growth dynamics in *Salmonella spp.*. After 24 hours of growth, the optical density (OD) of biofilms grown in a multi-well plastic microplate was higher at 30°C than at 37°C or 22°C. After 48 hours however, the OD was higher at 22°C[105]. In the foodborne pathogen *Listeria monocytogenes*, biofilm formation was tested at four temperatures: 12°C, 20°C, 30°C and 37°C. Overall, biofilm formation decreased with decreasing temperature[106]. A study performed on 67 *S. aureus* strains isolated from food, food processing environments and handlers also demonstrated the effect of temperature on biofilm formation in the pathogenic bacterium. While most strains formed biofilms at 37°C on various surfaces, only one strain was able to form biofilms at 12°C[107]. Finally, *E. coli* biofilms were stiffer when grown at 30°C than when grown at 37°C due to an increase in curli production at 30°C[66]. Liquid medium pH has an influence as varied as temperature. For *P. fluorescens* biofilms, exopolysaccharide production is optimal at pH 7[108]. However, biofilm formation in Group B *Streptococcus* is significantly higher at pH 4.5 than at pH 7[109]. Similarly, in Group A *Streptococcus* (*S. pyogenes*), low pH enhances biofilm formation as well as the expression of the genes encoding pilus proteins[110].

2.4.2. Genetic engineering

In addition to environmental factors, interesting material properties can also be obtained when using synthetic biology to reprogram the bacteria genetics. The possibilities are so vast that genetic engineering deserves its own section. Genetic engineering has, for example, been applied to better control the genes involved in polysaccharide synthesis, e.g. with the goal of increasing their production. A modular genetic toolkit was developed specifically for a strain of *Komagataeibacter rhaeticus*, a high-yield producer of cellulose isolated from Kombucha tea, thereby enabling external

control over its cellulose production[111]. In *Bacillus amyloliquefaciens*, the production of a high-purity and low-molecular weight levan was maximized by knocking out the genes responsible for other main matrix components (TasA fibers and poly-γ-glutamic acid) as well as extracellular proteases[112].

Genetic engineering of the matrix peptidic compounds has been much more broadly investigated than in the case of polysaccharides because proteins are easier to functionalise than sugar polymers. For this reason, the examples mentioned below will be restricted to research conducted in *E. coli* only, i.e. on the amyloid curli fibres made of CsgA subunits. Before even altering the nature of the amyloid fibres, genetic engineering can be used to control the environmental factor triggering their production. With the aim of fighting water pollution by mercury, *E. coli csgA* transcription was placed under the mercury-responsive P_{merR} promoter, itself constitutively repressed by the MerR repressor. In presence of mercury, MerR changes conformation and the promoter is de-repressed. Curli fibres were excreted and sequestrated Hg(II) cations in solution[113]. *E. coli* was also engineered to obtain light-controlled CsgA production. Different colours of light led to the expression of CsgA fused to different peptide tags. When projecting colour images, cells could be patterned on various materials such as polystyrene, cotton and 3D-printed materials[114]. Similarly, *E. coli* was adapted to express an adhesin gene (Ag43) under the control of a light-activated transcriptional promoter (pDawn). This enables biofilm patterning upon blue light exposure, with a spatial resolution of 25 µm and without requiring surface pre-treatment[115].

Even more widespread is the fusion of CsgA with functional domains. The goal of such a strategy can be to immobilise an enzyme onto the extracellular matrix in order to improve its activity, or to provide the biofilm with completely new functions. At this stage, the only limit seems to be the imagination of researchers, with potential applications in fields as varied as metal bioextraction, disinfection or biomaterials. For example, in order to improve the catalytic synthesis of trehalose from starch, the immobilisation of β-amylase on CsgA was coupled with the intracellular expression of trehalose synthase in the same *E. coli* cell. This configuration increased the maximum trehalose formation rate as well as the conversion of starch into trehalose[116]. In the same way, CsgA was

appended with a lipase-binding protein to immobilise the Lip181 lipase onto curli fibres. In doing so, Lip181 thermo-, pH and storage stability as well as its relative activity were increased, thereby leading to increased catalytic performances[117].

Curli amyloid fibres were also genetically modified to display lanthanide binding tags (LBTs) to produce rare earth filters. The biofilm-based filters showed lanthanide specificity in presence of other metals and bound several high-value rare earth elements. Metals could be recovered by washing with dilute nitric acid and the filters reused for several cycles[118]. With a health sector targeting approach, CsgA was fused with the influenza-virus-binding peptide (C5). Using the resulting biofilms as a sequestrator, aqueous solutions could be disinfected below the limit of detection of qPCR-based detection assays[119]. The functionalization of CsgA is not limited to enzymes and binding motifs. Other applications of biofilms that can be realized with genetic engineering include conductive biofilm-based materials. To do so, conductive peptides, containing different combinations of tyrosine and tryptophan, were inserted into CsgA[120].

When combining several of these approaches, entirely new materials can be synthetized. CsgA fibres genetically fused to human trefoil factors (TFF) 1, 2 and 3 were produced, secreted and assembled by *E. coli*. Moreover, curli matrices formed from such fibres maintained the ability of TFF to bind mucins, as well as their signalling bioactivity, and also showed enhanced bacterial adhesion to mammalian cell surfaces[121]. CsgA functionalized with TFF2 also formed hydrogels that can be cast and dried at ambient temperature, resulting in aquaplastics that resist strong acids and bases as well as organic solvents[8]. The *E. coli* MG1655 strain was genetically modified to create a glue based on CsgA that can be chemically or light-controlled. The amyloid glue was capable of capturing non-sticky microspheres from a solution to form living composite coatings. Moreover, by coupling the production of the modified CsgA to a heme-sensitive gene circuit, damages in a microfluidic device could be autonomously repaired upon blood sensing[122]. Finally, biofilm 3D-printing has been widely investigated and bioinks based on *E. coli* were developed. Indeed, engineered CsgA nanofibres assemble into a network forming extrudable hydrogels. Functional living materials could thus be 3D-

printed from the bioink containing *E. coli* cells embedded in their excreted nanofibres[123]. Recently, the biological endurance to disinfectants was investigated for 3D-printed *E. coli* biofilms with various matrix compositions (curli +/- cellulose, or neither fibre). The highest biological endurance to ethanol or Virkon™S was measured for a matrix containing both fibres[124].

2.4.3. Metal ions

Metal ions are widespread in nature and play a multitude of roles in living organisms. They are required for catalytic activity in enzyme active sites and control transcription factor structure and activity. The following section will focus on cases where metal ions directly affect the mechanical properties of biological materials, for example, where they contribute to increasing stiffness, hardness, adhesion or even self-healing properties.

In arthropods, higher concentrations of metal ions are detected in organs that require additional stiffness or hardness such as stings or fangs. High concentrations of Zn(II) ions are measured in the mandibular teeth of the ant *Tapinoma sessile* as well as in the pedipalp and cheliceral teeth, tarsal claws and sting of the scorpion *Vaejovis spinigeris*[125]. The spider *Cupiennius salei* incorporates Zn(II) and Ca(II) cations in the cuticle of its chitin-made fangs. The stiffness and hardness are highest at the tip of the fang and decrease away from it. Interestingly, this correlates with the highest concentration of Zn(II) at the tip of the fang. Ca(II) is also localised in the fang with a complementary distribution to Zn(II)[126]. The contribution of metal ion complexation to material properties is not limited to arthropods. Zn(II) is also essential for the mechanical properties of the polychaete *Nereis* jaws, where both stiffness and hardness were shown to decrease by more than 65% in case of Zn(II) chelation[127]. The presence of chlorinated and brominated residues was also detected and the main determinants of local jaw hardness were shown to be Zn(II) and chlorinated functional groups[128]. In molluscs, the granular cuticle of the byssus of the mussel *Mytilus galloprovincialis* was demonstrated to be a polymeric scaffold stabilised by complexes between 3,4-dihydroxyphenylalanine (DOPA) and Fe(III)[129]. Such complexes are responsible for cuticle hardness, which decreased by 50% after

chelation by ethylenediaminetetraacetic acid (EDTA)[130]. In addition to stiffness and hardness, metal chelation can also facilitate adhesion. Cross-linking by metal ions, in particular Ca(II), is also suspected to play a role in the glue produced by the slug *Arion subfuscus*[131]. Similarly, the polychaete worm *Phragmatopoma californica* secretes a proteinaceous cement to form protective tubes by joining bits of sand grains and shells. The adhesive contains several proteins, some with DOPA residues and others with a high number of phosphorylated serine. Proteins are excreted in the form of granules, which also contain Mg(II) cations[132,133]. Metal-protein interactions are up to half the strength of covalent bonds. However, the ability of metal-coordination bonds to rapidly dissociate and associate enables them to serve as sacrificial bonds, which in turn provides biological materials with self-healing capacity[20,26]. In this context, a much-studied living organism is the mussel *Mytilus californianus*, where reversible sacrificial protein-Zn(II) coordination bonds, primarily involving histidine residues, were shown to be responsible for the self-healing properties of its byssus[134].

Amyloid-forming fibres are peptidic compounds known for interacting with metal ions. These include for example Aβ peptides, which are the main components of amyloid plaques responsible for Alzheimer's disease. *In vitro*, Zn(II) was shown to inhibit the formation of β-sheets while Fe(III) and Al(III) trigger amyloid formation or stabilise the structures. In amyloid plaques, the three metal cations co-localise with Aβ[135]. 3D-models have shown that Al(III) is almost always hexacoordinated and interacts with aspartate and glutamate residues in Aβ-complexes[136]. Zn(II) coordinates four to six ligands in Aβ-complexes, including three histidine residues as well as one aspartate and/or glutamate residue[137]. Despite a lack of structural studies on Fe(III) coordination to Aβ[138], ferric ions are known to bind histidine more efficiently than Zn(II)[139]. To date, curli amyloid fibres have only been demonstrated to sequester Hg(II) ions, suggesting a possible general ability to bind metal cations[140].

Cellulose is the most abundant biopolymer on Earth. It is well-known for sequestrating metal ions. This property has mostly been studied with the aim of heavy metal removal. Untreated sugarcane bagasse, a by-product of the sugarcane industry that contains 50% cellulose, has been shown to

adsorb Cd(II), Pb(II), Cr(IV) and As(V) among other heavy metals[141]. Cellulose is rarely used alone for remediation as it is not very efficient. Various chemically-modified celluloses have been developed, thereby improving the adsorption efficiency[142]. Interestingly in the context of this thesis, phosphorylation of cellulose nanofibres significantly enhances their adsorption capacity of Fe(III) ions[143]. However, no data is yet available concerning the interaction of Al(III) or Fe(III) with pEtN-cellulose, the form present in *E. coli* biofilms.

Biofilms frequently grow in an environment rich in metal ions such as wastewater basins or at the inner surface of metallic pipes. The effect of metal ions on their mechanical properties has thus been investigated, at first with the aim of better fighting them and, subsequently, as a way to tune their properties. For *Enterobacter asburiae*, *Vitreoscilla sp.* and *A. lwoffii*, metal ions promote biofilm formation[27]. In the case of *S. epidermidis*, *B. subtilis* and *P. aeruginosa*, biofilms stiffen in the presence of metal cations[28]. Specifically, *B. subtilis* biofilms stiffen and erode slower in presence of Fe(III) and Cu(II)[29]. In *B. subtilis* B-1 and *A. vinelandii*, both the ion size and the configuration of the polyanionic macromolecules in the matrix determine whether biofilm stiffening occurs[57]. In *P. aeruginosa*, however, the key factor seems to be the cation valence as only Fe(III) and Al(III) were shown to trigger stiffening[56]. The mechanism behind cation-mediated biofilm stiffening, therefore, seems to be specific to the bacterium species. While metal cations can stiffen biofilms by cross-linking the matrix, a wide range of metal complexes has also demonstrated anti-biofilm activity[144].

Making use of genetic engineering, some metal ion-binding motifs found in multicellular organisms have been introduced into biofilm-forming bacteria with the aim of further tuning their mechanical properties. For example, the amyloidogenic protein TasA from *B. subtilis* was appended with the mussel foot protein Mepf5 and the hydrophobin BslA was equipped with the mussel-derived peptide Mfp3Sp. Both Mepf5 and Mfp3Sp are rich in tyrosine residues. When expressing a tyrosinase to convert tyrosine into DOPA, curing of the biofilm material with Fe(III) cations became possible. This strategy increased the shear adhesive strength and the resistance to detergents, among other

properties, resulting in "*functional cellular glue*"[7]. Noteworthy, a similar approach was also applied to *E. coli* but no metal-curing step was reported[122].

Interestingly, the effect of metal ions on *E. coli* biofilm mechanics has not yet been investigated at the same level of detail as for other biofilm-forming model bacteria. An inhibitory effect of trivalent metal cations on bacterial growth was reported. For example, 10^{-5} M of $LaCl_3$ reduces the number of colony-forming units (CFU) by 98% while $FeCl_3$ and $AlCl_3$ reduce it by 40% and 50%, respectively[145]. In addition, $FeCl_3$ also triggers the production of rugose biofilms in *E. coli*. In such biofilms, two populations of bacteria can be distinguished: an external population at the air-biofilm interface producing matrix and expressing *csgD* at high-levels; and an internal population with low levels of *csgD* expression and no detection of cellulose or curli. The activation of rugose biofilms by Fe(III) is linked to oxidative stress. Mitigating iron-derived reactive oxygen stress reduces biofilm formation upon exposure to $FeCl_3$, while superoxide generation stimulates rugose biofilm formation even in absence of $FeCl_3$[30]. In addition, an Fe(II)- and Zn(II)-sensing transcription regulator (BasS-BasR) has been shown to upregulate *csgD* transcription[146].

Metal ions play a key role in controlling the tissue mechanics of many organisms. They are particularly influential in biofilms, the mechanical properties of which can be tuned post-growth by incubation with metal ions[57]. The bacterium *E. coli* is one of the most studied organisms, as it is crucial to both our health and our economy. However, while *E. coli* also serves as a model organism for the study of biofilms, very little is known concerning the influence of metal cations on biofilm mechanics, in particular after growth. Since the mechanisms involved, the determining criteria and the resulting biofilm properties seem to vary from one bacterium species to another, their thorough investigation for *E. coli* is essential. What are the effects of metal cations on the mechanical properties of *E. coli* biofilms? If such effects exist, what are the factors determining which particular cation plays which role? Knowing the composition of *E. coli* biofilms and assuming a contribution of biofilm architecture, which matrix component(s) interact(s) with metal cations? What interactions take place at the molecular level?

3. Scope of this thesis

In this doctoral thesis, I aimed to explore key open questions about the contribution of matrix composition and architecture to the properties of *E. coli* biofilms, with a particular focus on tuning the viscoelasticity of *E. coli* biofilms with metal cations and their possible interaction with fibres.

My first goal was to investigate if and how the viscoelastic properties of *E. coli* biofilms can be tuned by the addition of metal cations and to explore the role of curli amyloid and pEtN-cellulose fibres. Biofilms with different matrix composition were mixed with salt solutions of $FeCl_3$, $AlCl_3$, $ZnCl_2$ and $CaCl_2$ and their viscoelastic properties were determined with shear rheology. As controls, ultrapure water was used along with controls for the pH and osmolality of the respective solutions. To account for the low pH of the above salt solutions, an HCl control solution with a pH similar to the $FeCl_3$ solution was used. In addition, an NaCl control solution was used that matched the osmolality of the $FeCl_3$ solution. In practise, biofilms were grown on nutritive agar substrates for one week, scraped from the agar surface and mixed with one salt solution or ultrapure water. Shear strain amplitude sweeps were then performed with an oscillatory rheometer. The elastic and viscous biofilm properties were obtained from the plateau values of the storage and the loss moduli, respectively. Subsequently, the moduli measured in the presence of different salt solutions were compared to the control with ultrapure water to identify whether a biofilm with a particular matrix composition stiffened or softened in the presence of a particular metal cation.

Even though the same sample preparation strategy has been used in the past for rheology experiments of other biofilms, it appears likely that the architecture of *E. coli* biofilms is destroyed at least partially. In the second study, I compared stiffness measurements from rheology with stiffness measurements obtained from less destructive microindentation to assess how biofilm homogenization upon mixing with salt solutions affects the viscoelastic properties. When performing microindentation, the biofilms can be measured directly on their agar substrate and the matrix architecture can be preserved. The Young's moduli obtained from indentation curves were compared to the shear moduli obtained from rheology. At this stage, a larger variety of different

matrix compositions was tested to gain further insight into the contributions of these components. In addition to the matrices mentioned in the previous paragraph, strains producing non-modified cellulose were tested with or without the expression of curli as well as a strain that did not produce any of these two matrix components.

Both rheology and microindentation provide information about the bulk mechanical properties of biofilms but do not provide any information about matrix-cation interactions at the molecular level. In the third and last project, I thus used Fourier-transform infrared spectroscopy (FTIR) to obtain molecular signatures and to identify which matrix components interact with metal cations. In addition, matrix fibres were purified from the biofilms of *E. coli* strains that produce only curli or pEtN-cellulose. The purified fibres were mixed with the respective salt solutions and also characterized with FTIR. The resulting spectra were used to detect possible changes in curli secondary structure as well as functional groups interacting with metal cations.

4. Materials and Methods

4.1. Culture and solutions

4.1.1. Bacterial strains

Different *E. coli* strains were used to distinguish between the contributions of the two main matrix fibres to the mechanical biofilm properties, and the dependence of these properties on the presence of metal cations. W3110 is a non-pathogenic K-12 strain[44] that produces curli amyloid fibres and lacks the ability to synthesize cellulose. Cellulose synthesis, which is encoded in the *bcs* operon, was restored in the strain AR3110[46]. This W3110-based strain thus produces both curli amyloid fibres and pEtN-cellulose. To obtain a strain that produces only pEtN-cellulose, curli production was inactivated in the strain AP329 (AR3110 *ΔcsgBA*)[16]. AP470 (AR3110 *ΔbcsG*) is a strain derived from AR3110 that produces amyloid curli proteins and non-modified cellulose, i.e. without the pEtN-modification[46]. AP472 (AR3110 *ΔcsgBA ΔbcsG*) is a AR3110 derivative strain that produces only non-modified cellulose[46]. AR198 (AR3110 *ΔcsgB ΔbcsA)* is a strain derived from AR3110 that produces neither curli amyloid proteins nor cellulose[46]. This library of bacterial strains was kindly provided by Prof. Dr. Regine Hengge's research group from the Humboldt University of Berlin, Germany. To test biofilm properties when both curli and pEtN-cellulose are present, but not produced by the same bacterial cell, W3110 and AP329 were combined before inoculation (co-seeded) or when harvesting the mature biofilms for the rheology experiments (mixed).

4.1.2. Biofilm growth

For bacterial culture, LB agar plates (Luria/Miller; x969.1, Carl Roth GmbH) were prepared. A bacterial suspension, grown from glycerol stocks, was streaked onto these agar plates to obtain microcolonies after overnight culture at 37°C. One day before starting biofilm growth, two single microcolonies were separately transferred into LB medium (5 mL; Luria/Miller; x968.2, Carl Roth GmbH) and incubated overnight at 250 rpm and 37°C. The OD_{600} of the resulting bacteria suspensions was measured after a 10-fold dilution. The sample where OD_{600} of the diluted suspension was closest to 0.5 was chosen for inoculating the biofilms. Biofilms were grown on salt-

free LB agar plates as media with low osmolarity promote matrix production[147]. The salt-free LB agar plates were composed of tryptone/peptone ex casein (10 g L^{-1}; 8952.1, Carl Roth GmbH), yeast extract (5 g L^{-1}; 2363.1, Carl Roth GmbH) and bacteriological agar agar (18 g L^{-1}; 2266.3, Carl Roth GmbH). On each Petri dish (ø = 145 mm), 9 x 5 µL of suspension were inoculated to obtain an array of 9 biofilms. For the "co-seeded" biofilm samples, OD_{600} of the two suspensions was measured and the suspensions were combined such that the final density of each bacterial strain was identical. Inoculation took place immediately after a short mixing step. For the "mixed" samples, both bacterial strains were grown on the same agar surface. All biofilms were grown at 28°C for 7 days, unless specified otherwise, and then stored in the fridge at 5°C for a maximum of 48 h. Images of the biofilms were acquired with an AxioZoomV.16 stereomicroscope (Zeiss, Germany).

4.1.3. Metal salt solutions

The following salts were used to probe the influence of trivalent and bivalent cations on biofilm properties: aluminium chloride hexahydrate (97%; 26726139, Molekuka GmbH), iron(III) chloride anhydrous (I/1035/50, Fisher Scientific), zinc chloride (≥98%) (29156.231, VWR International) and calcium chloride dihydrate (≥99%; C3306, Sigma-Aldrich). $AlCl_3$, $FeCl_3$, $ZnCl_2$ and $CaCl_2$ were dissolved in ultrapure water to a concentration of 220 mM and the pH was measured with a pH-meter (WTW GmbH; Table 2). Using the $FeCl_3$ solution as a reference, a control solution with identical pH was prepared using hydrochloric acid (1.09057, Merck KGaA). In addition to the pH, the osmolality of the metal salt solutions can also influence biofilm properties *via* water intake of the biofilm. The osmolalities of the different solutions were measured with an osmometer (Osmomat 3000, Gonotec GmbH). The osmolalities were determined from a calibration curve established from solutions of sodium chloride (39781.02, Serva Eletrophoresis) (Table 2, Annex Figure 22). Similar to the pH control, a NaCl solution was prepared that matched the osmolality of the $FeCl_3$ solution.

Table 2. Concentration, pH and osmolality of the four metal salt solutions $FeCl_3$, $AlCl_3$, $ZnCl_2$, $CaCl_2$ and the NaCl and HCl control solutions.

Solution	$AlCl_3$	$FeCl_3$	$ZnCl_2$	$CaCl_2$	NaCl	HCl
Concentration (mM)	220	220	220	220	409	32
pH	2.8	1.5	5.7	5.2	-	1.5
Osmolality (mOsmol/kg)	895	754	598	618	754	-

4.2. Influence of metal cations on the viscoelastic properties of *Escherichia coli* biofilms

4.2.1. Sample preparation for rheology experiments

Depending on the *E. coli* strain, two or three biofilms (~90 mg) were scraped from the agar surface and transferred into an empty Petri dish using cell scrapers. For the "mixed" biofilm samples, materials from both strains were combined in equal proportions. All samples were gently stirred with a pipette tip and either measured as obtained (neat) or incubated with the desired metal or control solution (diluted). For the experiments that required the incubation of the biofilm with the respective solution, the scraped biofilms were stirred with the solution in a ratio of 10:1 (w/v), yielding a final cation concentration of ~20 mM. After stirring, the Petri dish was sealed with Parafilm and left to incubate at room temperature for 45 min. For every dilution experiment, two samples from the same agar plate were measured. One was incubated with the solution of interest and the other sample was incubated with ultrapure water. To document sample texture, images of the different mixtures were taken with a 2-megapixel USB camera (Toolcraft Microscope Camera Digimicro 2.0 Scale, Conrad Electronic SE).

4.2.2. Bacterial growth experiment after incubation with metal salt solutions

In addition to rheology experiments, bacterial growth was monitored after biofilm incubation with metal salt solutions in order to assess the potential toxicity of the solutions on bacteria within the biofilms. To do so, biofilms were grown, scraped and mixed with metal salt solutions in a Petri dish as previously described. Unlike the sample preparation for rheology, those steps were performed in sterile conditions. Two solutions were tested: $FeCl_3$ and $ZnCl_2$; as well as ultrapure water. After 45 min of incubation, a portion of the resulting mixture was transferred for inoculation into 5 mL of LB medium using an inoculation loop. The resulting liquid cultures were briefly vortexed and incubated at 250 rpm and 37°C. The inoculated biofilm mass was determined by subtracting the mass of the dish containing the mixture before and after inoculation. Bacterial growth was monitored with OD_{600} measurements after a 10-fold dilution after 180, 270, 360 min and overnight growth (~23 hours). The bacterial concentration was determined using the following relation: OD_{600}=1 corresponds to $10*10^{-8}$ cells/mL[148], with the additional factor 10 corresponding to the 10-fold dilution. The concentration was subsequently divided by the initial biofilm mass inoculated, supposedly proportional to the initial number of bacteria inoculated.

4.2.3. Biofilm buffering capacity

Since the four metal salt solutions tend to have a low pH, the buffering capacity of the biofilms was assessed. Phosphate buffers (0.1 M) were prepared with pH = 2, 7 and 12, using phosphoric acid and its potassium salts. Biofilms of the three strains used in the rheology experiments (AR3110, W3110 and AP329) were grown for one week, scraped from the agar surface and transferred into Petri dishes, as previously described. After weighing (PG1003-S analytical balance, Mettler-Toledo LLC), biofilms were stirred with ultrapure water or buffer in a ratio of 10:1 (w/v). The pH of the resulting mixture was measured immediately after mixing using pH-paper (PH-FIX Indikatorstäbchen pH 0-14, Macherey-Nagel GmbH & Co. KG) and again after 45 min of incubation in the Petri dish sealed with Parafilm.

4.2.4. Assessing evaporation during the incubation with metal ions

To assess whether evaporation depends on the type of solution added, biofilm mass was determined at the start and end of the incubation period. Reproducing the sample preparation method for rheology, biofilms were weighed (ABJ 220-4NM precision balance, Kern & Sohn GmbH) and subsequently stirred with ultrapure water or the respective NaCl, $ZnCl_2$ or $FeCl_3$ solutions in a ratio of 10:1 (w/v). They were weighed again after stirring and left to incubate in a Petri dish sealed with Parafilm for 45 min and then weighed one last time. The weighing steps took place with the Petri dish open and the water loss was calculated from the difference in mass before and after incubation.

4.2.5. Rheology measurements

The measurements were performed with an oscillatory shear rheometer (MCR301, Anton Paar GmbH) under stress control. The sample stage was equipped with Peltier thermoelectric cooling and the temperature was set to 21°C for all measurements. Once the sample was transferred onto the stage, a channel around the stage was filled with water and a hood was used to maintain a high humidity environment. A parallel plate geometry (ø = 12 mm) was used and the gap was set to 250 µm.

To quantify the viscoelastic properties of the biofilm, strain amplitude sweeps were carried out to determine the linear viscoelastic (LVE) range and to extract the storage (G'_0) and loss (G''_0) moduli. The oscillation frequency was set to 10 rad s^{-1}. The strain amplitude was increased from 0.01% to 100% with 7 points per decade and then decreased again. These cycles of ascending and descending strain amplitude were repeated 3x. One experiment with 3 cycles lasted approximately 45 min. The data presented in the Results sections (5.1 and 6.1.2) were extracted from the ascending amplitude sweep in the second cycle. The first cycle was considered as an additional homogenisation step.

To validate the chosen oscillation frequency, frequency sweeps were performed for AR3110 samples. The strain amplitude was set constant to 0.02%. The oscillation frequency was decreased step-wise from 100 rad s^{-1} to 1 rad s^{-1} with 7 points per decade. Alternatively, frequency sweeps were performed with a frequency increasing from 1 to 100 rad s^{-1}. This ranges from one order of

magnitude above and below the frequency used for the amplitude sweeps. Frequency sweeps were also performed over a wider range of frequencies, i.e. from 100 to 0.001 rad s^{-1}; however, these measurements showed excessive drying of the biofilm samples at low frequencies. All frequency sweeps were carried out with neat biofilms and samples mixed with 10% (v/w) ultrapure water, and both preceded or not by a pair of increasing and decreasing amplitude sweeps as previously described.

To validate that sample drying does not affect the data acquired within the second ascending amplitude sweep, sample properties of AR3110 were recorded for a duration of at least 3 h, using a low oscillation frequency of 10 rad s^{-1} and strain amplitude of 0.02%. This test was also preceded by a pair of amplitude sweeps (increasing and decreasing strain amplitude) as previously described.

4.2.6. Data analysis for the rheology measurements

To determine biofilm properties, the G' and G'' values were averaged over a strain range from 0.01 to 0.02% (3 data points). These values represent the plateau moduli G'_0 and G''_0 of the respective biofilms (neat samples vs. samples diluted with ultrapure water). For the dilution experiments with solutions of metal cations, the primary focus was on the relative difference between moduli. That is, the modulus of the sample diluted with the solution of interest was corrected by the modulus of a sample (from the same Petri dish) diluted with ultrapure water. This comparison to a reference sample, grown under identical conditions, was necessary to account for biofilm sample variability between Petri dishes.

For both moduli, the relative difference was calculated as follows, as exemplary shown for G'_0:

$$\Delta G'_0 = \frac{G'_{0,solution} - G'_{0,water}}{G'_{0,water}}$$

For each condition tested, the median was determined ($n_{pairs} \geq 4$) as the data was not normally distributed. The data is shown in the form of boxplots and the whiskers of the boxplots represent 1.5

times the interquartile range (IQR). To assess whether the relative differences of the moduli show a significant difference from zero, i.e. the effect of the solution tested differs from that of water, a one-sample Wilcoxon signed rank test (μ = 0, a = 0.05) was performed, using the program R (R Core Team; version 4.0.5).

4.3. Microindentation to assess the contribution of the biofilm macroscopic architecture to its viscoelastic properties*

The microindentation experiments were performed on native biofilms. Biofilms were seeded on salt-free LB agar as previously described and then grown for 4 days at 28°C. The measurements took place either directly after growth or after storage in the fridge at 5°C for up to 5 days. During storage, the Petri dishes were sealed with parafilm to prevent evaporation. 2 to 4 biofilms were tested per condition. The measurements were performed while the biofilms were still attached to their agar substrate, i.e. in their native conditions, unless specified otherwise. Microindentation measurements were performed using a TI 950 Triboindenter (HYsitron Inc., USA) and data was acquired in the form of load-displacement curves $p - \delta$. The calibration was done in air. The samples were indented using a spherical diamond tip (r = 50 μm) on an extended displacement stage (xZ-500 displacement stage, Bruker), adapted to the measurement of soft biological samples. The samples were approached vertically from 300 to 400 μm above the biofilm surface, indented and the indenter was retracted to the starting position. The applied force was recorded over the whole range. Loading/unloading rates ranged from 20 to 30 μm s^{-1}, corresponding to loading/unloading times of 10 s. In the case of native samples, the central region of each biofilm was indented 8 times. Two measurement points were separated by a minimum of 250 μm both in x and y directions.

The reduced Young's modulus was obtained by fitting the loading part of the curve (displacement range: δ = 0-10 μm) with a Hertzian contact model[149]:

* All microindentation experiments were performed by Ricardo Ziege either in parallel or at a different moment. Those results are thus not formally part of the present thesis but were part of a common project. They are introduced in this work for the sake of comparison with the rheology data.

$$p = \frac{4}{3} E_r \, R^{\frac{1}{2}} \, \delta^{\frac{3}{2}}$$

The work of adhesion was calculated by integrating the area under the unloading curves, for p < 0. Load-displacement curves were analysed only when the maximum load was reached within the displacement range from 7 to 30 µm, to ensure comparable tip-sample contact areas. This was necessary as the absolute depth of indentation cannot be controlled when the microindenter is running in the "*air-indent*" mode. For each condition tested, median values and standard errors were calculated only over the analysed load-curves. The median was used instead of the mean because the data was not always normally distributed. The standard error of the median was estimated using a bootstrap (see Annex) strategy (number of iterations: 1000) implemented in the program R (R Core Team; version 4.0.5).

4.4. Molecular interactions between metal cations and the biofilm matrix

4.4.1. ATR-FTIR measurements on biofilms

ATR-FTIR was used to investigate the molecular mechanisms responsible for the bulk effects observed with rheology. For this purpose, three bacterial strains (AR3110, W3110 and AP329) and six solutions ($FeCl_3$, $AlCl_3$, $ZnCl_2$, $CaCl_2$, NaCl, HCl), as well as ultrapure water, were tested. The concentrations of the solutions were the same as already specified for the rheology experiments. For each combination of one solution and one bacterial strain, three replicates were measured. All combinations and replicates involving the same bacterial strain were measured on the same day. Biofilms were scraped from the agar, weighed and mixed with the solution or ultrapure water in a 10% (w/v) ratio. The mixtures were then transferred onto the diamond crystal surface of the spectrophotometer (Vertex 70v, Bruker Optik GmbH) and partially dried under N_2 flow for 3 min. The spectrometer is equipped with a single reflection diamond reflectance accessory, which is continuously purged with nitrogen to minimise water vapour distortions in the spectra[150]. Every measurement consisted of 64 accumulations recorded at 25°C, between 7500 and 600 cm^{-1} with a spectral resolution of 0.4 cm^{-1}. Baseline correction (method: Rubberband correction) and

atmospheric compensation were performed with OPUS software (Bruker Optik GmbH; version 7.0). The data was normalised to a 0-1 range and plotted in R (R Core Team; version 4.0.5).

Normalisation: $z_i = \frac{x_i - \min(x)}{\max(x) - \min(x)}$ with x_i and z_i the intensity data respectively before and after normalisation.

For biofilm spectra, the maximum corresponded to the peak at 1623 cm^{-1}, or exceptionally the peak at 3280 cm^{-1}. Normalising the biofilm spectra with respect to the maximum over the range was chosen because not all biofilm replicates showed the same maximum. In doing so, all replicates could be simultaneously plotted without overlapping (Annex 12.3.1).

4.4.2. Curli amyloid and pEtN-cellulose purification*

The protocol for the purification of curli fibres was adapted from Chapman et al.[151]. The goal of the original protocol was to purify curli fibres from the biofilm matrix of an *E. coli* strain that does not produce (pEtN-)cellulose. However, reciprocally, the same protocol can be used to purify pEtN-cellulose from the biofilm matrix produced by the *E. coli* AP329 strain, which does not produce curli. The protocol written below describes the purification of curli fibres.

Biofilms were grown for one week on salt-free LB agar at 28°C. A total of 27 biofilms (or 3 Petri dishes of 9) are necessary to obtain approximately 1 g of biofilm material. Biofilms were scraped from their agar substrate and transferred into an Eppendorf tube. They were blended on ice for 1 min, five times at intervals of 2 min, using a homogeniser (Xenox MHX 68500). The homogenized sample was centrifuged twice at 5000 g for 10 min at 4°C. After adding 150 mM NaCl to the supernatant, the curli proteins were pelleted at 12.000 g for 10 min at 4°C. The curli pellet was then re-suspended in 1 mL of buffer (10 mM tris(hydroxymethyl)aminomethane (Tris) pH 7.4, 150 mM NaCl) and incubated on ice for 30 min before another centrifugation step was performed (16.000 g, 4°C, 10 min). This washing procedure was repeated three times. The pellet was re-suspended in 1 mL

*The curli and pEtN-cellulose fibres were obtained from Dr. Macarena Siri. The procedure is given here to provide a complete description of the experimental protocol.

of 10 mM Tris pH 7.4 and pelleted again (16.000 g, 4°C, 10 min). Then the pellet was re-suspended in 1 mL of 10 mM Tris pH 7.4 and centrifuged (17.000 g, 4°C, 10 min, 2x). The pellet was then re-suspended in 1 mL 1% (v/v) sodium dodecyl sulfate (SDS) solution and left to incubate for 30 min. Curli fibres were pelleted at 19.000 g for 15 min at 4°C and the resulting pellet was re-suspended in 1 mL of ultrapure water. Washing with water was repeated three times. The last resuspension was performed in 0.1 mL ultrapure water with 0.02% sodium azide. The resulting suspension was stored at 4°C.

4.4.3. ATR-FTIR measurements on purified pEtN-cellulose and curli fibres

Both curli and pEtN-cellulose fibres were analysed separately in the presence $FeCl_3$, $AlCl_3$, $ZnCl_2$, $CaCl_2$ and ultrapure water. For each fibre and each solution, 3 to 4 replicates were recorded. Only one replicate was recorded for ultrapure water because the fibres were already characterized by Dr. Siri in this condition. The stock solutions of the respective salts (220 mM) were diluted to a concentration of 400 µM. The pH values of the resulting solutions were 3.0 ($FeCl_3$), 4.3 ($AlCl_3$), 5.9 ($ZnCl_2$) and 6.5 ($CaCl_2$). The fibre suspensions were then added to the salt solutions or ultrapure water in a 1:9 (v/v) ratio, yielding a final salt concentration of 360 µM. The suspensions (3 µL) was then transferred onto the diamond crystal surface of the spectrophotometer and completely dried under N_2 flow. Similarly to the measurements performed on biofilms, every measurement consisted of 64 accumulations recorded at 25°C, between 7500 and 600 cm^{-1} with a spectral resolution of 0.4 cm^{-1}.

Both pEtN-cellulose and curli spectra were processed using the Kinetic software, running on MATLAB (7.6 (R2008a), MathWorks) and developed by Dr. Erik Goormaghtigh[152,153] at the Structure and Function of Membrane Biology Laboratory, Université Libre de Bruxelles, Brussels, Belgium. For curli fibres, the water vapour and the amino acid side chains were subtracted. The spectra were baseline corrected and normalised to a 0-1 range between 1700 and 1600 cm^{-1} with respect to the maximum at 1623 cm^{-1} (4.4.1). Spectra were Fourier self-deconvoluted using a Lorentzian line shape (full width

at half height (FWHH) = 20 cm^{-1}) and a Gaussian line shape (FWHH = 13.33 cm^{-1}) for the apodization, yielding K = 1.5 for the ratio of the Lorentzian and Gaussian FWHH[154]. The second derivative was calculated from the deconvoluted spectra for band assignment. The bands identified from the deconvoluted spectra and their second derivatives were used as the initial parameters for a least-squares iterative curve fitting of the original IR band (K = 1) in the amide I region, using mixed Gaussian/Lorentzian bands[150]. The peak positions of each identified individual component were constrained within ±2 cm^{-1} of the initial value[150].

Table 3. FWHH input values in cm^{-1} and their physically plausible ranges expected for each type of secondary structure[150,154,155]

Secondary structure component		FWHH input (cm^{-1})	Lower limit (cm^{-1})	Upper limit (cm^{-1})
β-sheet	High wavenumber component	9	8	11
	Low wavenumber component	17	14	19
α-helix/ random		20	5	30
Turns		20	5	30

For pEtN-cellulose fibres, the water vapour was subtracted. The spectra were corrected for the baseline and normalised to a 0-1 range over the plotted wavenumber, as previously mentioned for biofilms (4.4.1). In particular when plotting the pEtN-cellulose spectra between 4000 and 600 cm^{-1}, the contribution of the metal salt solutions were such that the maximum peak varied across spectra.

5. Influence of metal cations on the viscoelastic properties of *Escherichia coli* biofilms

5.1. Results

Biofilms that synthesize both curli and pEtN-cellulose (AR3110) showed the typical morphology with three-dimensional wrinkles (Figure 5) [16]. In contrast, the strains producing only curli (W3110) or pEtN-cellulose (AP329) showed different morphologies in agreement with the literature[16,46]. When co-seeding W3110 and AP329, the biofilm morphology was similar to AR3110, suggesting that the structural and mechanical properties of the matrix are at least partly restored in the co-seeded biofilm.

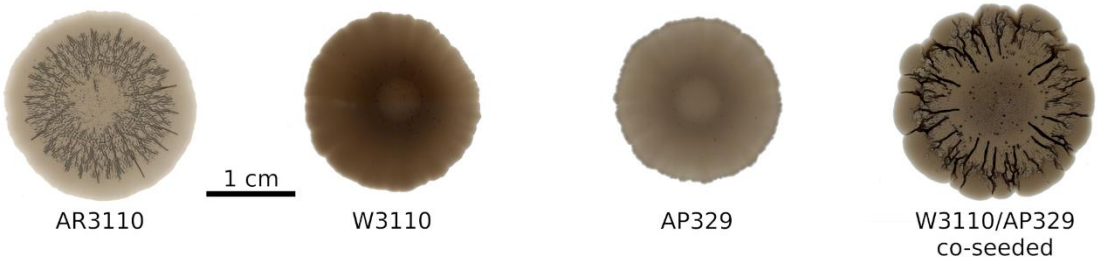

Figure 5. Phenotypes of the different *E. coli* strains. AR3110 produces both curli fibres and pEtN-cellulose. W3110 expresses only curli, while AP329 synthesizes only pEtN-cellulose. The sample W3110/AP329 shows the biofilm morphology obtained when W3110 and AP329 were co-seeded, i.e. when curli and pEtN-cellulose were produced by different bacteria. (W3110/AP329 co-seeded photograph courtesy of Ricardo Ziege)

For measuring the viscoelastic properties, the biofilms were harvested and mildly homogenised by stirring. It has previously been suggested that homogenized *P. aeruginosa* biofilms quickly regain their viscoelastic properties when probed with shear rheology[56]. Here, homogenisation was necessary to mix the harvested biofilms with the metal cation solution of interest. As trivalent metal ions, Al(III) and Fe(III) were chosen for their known effects on the viscoelastic properties of *B. subtilis* and *P. aeruginosa* biofilms. Fe(III) has coordination numbers ranging from 4 to 6[156], Al(III) has 4 and 6, rarely 5[157]. Zn(II) and Ca(II) were chosen as two bivalent cations with different preferred coordination numbers (Zn(II): 4-6, Ca(II): 6-8)[156,158].

5.1.1. Selection of measurement conditions and data range for rheology analyses

Before probing the influence of bivalent and trivalent cations on the mechanical properties of the different biofilms, the measurement conditions were first established using neat AR3110 biofilms. As previously stated, the amplitude sweeps consisted of three cycles and the data presented were extracted from the ascending amplitude sweep in the second cycle (Figure 6A). The plateau values for both moduli were similar for the three cycles, with no systematic increase or decrease of the values between the first and subsequent cycles (Annex Figure 23). This confirms that also homogenized *E. coli* biofilms recover their stiffness within a few min after yielding, similarly to what was observed for *P. aeruginosa*[56].

To assess the validity of the strain amplitude sweeps, frequency sweeps were performed. The storage and loss moduli showed a limited influence of the oscillation frequency over a range from 1 to 100 rad s^{-1} (Figure 6B). Similar viscoelastic properties were observed for frequency sweeps with increasing and decreasing frequency and for samples with and without the addition of 10% (v/w) ultrapure water (Annex Figure 24). Consequently, in the amplitude sweeps, the plateau moduli G'_0 and G''_0 were always obtained from the linear viscoelastic range (Figure 6A) at a frequency of 10 rad s^{-1}. Frequencies below 1 rad s^{-1} were also tested but the sample showed a strong increase in the values of both moduli, supposedly due to sample drying (Annex Figure 25).

The effect of drying was subsequently investigated in more detail. The focus was on the time window of the second ascending amplitude sweep, from which the shear moduli were derived. Although the sample appears to be continuously drying throughout the experiment, the drying effect accounts for only 10% of the increase in G'_0 during this period (Figure 6C). Interestingly, the values for both moduli ($G'_0 \approx 30$ kPa and $G''_0 \approx 3$ kPa) are significantly lower than those measured for the *E. coli* strain MG1655 ($G'_0 \approx 100$ kPa and $G''_0 \approx 20$ kPa), which produces a matrix with a different composition (curli and PGA, a linear polymer of β-1,6-N-acetyl-D-glucosamine)[159].

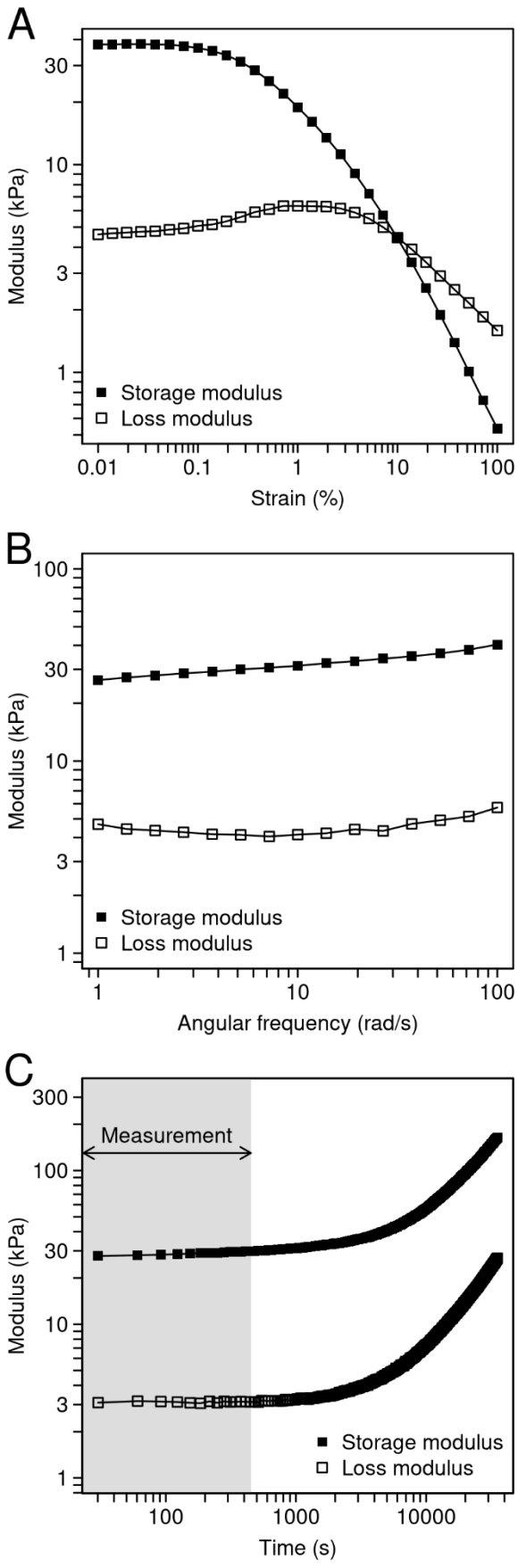

Figure 6. Viscoelastic properties of AR3110 biofilms, producing both matrix fibres. A: Strain amplitude sweep (ω = 10 rad s^{-1}) of a biofilm where no solution was added. B: Frequency sweep (γ = 0.02%, decreasing frequency) of a biofilm where no solution was added. C: Evolution of the storage and loss moduli, measured with constant strain amplitude (γ = 0.02%) and frequency (ω = 10 rad s^{-1}). The biofilms were measured without any solution added and the measurement was preceded by one amplitude sweep (not shown). The time interval of the analysed ascending amplitude sweep (7.5 min) is labelled in grey.

5.1.2. Dispersion of the storage and loss moduli upon dilution

Adding metal ions in solution increases the water content of the biofilm-cation mixture. Changes in biofilm properties are thus a combined effect from the addition of water and from the respective metal ion. To disentangle these effects, possible changes in biofilm viscoelasticity in response to the addition of 10% (v/w) ultrapure water were investigated first. In general, both storage and loss moduli decreased by approximately one order of magnitude. For example, for AR3110 biofilms, the storage modulus decreased from 30 to 4 kPa (Table 4) and the loss modulus was lowered from 3 to 0.4 kPa (Table 5). This indicates that the architecture of the biofilm matrix is partially destroyed when the sample is stirred after the addition of water. This observation relates to results obtained in *P. aeruginosa* biofilms where the addition of 5% (v/w) water led to a stiffness decrease of 40%[56]. In most cases, the addition of water also increased the dispersion (coefficient of variation) in both moduli (Tables 4, 5, Annex Tables 17, 18). Considering the overall large dispersion between biofilm samples grown on different days and as a result of stirring, the following measurements to probe the effect of metal ions were performed with an internal control. Each metal containing sample was compared to a sample containing 10% (v/w) ultrapure water that was grown in the same Petri dish (Figure 7A; Materials and Methods).

Table 4. Median storage moduli (G'_0) before (-) and after (+) dilution of the biofilms with 10% (v/w) ultrapure water ($n_{expriments} \geq 3$). The G'_0 values of all individual experiments are reported in Annex Table 17.

Matrix composition	**Curli pEtN-cellulose**		**Curli**		**pEtN-cellulose**		**Curli pEtN-cellulose (mixed)**		**Curli pEtN-cellulose (co-seeded)**	
Water	**-**	**+**	**-**	**+**	**-**	**+**	**-**	**+**	**-**	**+**
Median G'_0 (Pa)	28267	4510	16533	1580	18200	576	31267	2673	51167	5617
Median absolute deviation (MAD) (Pa)	4567	863	6517	367	9043	385	4267	1250	3233	2717
Coefficient of variation (MAD/median) (%)	16	19	39	23	50	67	14	47	6	48

Table 5. Median loss moduli (G''_0) before (-) and after (+) dilution of the biofilms with 10% (v/w) ultrapure water ($n_{expriments} \geq 3$). The G''_0 values of all individual experiments are reported in Annex Table 18.

Matrix composition	**Curli pEtN-cellulose**		**Curli**		**pEtN-cellulose**		**Curli pEtN-cellulose (mixed)**		**Curli pEtN-cellulose (co-seeded)**	
Water	**-**	**+**	**-**	**+**	**-**	**+**	**-**	**+**	**-**	**+**
Median G''_0 (Pa)	3297	442	2047	170	2187	61	3413	225	6390	695
Median absolute deviation (MAD) (Pa)	1033	83	657	14	1007	46	277	91	160	149
Coefficient of variation (MAD/median) (%)	31	19	32	8	46	75	8	40	3	21

5.1.3. Effect of trivalent cations on the shear modulus of AR3110 biofilms

To address the great variability between samples grown on different Petri dishes, bacteria were always seeded such that biofilm material sufficient for two samples could be obtained from the same Petri dish. After one week of growth, the biofilms were scraped from the agar. Prior to the rheology measurements, one sample was incubated with ultrapure water, while the other one was incubated with the solution of interest. This allowed a systematic comparison dish per dish between the samples incubated with a solution and the respective control samples incubated with water (Figure 7A).

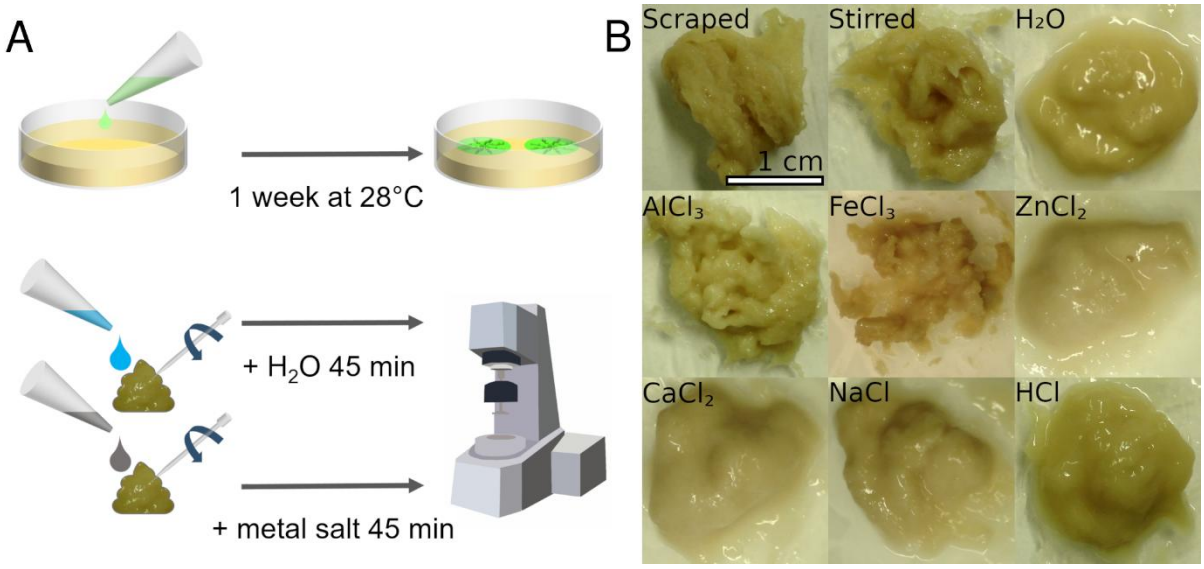

Figure 7. Sample preparation and texture. A: Biofilms were inoculated on salt-free LB agar and grown for one week at 28°C. One Petri dish contained material for two rheology experiments. After harvesting two samples of the biofilm material, the solution of interest was added to one sample and the sample was gently stirred with a pipette tip. Ultrapure water was added to the second sample, which was then treated in the same way. Both samples were incubated for 45 min, followed by the rheology measurements. B: Texture of AR3110 biofilm material after stirring with various solutions. Biofilms stirred with ultrapure water (H_2O), with the control solutions or solutions with bivalent metal cations appear more liquid. In contrast, the samples containing trivalent metal ions show a more solid textural appearance.

Immediately following the addition of the metal ion solutions to AR3110 biofilms, the mixtures showed a striking difference in their visual appearance (Figure 7B). The texture of biofilms containing $AlCl_3$ or $FeCl_3$ was similar to a granular paste. In contrast, the biofilm mixture appeared more fluid and smooth when $ZnCl_2$ or $CaCl_2$ was added. No such difference between bivalent and trivalent cations was observed for any other matrix composition. At this stage, the toxicity of one solution representative for each texture ($AlCl_3$ and $ZnCl_2$) was assessed. Bacterial liquid cultures were inoculated from a fragment of biofilm previously incubated with one of the two solutions and compared to their equivalent incubated with ultrapure water. This was performed for the three *E. coli* strains AR3110, W3110 and AP329. The resulting growth curves showed no effect of the incubation with whichever solution (Figure 8). This suggests that the initial number of living bacteria in the inoculated piece of biofilm was not affected by the addition of $AlCl_3$ or $ZnCl_2$. Possible losses of water during the incubation period were also measured by differential weighing and were always found to be less than 5% of the biofilm wet mass (Table 7). In practical terms, the absolute values of

water loss are close to the limit of detection of the balance. In addition, since the metal cation solutions have low pH (Table 2), the buffering capacity of the biofilms was estimated with pH-paper. After incubation with different phosphate buffers (pH = 2, 7 or 14), the pH of all resulting mixtures remained in the range of 7 ± 1 irrespective of the buffer added (Table 6).

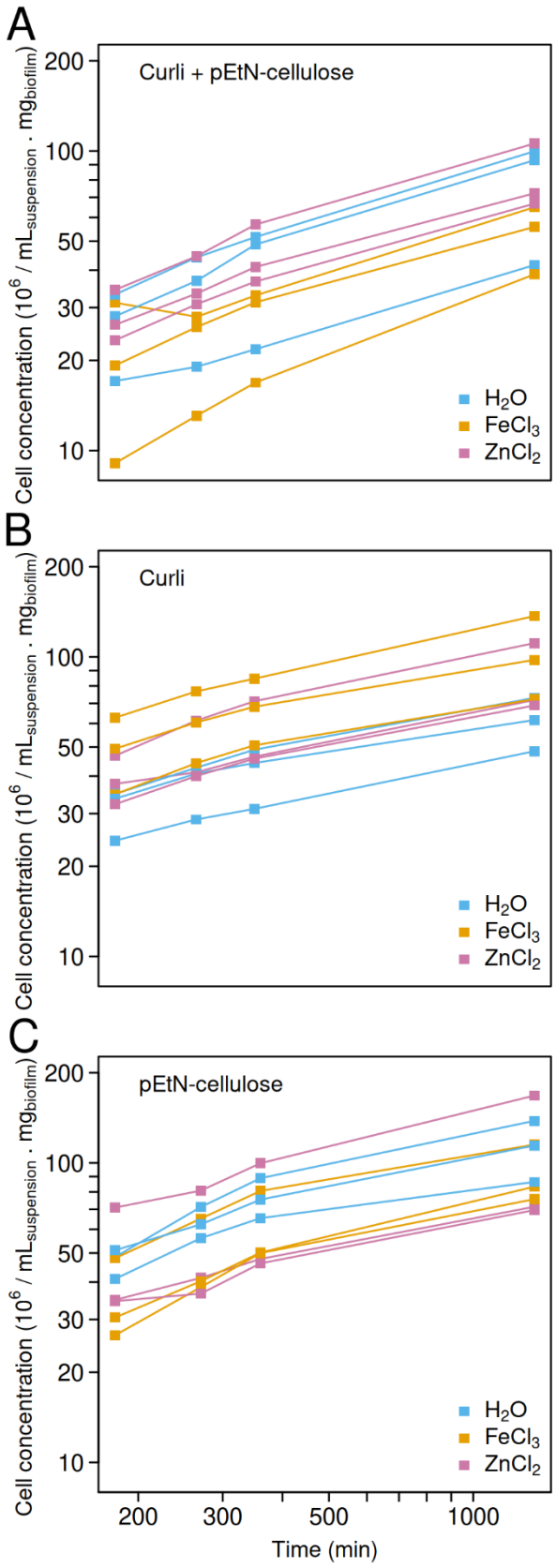

Figure 8. Control experiment to assess metal cation toxicity. *E. coli* liquid cultures were inoculated in LB medium from a fragment of biofilm that was incubated in ultrapure water or 10% (w/v) $FeCl_3$ or $ZnCl_2$. The cell concentrations in suspension are normalised to the mass of biofilm inoculated, which is assumed proportional to the initial number of cells inoculated.

Table 6. Biofilm buffering capacity after 10% (w/v) homogenization with three buffer solutions (pH = 2, 7 and 14) for three *E. coli* strains (AR3110, W3110 and AP329). The pH of the mixture was measured with pH-paper directly and after 45 min of incubation.

Matrix composition	Curli pEtN-cellulose		Curli		pEtN-cellulose	
Time (min)	**0**	**45**	**0**	**45**	**0**	**45**
Buffer pH=2	7	7	6-7	7	6.5-7	7
Buffer pH=7	7-8	7-8	7	7	7	7
Buffer pH=14	8	7-8	7-8	7-8	7.5	7

Table 7. Biofilm relative mass loss through evaporation after 45 min of incubation in a Petri dish sealed with Parafilm. In bold: mass increase most likely due to measurement uncertainty.

Solution	Δm (%)	Solution	Δm (%)	Solution	Δm (%)	Solution	Δm (%)
H_2O	2.80	$FeCl_3$	2.77	$ZnCl_2$	**-2.14**	NaCl	1.75
	1.51		1.27		0.70		0.83
	2.52		4.22		2.03		3.59

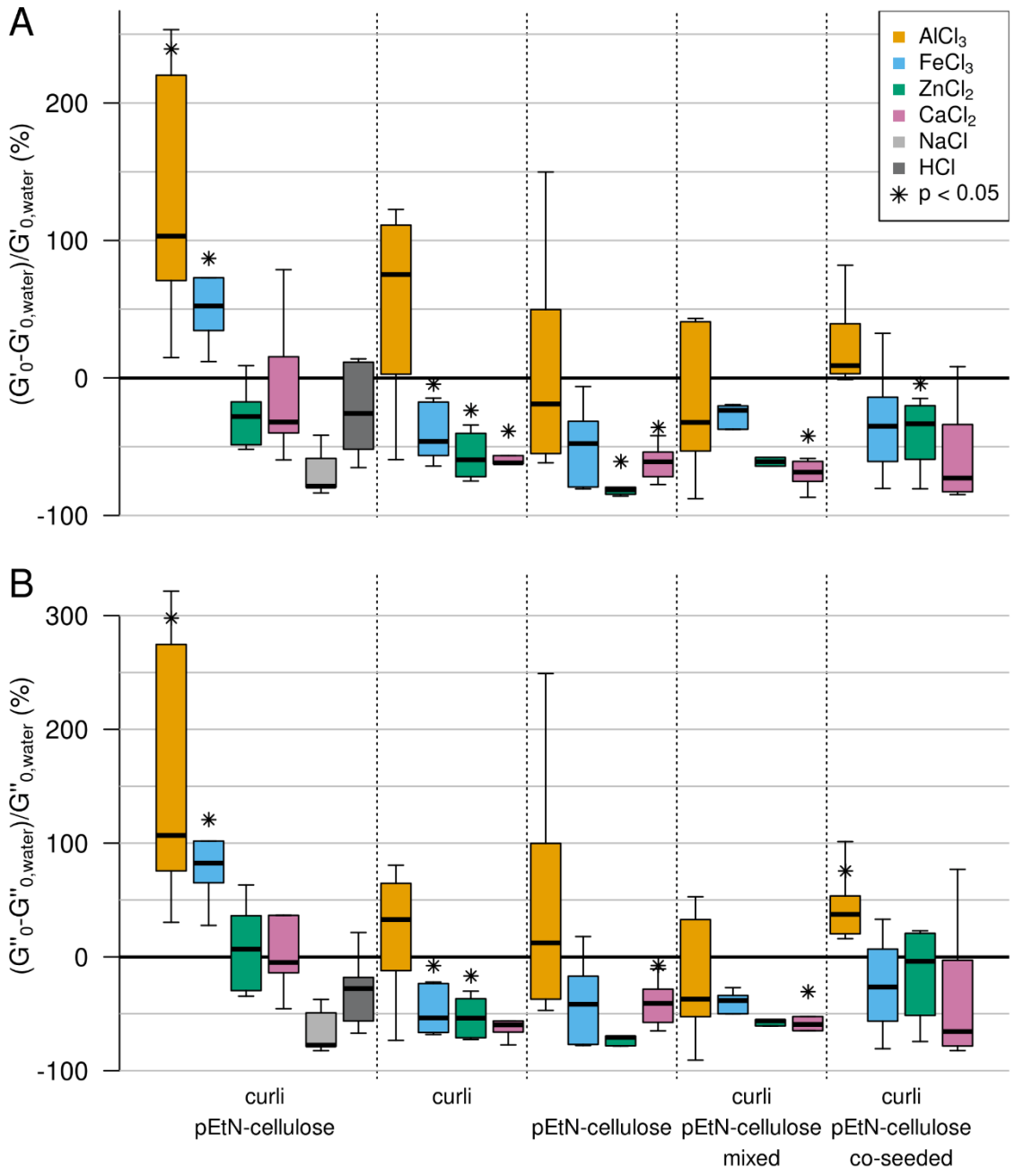

Figure 9. Effect of bivalent and trivalent metal ions on *E. coli* biofilms with different matrix compositions. A: Storage moduli. B: Loss moduli. All samples were stirred with the respective metal cation or control solution, adding 10% (v/w) of the respective solution. The box plots highlight the median of ≥4 independent experiments (see Annex Tables 19-28 for all values). The whiskers represent 1.5 times the interquartile range (IQR).

To quantify the observed texture changes, G'_0 and G''_0 were determined for all different biofilm samples incubated with the different metal ion solutions or the control solutions. Consistent with the changes in texture, the moduli also differed when the AR3110 biofilms were mixed with bivalent or trivalent metal cations. The addition of $AlCl_3$ or $FeCl_3$ increased the storage and loss moduli for

AR3110 (Figure 9). Neither the bivalent metal ions caused an increase in either modulus nor did the control solutions that mimicked the pH value or osmolality of the $FeCl_3$ solution (Figure 9).

Table 8. Statistical significance between the effect of a metal salt solution on the storage modulus (G') and the effect of water. Shown are the p-values calculated from a One-Sample Wilcoxon Signed Rank Test (μ = 0) assessing the effect of one solution on G' for each matrix composition. H_0: the variation of G' does not differ significantly from zero. p-values inferior to 0.05 in bold, in which case an arrow indicates whether the modulus increases (↑) or decreases (↓).

Matrix composition	Curli pEtN-cellulose	Curli	pEtN-cellulose	Curli pEtN-cellulose (mixed)	Curli pEtN-cellulose (co-seeded)
$AlCl_3$	↑ **0.001**	0.094	0.844	0.563	0.063
$FeCl_3$	↑ **0.031**	↓ **0.031**	0.063	0.063	0.156
$ZnCl_2$	0.063	↓ **0.031**	↓ **0.031**	0.063	↓ **0.031**
$CaCl_2$	0.563	↓ **0.031**	↓ **0.031**	↓ **0.031**	0.063
NaCl	0.063				
HCl	0.313				

Table 9. Statistical significance between the effect of a solution on the loss modulus (G'') and the effect of water. Shown are the p-values calculated from a One-Sample Wilcoxon Signed Rank Tests (μ = 0) assessing the effect of one solution on G'' for each matrix composition. H_0: the variation of G'' does not differ significantly from zero. p-values inferior to 0.05 in bold, in which case an arrow indicates whether the modulus increases (↑) or decreases (↓).

Matrix composition	Curli pEtN-cellulose	Curli	pEtN-cellulose	Curli pEtN-cellulose (mixed)	Curli pEtN-cellulose (co-seeded)
$AlCl_3$	↑ **0.001**	0.563	0.447	0.563	↑ **0.031**
$FeCl_3$	↑ **0.031**	↓ **0.031**	0.188	0.063	0.313
$ZnCl_2$	0.563	↓ **0.031**	0.063	0.063	0.563
$CaCl_2$	1	0.063	↓ **0.031**	↓ **0.031**	0.219
NaCl	0.063				
HCl	0.188				

Although statistically significant (Tables 8 and 9), the increase in stiffness (G'_0) was smaller than what was observed for other bacteria species. For example, Fe(III) and Al(III) lead to a 100-fold increase of the storage modulus of *P. aeruginosa* biofilms[56]. Moreover, a range of bivalent and trivalent metal cations increased the storage modulus of *B. subtilis* biofilms by several orders of magnitude. Such discrepancies in the magnitude of the observed stiffening might be due to the differences in sample preparation and in matrix composition. Indeed, in the case of *P. aeruginosa*, only 5% (v/w) solution was added[56], i.e. less than in our case (10%). In *B. subtilis*, the final metal cation concentration in the biofilm was 0.25 M[57], whereas it was 0.02 M in our case. Moreover, the biofilm matrix of the *P. aeruginosa* PAO1 strain contains at least three polysaccharides (alginate, Psl, and Pel)[160] and the *B. subtilis* B-1 strain produces mainly γ-polyglutamate, which all differ from the curli and pEtN-cellulose found in the *E. coli* biofilm matrix.

The effect induced by Fe(III) also depends on the matrix composition (Figure 9). While the ferric salt caused a stiffening of the biofilm sample containing curli and pEtN-cellulose fibres (+50% in G'_0), it caused a softening (-50% in G'_0) for the matrix composed of curli fibres only and no statistically significant effect for the matrix composed of pEtN-cellulose. The effect remained unclear for the co-seeded and mixed biofilms. The bivalent ions caused a significant decrease (>50%) in G'_0 for the matrices containing only one type of fibre (Figure 9) while no such effect was observed for the AR3110 strain producing both fibres. One possible explanation for the decrease in stiffness observed for most matrix-metal combinations is a non-specific osmotic effect caused by the addition of the ionic solution. The Fe(III) - and Al(III)-induced net stiffening of the AR3110 matrix overrules this softening observed in all other samples. This suggests that the curli and pEtN cellulose fibres co-produced by AR3110 bacteria form a composite material with a built-in response to trivalent cations.

5.2. Discussion

In this work, the influence of metal cations on the properties of biofilms formed by different *E. coli* strains that produce pEtN-cellulose and/or curli fibres was analysed. Using shear rheology, it was

shown that the viscoelastic properties of *E. coli* biofilms vary under the influence of metal cations. While the shear modulus generally decreased in the presence of metal salt solutions, it specifically increased when trivalent cations were added to a biofilm made from bacteria that co-produced both fibres. Metal cations trigger the formation of biofilms in *E. asburiae*, *Vitreoscilla sp.* and *A. lwoffii*[27]. Moreover, biofilms produced by *B. subtilis*, *Pseudomonas putida* and *Shewanella oneidensis* allow for the biosorption of metal ions[161]. In *E. coli* biofilms, the greatest biosorption performance was observed for Fe(III) when compared to Cd(II), Ni(II) or Cr(VI) but biofilm mechanical properties were not investigated[86]. In other species, changes in mechanical biofilm properties were observed[28], revealing that the same ion can have opposite effects in different bacterial species. While Cu(II) reinforces *B. subtilis* B-1 biofilms, it weakens those produced by *P. aeruginosa*[56,61]. This suggests a specific interplay between matrix composition and the type of ion. In a strain of *B. subtilis* producing a multi-component matrix, however, the effect of metal cations on the biofilm viscoelastic properties did not seem to be dictated by any specific matrix component[29].

To interpret the present results, a molecular understanding of the possible interaction of trivalent cations with the matrix fibres is required. No data is available concerning the interaction of Al(III) or Fe(III) with pEtN-cellulose. Yet, it was demonstrated that phosphorylation of cellulose nanofibers significantly enhances their adsorption capacity of Fe(III) ions[143]. Most interestingly, phosphorylated bacterial cellulose has a much stronger affinity for Fe(III) ions than for Zn(II), in particular in acidic solutions[162]. It was also shown that Fe(III) ions exhibit tetrahedral coordination when bound to hydroxyethyl cellulose or carboxymethyl cellulose[163]. Tetrahedral coordination is the second most common geometry for Fe(III) after octahedral, but it is also the most common coordination geometry for Zn(II)[156]. This may suggest that the overall charge is more important than the coordination geometry. This charge specificity could be explained by counter ion condensation, a phenomenon in which ions condense along a polyionic chain of opposite charge, reducing the charge density along the chain. This can in turn lead to changes in the conformation of the chains, their interactions with other polymers, and therefore affect the viscoelastic properties of the biofilm[57].

Ion condensation occurs when Manning's criterion is satisfied (see 12.1.6). According to our calculations, counter ion condensation can take place along the pEtN-cellulose chain both in the presence of bivalent or trivalent cations.

Equally little information is available about the interaction between metal cations and amyloid curli fibres. It was demonstrated that curli fibres sequester Hg(II) ions, suggesting a possible general ability to bind metal cations[140]. More broadly, the interaction between metal cations and other amyloid-forming structures was widely investigated. This includes Aβ peptides, which are the main components of amyloid plaques responsible for Alzheimer's disease. While Fe(III), Al(III) and Zn(II) co-localise with Aβ in senile plaques, their influence on the *in vitro* formation of amyloid fibrils differs. Zn(II) inhibits the formation of β-sheets while both trivalent cations trigger or stabilise them[135]. 3D-models have shown that Al(III) is almost always hexacoordinated and interacts with aspartate and glutamate residues in Aβ-complexes[136]. Zn(II) coordinates four to six ligands in Aβ-complexes, including three histidines as well as one aspartate and/or glutamate residue[137]. Although there is a lack of structural studies on Fe(III)-coordination to Aβ[138], ferric ions bind histidine more efficiently than Zn(II)[139]. A 3D-structure prediction of the major curlin subunit CsgA (AlphaFold; Figure 10) reveals close proximity of several surface-exposed histidine, glutamate and aspartate residues, suggesting that several residues are available for metal coordination[164,165].

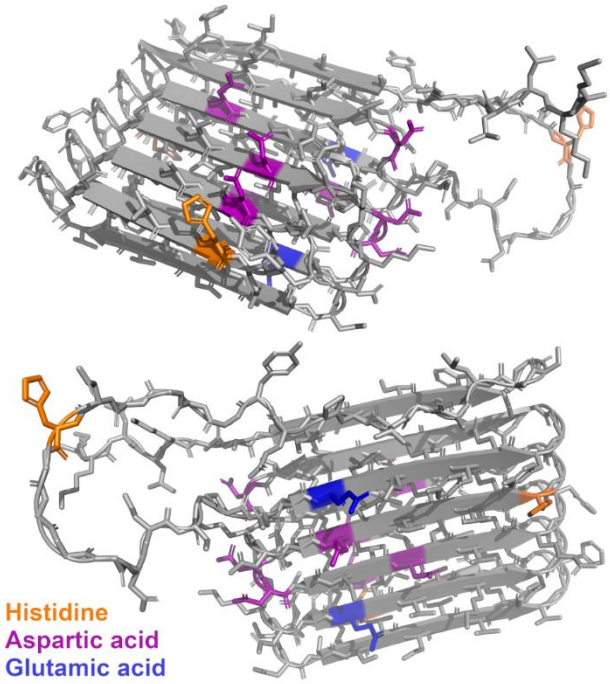

Figure 10. Tertiary structure of CsgA, the major curlin subunit, as predicted by AlphaFold (top and bottom view). Amino acids known to be involved in metal coordination are highlighted as follows: orange - histidine, purple - aspartic acid, blue - glutamic acid.

The obtained results indicate that the stiffening effect observed in the main strain producing both pEtN-cellulose and curli amyloid fibres in presence of trivalent cations does not take place in biofilms resulting from the co-seeding of the two mutant strains, each producing one fibre (Figure 9, Table 8 and 9). This experimental design is based on the assumption that the production yield of the fibres would be similar to what is observed in the strain producing both fibres. Combining them in equal proportions would then ultimately yield the original ratio between the two fibres, i.e. 75% curli and 25% pEtN-cellulose[17], although with a lower total concentration. However, either mutant strain could potentially dedicate more energy to the production of its unique fibre than is dedicated in the strain producing both. Therefore, investigating biofilms obtained from mixed bacterial suspensions of the two mutants with other ratios than 1:1 would be interesting and may eventually result in a better reconstitution of the original matrix composition. However, a spatial segregation of the two bacterial populations in the biofilm is also possible. This phenomenon was observed in *B. subtilis*[166], as well as in biofilms resulting from two competing *E. coli* strains[167]. In such a scenario, the two fibres

would not co-localise and therefore only interact at the interface between clusters of the different bacteria populations. Intriguingly, co-seeding the two mutant strains as performed in this work partially restores the phenotype of the strain producing both fibres (Figure 5). Further work will be needed to clarify the determinants of strain segregation and/or matrix fibres interactions in biofilms grown from mixed bacterial suspensions.

While the obtained results point towards a determining role of the matrix, they do not exclude a possible effect of the metal ions on the bacteria themselves. Since metal ions trigger biofilm formation in various species[27], matrix production may be regulated by the presence of metal ions. However, considering the timescale of the performed experiments, altered expression of matrix components is considered to play a minor role. Bacteria may further respond to reduce a possible toxic effect of heavy metal ions. For planktonic *E. coli* cells, it was shown that Fe(III) and Al(III) in a concentration of 0.01 mM reduce the number of colony forming units by 50%[145]. While it appears likely that biofilms provide protection against heavy metal toxicity, as demonstrated for *P. aeruginosa*[168] and suggested in the shown control experiment (Figure 8), it cannot be fully neglected that these cations also have an effect on *E. coli* cells in biofilms. It is reasonable to assume, however, that the viscoelastic biofilm properties are not significantly altered by the appearance of non-viable bacteria as bacterial cells can most likely be considered as particles in a composite material. Most importantly, toxicity would affect all strains equally while a clear difference is observed between strains producing different matrix fibres. Similar to the condensation discussed at the fibre scale, aggregation of the negatively charged bacteria *via* neutralisation by the metal cations is also to consider. In *E. coli* suspensions monitored with dynamic light scattering, 10 µM Fe(III) or Al(III) showed little to no effect on cell size distribution. Thus, if they caused aggregation, the formed aggregates are not big enough to be distinguished from individual cells[145]. However, the metal ion concentrations that were used in the investigated biofilm samples were much higher (20 mM). Moreover, the cell concentrations in suspension and in biofilms are not necessarily comparable. Cell

aggregation by trivalent cations can therefore not be excluded. Yet, similar to the effect on cell viability, cell aggregation - if taking place - would not distinguish between matrix compositions.

Osmolarity may also play a role as *E. coli* K-12 were shown to rapidly adapt (within a few min) to increases in osmolarity by uptake of potassium ions. In doing so, they maintain an internal osmotic pressure superior to that of the environment, which is necessary for growth[169]. After 45 min of incubation however, osmolarity-triggered bacteria shrinking is no longer expected to impact biofilm mechanics. While bacteria growth could also be affected by changes in osmolarity, this should not play a role within the time scale of our experiments. Considering the whole biofilms as complex hydrogels, they could potentially experience swelling upon exposure to higher osmotic pressures. This would in turn affect their viscoelastic properties since their modulus of elasticity is negatively impacted by swelling[170]. In theory, such swelling could partially explain the non-specific decrease in stiffness observed upon exposure to most solutions (Figure 9). However, the amplitude of the decrease (as far as -50% in G'_0) is hardly compatible with the little amount of water added (10% in mass, i.e. about 10% in volume). The excess of water observed around the material after mixing with bivalent ion solutions but not with trivalent ones, indicates that an equilibrium in the swelling is not reached in all cases (Figure 7B). Together with the greater complexity of the biofilm material, these swelling differences make the impact of osmotic pressure changes on biofilm stiffness delicate to assess.

6. Contribution of the biofilm macroscopic architecture to its viscoelastic properties

6.1. Results

6.1.1. Microindentation

In order to investigate the contribution of each matrix component to the overall stiffness of the biofilm, various *E. coli* strains with different matrix compositions were cultured. AR3110 produces both pEtN-cellulose and curli amyloid fibres and yields biofilms with a skin-like texture[171]. W3110 produces only curli and yields biofilms with a paste-like texture while AP329 produces only type pEtN-cellulose and is characterised by a glue-like texture[171]. These two strains were co-seeded in a 1:1 ratio in an attempt to restore the phenotype of AR3110. Indeed, the skin-like texture as well as some characteristics of the phenotype (e.g. radial wrinkles) were partially recovered. AP470 produces both curli and non-modified cellulose and results in a paste-like texture. AP472 produces only non-modified cellulose and AR198 produces neither fibre. These last two strains, both lacking curli, yield biofilms with a glue-like texture[171].

A possible correlation between those textures, presumably resulting from the matrix composition and the viscoelastic properties of the biofilm material was investigated by means of microindentation. A 50 µm diamond indenter tip was used to ensure a contact area large enough to cope with the heterogeneities of the biofilm. The indented area encompasses tens of bacteria, embedded in their matrix[171]. Data was already recorded before the indenter made contact with the biofilm surface (displacement < -100 µm) where an attractive force between the biofilm and the indenter tip was detected. Upon contact, the biofilm was indented. To estimate the elastic properties of the biofilms, only the load-displacement curves with a displacement from 7 to 30 µm were considered. The indentation curves were fitted with a Hertz model to calculate the reduced Young's modulus (see Materials and Methods). Moreover, adhesion energies were quantified as the area under the unloading part of the load-displacement curves.

The reduced Young's moduli obtained from the indentation curves (Figure 11A) are highest for AR3110 (~400 kPa) and W3110 (~360 kPa) (Figure 11B), i.e. the strains that produce both curli and pEtN-cellulose and only curli, respectively. Interestingly, for the biofilms co-seeded from W3110 and AP329 bacterial cultures, the stiffness in compression is reduced to almost half of those values (~200 kPa). For the other strains, all lacking curli amyloid fibres, the reduced Young's moduli are one order of magnitude lower (~10 kPa).

Low adhesion energies are measured for biofilms producing curli amyloid fibres, i.e. 0.33 and 0.51 N·µm for AR3110 and W3110, respectively (Figure 11C). When curli are produced by only half of the bacteria (co-seeded), slightly higher energies of 0.61 N·µm are detected. Even higher adhesion energies are detected for all strains lacking curli. For the pEtN-cellulose and cellulose-only strains, the adhesion energies are 0.87 and 1.93 N·µm, respectively. For the strain lacking both fibres, an adhesion energy of 1.23 N·µm is detected. Lastly, the strain producing both non-modified cellulose and curli has an adhesion energy of 9.6 N·µm.

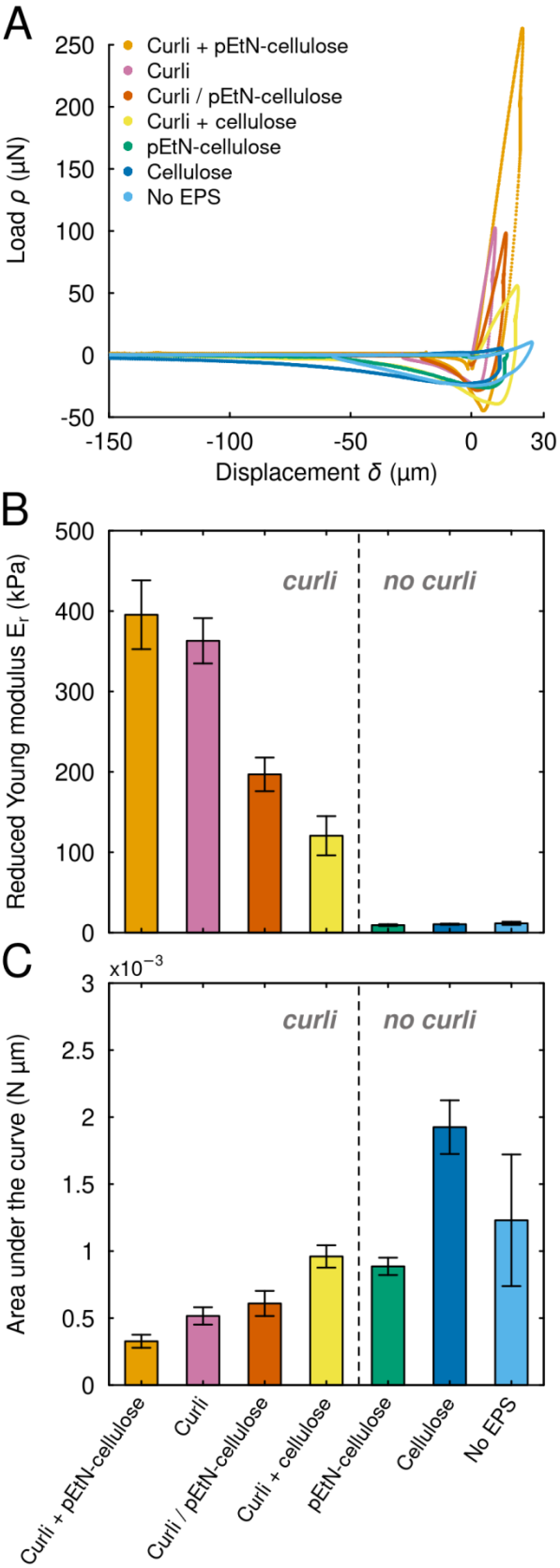

Figure 11. Microindentation of *E. coli* biofilms with different matrix compositions. A: Representative load-displacement curves of *E. coli* biofilms. B: Median values of the reduced Young's moduli. The error bars represent the standard error of the median computed by bootstrapping. C: Median values of the adhesion energies, calculated as the integrated area under the load-displacement curves for $p < 0$ ($n = 10$ to 25 individual indentation experiments from 2 to 4 different biofilm samples per condition).

6.1.2. Rheology

Another common method applied in mechanical studies of biofilms is shear rheology. While the biofilms were grown in the same conditions as for the microindentation experiments, the sample preparation and the loading geometry are fundamentally different. To perform bulk rheology, a few biofilms grown in the same Petri dish were first scraped off the surface and then mixed together to have enough material to fill the 250 μm gap between the 2 plates. Using biofilms homogenized without the addition of any solution, shear amplitude sweeps were performed to determine the mechanical response of the different biofilms to an applied shear strain. The plateau values of the storage (G'_0) and the loss (G''_0) moduli were extracted from these sweeps. When comparing the different matrix compositions (Figures 12A and 12B), the first observation is that the trend is identical for both moduli. Importantly, the differences between matrix compositions are at most a factor 2, unlike the differences observed with microindentation that spanned over more than one order of magnitude (Figure 11B). This can be attributed to the partial destruction of the matrix architecture during sample preparation.

In addition to the storage and loss moduli, also the the yield stress (τ_Y) was determined from the obtained amplitude sweeps. The yield stress represents the limit of the linear viscoelastic range, i.e. the level of stress at which irreversible plastic deformation occurs across the sample. It is also the product of the corresponding yield strain (γ_Y) and the shear modulus. It was observed that biofilms producing only curli yield at a lower stress than their counterparts, where curli are associated with (pEtN-) cellulose (Figure 12C). This suggests that curli fibres are more brittle. Interestingly, the biofilms containing both fibres yield under the same stress as those lacking both fibres (Figure 12C). Moreover, biofilms producing only non-modified cellulose resist yielding better than any other matrix composition. The flow stress (τ_F) corresponds to the level of stress where the viscous component begins to dominate over the elastic component ($G'_0 < G''_0$), i.e. where more energy is irreversibly dissipated than reversibly stored and the material predominantly behaves like a fluid. Similar to the yield stress, the flow stress corresponds to the flow strain (γ_F) multiplied by the shear

modulus. It should be noted that biofilms containing only curli or curli in association with non-modified cellulose start to flow at a lower stress than biofilms with other matrix compositions (Figure 12D). In other words, the association of curli with pEtN-cellulose brings the yield stress to a similar level as for biofilms that contain only cellulose (modified or not) or even neither of the two main components (Figure 12D).

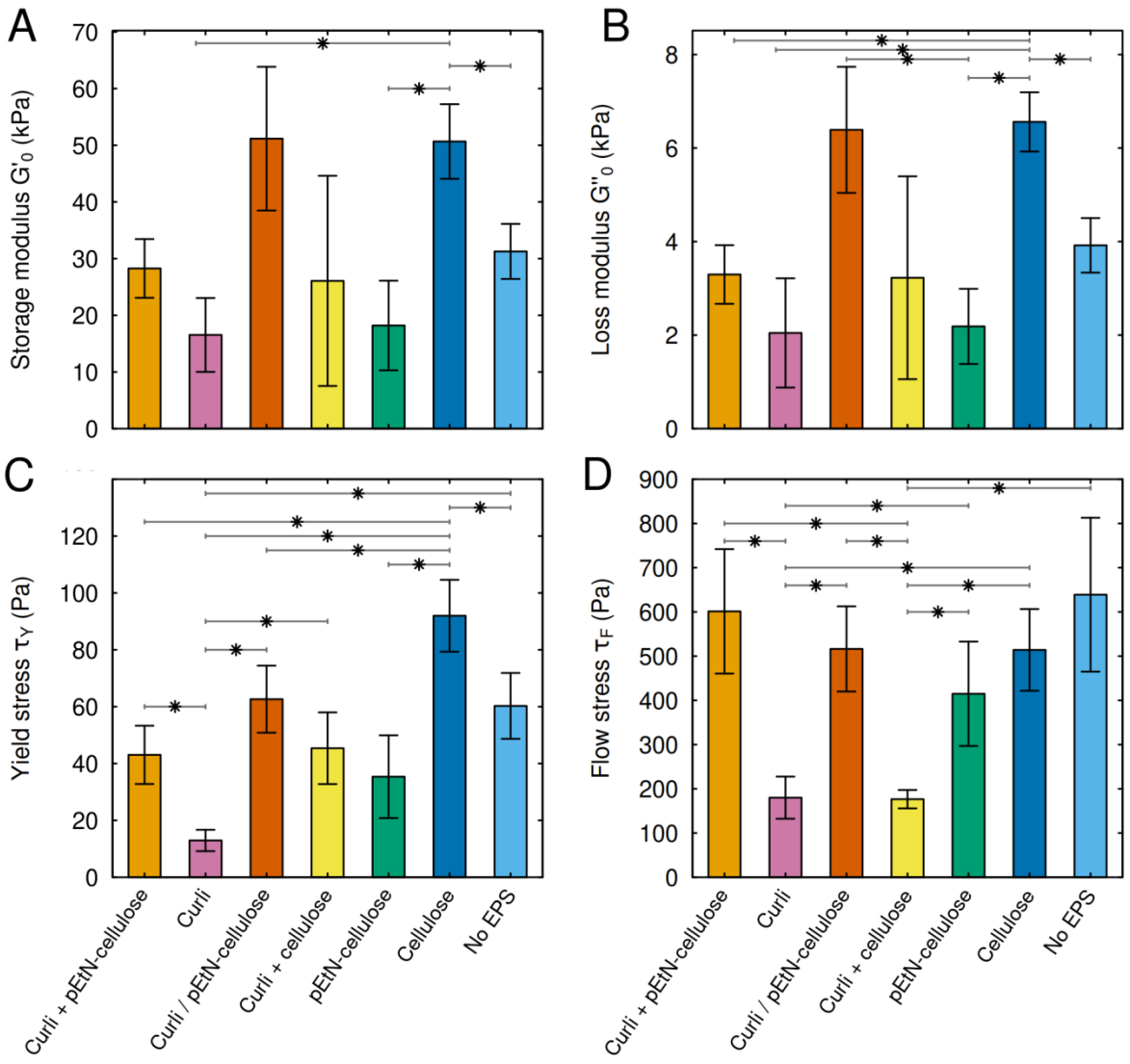

Figure 12. Rheology of *E. coli* biofilms with different matrix compositions. Data in the four bar plots were extracted from the same shear strain amplitude sweeps (ω = 10 rad s^{-1}, γ = 0.01 to 100%, *: p-value=0.1). A: plateau value of the storage modulus. B: plateau value of the loss modulus. C: yield stress. D: flow stress. The biofilms were measured without any solution added. The error bars represent the standard error of the median computed by bootstrapping.

Table 10. Storage modulus: p-values of the two samples Wilcoxon signed rank test.

	AR3110	W3110	Co-seeded	AP470	AP329	AP472	AR198
AR3110	1	0.2	0.7	1	0.4	0.2	1
W3110		1	0.2	0.4	1	**0.1**	0.2
Co-seeded			1	1	0.2	1	0.4
AP470				1	0.4	0.7	1
AP329					1	**0.1**	0.2
AP472						1	**0.1**
AR198							1

Table 11. Loss modulus: p-values of the two samples Wilcoxon signed rank test.

	AR3110	W3110	Co-seeded	AP470	AP329	AP472	AR198
AR3110	1	0.4	0.2	1	0.4	**0.1**	1
W3110		1	0.2	0.4	1	**0.1**	0.7
Co-seeded			1	0.7	**0.1**	1	0.4
AP470				1	0.4	0.7	1
AP329					1	**0.1**	0.2
AP472						1	**0.1**
AR198							1

Table 12. Yield stress: p-values of the two samples Wilcoxon signed rank test.

	AR3110	W3110	Co-seeded	AP470	AP329	AP472	AR198
AR3110	1	**0.1**	0.4	0.7	0.7	**0.1**	0.4
W3110		1	**0.1**	**0.1**	0.2	**0.1**	**0.1**
Co-seeded			1	1	0.2	**0.1**	1
AP470				1	0.4	0.2	1
AP329					1	**0.1**	0.2
AP472						1	**0.1**
AR198							1

Table 13. Flow point: p-values of the two samples Wilcoxon signed rank test.

	AR3110	W3110	Co-seeded	AP470	AP329	AP472	AR198
AR3110	1	**0.1**	0.7	**0.1**	0.4	1	0.4
W3110		1	**0.1**	1	**0.1**	**0.1**	0.2
Co-seeded			1	**0.1**	1	1	0.7
AP470				1	**0.1**	**0.1**	**0.1**
AP329					1	0.7	0.4
AP472						1	0.7
AR198							1

6.2. Discussion

6.2.1. Microindentation

As-grown biofilms, produced by different strains of *E. coli* with one particular matrix composition, were probed with microindentation. Biofilm stiffness appeared to be mainly determined by the presence of curli fibres rather than pEtN-cellulose. The indentation experiments also provided information concerning the adhesion of the biofilm to the microindenter tip. Adhesion primarily seems to be determined by the cellulose component and varies by up to a factor 4 between different matrix compositions. These results correspond to observations made at the molecular level by Tyrikos-Ergas *et al.*[172]. In order to study the interaction between curli and pEtN-cellulose, R5, a representative amylogenic peptide of curli was mixed with various hexosaccharides containing six glucoses and differing by the sequence of substitution of those glucoses by the pEtN-group on their carbon 6. The R amylogenic peptides then assembled in fibres, which were investigated with AFM[172]. The resulting Young's modulus was around 10 MPa, a similar value to what was already observed for CsgA networks[173], and was not impacted by the glucose substitution sequence. However, the measured adhesion varied up to five-fold depending on the substitution sequence of the glucose residues[172].

To better assess the role of both fibres, it is necessary to consider the architecture of the biofilm at a cellular level. The most elaborated architecture is observed for the strain producing both fibres

(AR3110). In the outermost zone of the biofilm (Figure 2B, chapter 2.2.3), the bacteria are encased in pEtN-cellulose-curli composite matrix[46,50,53,54]. In addition, the organisation of the fibres also differs between the two mutant strains. In the strain producing only cellulose, filaments of cellulose are observed, parallel to each other and perpendicular to the wrinkle line[53]. When only curli are present, the biofilm top layer is composed of small cells tightly surrounded in a "*honeycomb-like network*" of curli fibres[53]. From an architectural point of view, it may be hypothesised that curli fibres constitute a much denser network, both alone (W3110) and in the composite matrix formed with pEtN-cellulose (AR3110). This, in turn, correlates with their major contribution to the overall biofilm stiffness as observed with microindentation and also to the curli:pEtN-cellulose (3:1) mass ratio reported in the literature[17].

6.2.2. Rheology

When comparing the results obtained with rheology to those from microindentation, the most striking observation is the levelling of both storage and loss moduli. Young's moduli derived from the indentation curves spanned over more than one order of magnitude, mainly differing between matrices containing curli fibres or not. In contrast, the storage and loss moduli derived from amplitude sweeps vary by maximally a factor 2 and notably follow the same relative trend between different matrix compositions, i.e. both storage and loss moduli bar plots have the same shape. At low strains, the storage modulus exceeds the loss modulus and biofilms can be considered as viscoelastic solids. The storage modulus represents the deformation energy that is reversibly stored in the matrix network while the loss modulus represents the portion of deformation energy that is irreversibly lost due to viscous friction and is eventually converted to heat. In other words, the amount of energy stored and dissipated in the biofilm does not depend on the nature of the fibres composing the matrix.

It appears likely that the very similar properties of all biofilms originate from the partial destruction of the biofilm architecture during sample preparation for rheology. A dependence of the viscoelastic

properties on biofilm matrix architecture was reported for other bacterial species. Rheology experiments were conducted on *B. subtilis* NCIB 3610 biofilms under three different conditions: 1) grown on agar, scraped and transferred onto the rheometer; 2) grown in flow directly on the rheometer and 3) grown as a pellicle at the air-liquid interface on an interfacial rheometer[174]. For the third condition, apparent (storage) moduli were recalculated from the interfacial moduli after a plateau value was reached during growth. Storage moduli were similar (~1000 Pa) for the pellicle and the biofilms grown in flow. However, the storage moduli were one order of magnitude lower (100 Pa) for the biofilms scraped from the agar surface. This was the case despite the significantly higher dry mass to wet mass ratio (18.3% on agar, 8.4% for the pellicle, and 4.8% in flow)[174]. This clearly suggests that scraping negatively impacts the stiffness of the biofilm material, most likely *via* partial destruction of the matrix architecture. An even more significant impact of the homogenization step that follows scraping can thus be expected. Since the differences observed via microindentation correlated with the presence of curli, it appears likely that the loss of these differences originates from the (partial) destruction of curli fibres. Curli fibres have long been described as brittle, which contributes to the observation that the biofilm top-layer breaks into concentric rings in the strain producing only curli (W3110)[53].

A two samples Wilcoxon signed rank test was performed between different matrix compositions to compare their respective moduli (Tables 10-13). The lowest p-values are 0.1, which means 10% chance of wrongly considering a difference significant while it is not. Taking this into account, the biofilms producing a matrix containing only non-modified cellulose are significantly stiffer than the matrix producing only curli (Figure 12A). This would at first glance appear surprising when compared to the results of the microindentation measurements. Yet, this could also be explained following the same hypothesis that mostly curli fibres suffer from the sample preparation.

So far it was assumed that the observed levelling between the viscoelastic properties of different biofilms was due to a partial destruction of the matrix during sample preparation. However, this is not necessarily the case in the literature for bulk rheology experiments conducted on biofilms

produced by other bacterial species with different matrix compositions. Indeed, a clear dependence of the viscoelastic properties on matrix composition was reported in rheological experiments conducted on *B. subtilis* NCIB 3610 (matrix composition: TasA amyloid fibre, BslA hydrophobin, exopolysaccharide). These experiments showed that biofilm elasticity dropped from 1000 Pa for the wildtype to less than 100 Pa in a mutant strain lacking TasA. Similarly, the elasticity of biofilms lacking BslA dropped to 10 Pa, while it was reduced to lower than 1 Pa for the mutant strain lacking the exopolysaccharide[29]. However, rheology measurements conducted on the same strain reported a storage modulus drop from 600 to 300 Pa in a mutant lacking TasA, no significant change in stiffness for a mutant lacking BslA and a drop to 400 Pa in a mutant lacking the exopolysaccharide. In contrast, the same experiment conducted on another *B. subtilis* strain B-1 (producing mainly gamma-polyglutamate) yielded a storage modulus of 60 Pa[38]. While these results underline the contribution of the matrix composition to the mechanical properties of the biofilm, they also demonstrate that different experimental conditions can result in different interpretations of those contributions. In *P. aeruginosa* (matrix composition: CdrA protein, alginate, Psl, Pel polysaccharides), it was observed that increasing Psl production (but not alginate), slightly increases the storage modulus, while increasing alginate production (but not Psl) reduces the storage modulus by more than one order of magnitude. If Psl and alginate production increases simultaneously, the storage modulus decreases only by a factor 1.7. Moreover, the Psl-induced stiffening requires the presence of CdrA, suggesting cross-linking between these components[39]. In other words, the interactions between different fibres are as crucial to the mechanical properties of the biofilms as their individual contributions.

The above-mentioned studies[29,38,39] conducted with *B. subtilis* and *P. aeruginosa* biofilms suggest that differences in viscoelastic properties arising from matrix composition are at least partially preserved after scraping and can be measured by rheology, which contrasts with our own results. Yet, while biofilms were scraped and directly transferred onto the rheometer in these studies, the protocol used here included one more step of homogenization. This extra step, originally designed to

mimic the mixing with metal salt solution (see chapter 4.2.1), is prone to induce further deterioration of the matrix architecture. Yet, while the nature of the fibres already varies between strains of the same species, it varies even more between different species. Therefore, if a given treatment leads to the destruction of curli fibres in *E. coli*, it should not necessarily have a similar effect in *B. subtilis* or *P. aeruginosa*. Finally, to add another level of complexity, the relative contributions of matrix components to biofilm stiffness also depend on the growth conditions. Charlton *et al.* have recently shown in *B. subtilis* NCIB 3610, that biofilms grown on 0.5% agar are the stiffest for a full matrix composition. On the other hand, when grown on 1.5% agar, mutants lacking either BslA or the exopolysaccharide become stiffer than the wildtype[175].

Rheology experiments also provided values for the yield and the flow stresses. The yield stress corresponds to the level of stress at which irreversible plastic deformation occurs across the sample. The same statistical test was performed and the lowest p-values were again 0.1. Considering this level of certainty, it was observed that curli significantly reduce the yield stress. This confirms our previous hypothesis regarding the brittleness of curli fibres. In addition, biofilms producing only non-modified cellulose resist yielding best. This could potentially mean that they preserved a slightly higher storage modulus because they better resist stress. Opposite contributions from two different fibres to the yield stress were also evidenced in the previously mentioned experiments on *P. aeruginosa*. Overexpression of Pel and/or Psl increased the yield stress while increased production of alginate decreased it[39]. The flow stress corresponds to the level of stress beyond which the biofilm predominantly behaves like a fluid. Biofilms containing curli only or curli in association with non-modified cellulose flow at significantly lower stress (p=0.1) than other matrix compositions. This is corrected only *via* association with pEtN-cellulose, which brings back the flow stress at similar levels to those observed in biofilms producing cellulose only or in biofilms lacking both fibres. In practice, this could mean that curli fragility makes the biofilm entirely rupture at lower stress, causing it to flow. Only the specific association with pEtN-cellulose restores the composite material behaviour, in agreement with what is observed at the phenotypic level. Indeed, the complex 3D architecture of

AR3110 (curli + pEtN-cellulose) is not observed for AP470 (curli + cellulose) that is visually more similar to W3110 (curli only). While this is certainly not a causal relation, since the macroscopic architecture was destroyed, both the flow stress resistance and the phenotype could result from a common cause, i.e. the formation of a composite material specific to the pEtN-modification of the cellulose. In other words, pEtN-cellulose could have provided the bacterial colony with a competitive advantage by increasing its resistance to flow stress. This is coherent with observations that pEtN-cellulose enhances *E. coli* curli-mediated adhesion to bladder cells and acts as a mortar under high-shear conditions, which are encountered in the bladder environment[176]. However, the putative benefit conferred by an increased flow point remains quite speculative because the same relative behaviour between matrix compositions was not observed for yielding, which in practice necessarily precedes flowing. The question remains open and could possibly be answered simply by increasing the sample size, which was rather low (n=3), thereby leading to some uncertainty.

7. Molecular interactions between metal cations and the biofilm matrix

7.1. Results

The rheology experiments introduced in the first result chapter (5.1.3) have shown that stiffening occurred specifically in the presence of trivalent metal cations and only in biofilms formed by the strain producing both pEtN-cellulose and curli amyloid fibres. This can possibly be explained by three different phenomena: 1) trivalent cations act as cross-links between both matrix fibres, in which case specific functional groups would likely be involved; 2) ion condensation could take place along the fibres, influencing their packing and thereby the overall mechanics of the biofilm material; and finally 3) the negatively charged bacteria themselves could be impacted by the presence of the positively charged ions. To clarify the contribution of these phenomena, the cation-biofilm, and later the cation-fibre interactions, were investigated by means of ATR-FTIR.

7.1.1. ATR-FTIR spectra of biofilms

In a first step, biofilms produced by the three different strains AR3110, W3110 and AP329 were investigated in the absence of any salt solution. *E. coli* AR3110 produces both pEtN-cellulose and curli amyloid fibres, W3110 produces only curli and AP329 only pEtN-cellulose. To replicate the sample preparation used for rheology, the biofilm samples were mixed with 10% (v/w) ultrapure water, as was later done with the salt solutions. In addition, biofilms were partially dried for 3 min under nitrogen flow immediately preceding the measurements (see Materials and Methods).

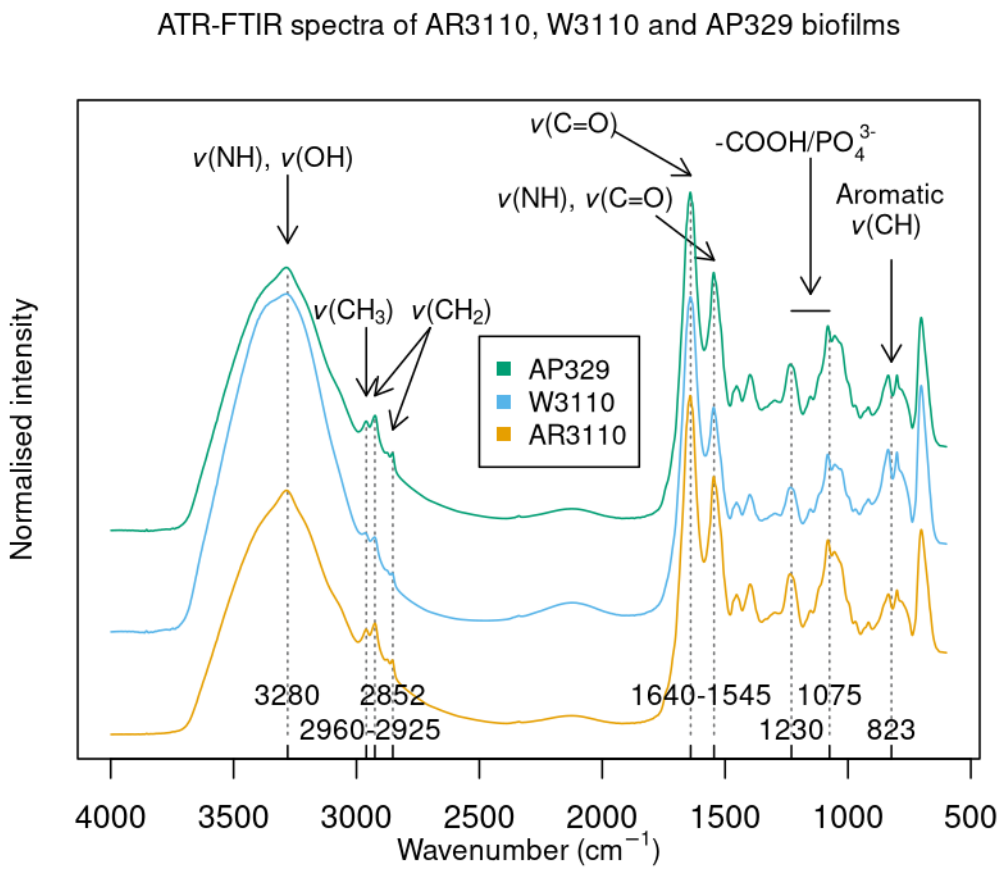

Figure 13. ATR-FTIR spectra of biofilms formed by the *E. coli* strains AR3110, W3110 and AP329 after homogenization with 10% (v/w) ultrapure water. Peaks were attributed to functional groups based on the literature (see Table 14 for more information). *ν*: stretching of the respective bonds.

The most striking observation is that the spectra are almost identical for these three strains, despite the different matrix compositions. The spectra are quite similar to *E. coli* biofilm spectra measured by Quintelas et al. (Figure 4)[86], i.e. all peaks analysed in this reference are present. The broad peak around 3280 cm^{-1} corresponds to the NH groups of proteins and the OH groups of glucose[86,177]. The two peaks at 2960 and 2925 cm^{-1} can be attributed to the asymmetric stretches of CH_3 and CH_2 in fatty acids[86,178]. The third peak at 2852 cm^{-1} corresponds to the symmetric stretch of CH_2 in fatty acids[178]. The two peaks at 1640 and 1545 cm^{-1} represent the amide I band of β-sheets and the amide II band in proteins[178]. The peaks between 1230 cm^{-1} and around 1075 cm^{-1} can be attributed to carboxyl and phosphate groups[86,178,179]. Finally, the double peak in the region around 823 cm^{-1} can indicate aromatic CH[86,178]. The peak characteristic wavenumbers gathered from the literature are summarised in Table 14. Although the broad peak at 3280 cm^{-1}, the fatty acid peaks at 2960 and

2920 cm^{-1} and the ratio between the two aromatic peaks around 823 cm^{-1} all seem to vary according to the matrix composition in Figure 13, this is not consistently the case between replicates, as can be seen from Figure 26 in the annex.

Table 14. Possible assignment of the peaks observed in the FTIR spectra of *E. coli* biofilms.

Wavenumber (cm^{-1})	Functional group	Biomolecule	Ref.
3500-3200	*v*(NH), bonded –OH	Proteins, carbohydrates	86
2957	*v*(CH_3) asymmetric	Fatty acids	178
2919	*v*(CH_2) asymmetric	Fatty acids	178
2852	*v*(CH_2) symmetric	Fatty acids	178
~1637	Amide I of β-sheets	Proteins	178
1548	Amide II	Proteins	178
1300-1067	Carboxyl and phosphate		86,179
1240	*v*(P=O) asymmetric	Phospholipids	178
1085	*v*(P=O) symmetric	DNA, RNA, phospholipids	178
900-800	Aromatic C=C, C=N, C-H Aromatic *v*(C-H)	Nucleotides	178 86

v: stretching

7.1.2. ATR-FTIR spectroscopy on biofilms mixed with metal ions

Having established that biofilms produced by the three strains AR3110, W3110 and AP329 are undistinguishable based on their FTIR spectra, the next step was to incubate these biofilms with the same solutions used for rheology ($AlCl_3$, $FeCl_3$, $ZnCl_2$, $CaCl_2$, NaCl, HCl) and to assess possible cation-dependent changes in their FTIR spectra. The resulting spectra are plotted in Figures 14 (AR3110), 15 (W3110) and 16 (AP329). The spectra corresponding to the incubation with the NaCl and HCl control solutions are plotted in the annex (Figures 27-29). Dotted lines are plotted at the wavenumbers of the previously mentioned peaks to facilitate the identification of possible shifts.

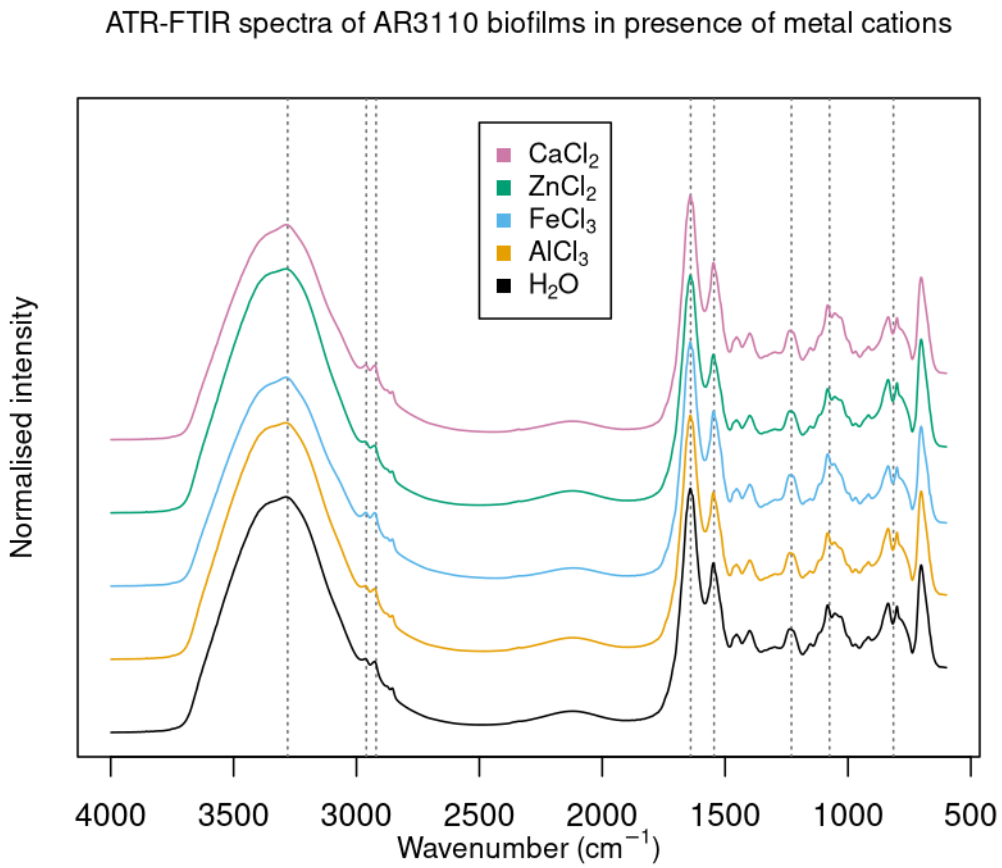

Figure 14. ATR-FTIR spectra of *E. coli* AR3110 biofilms after homogenization with 10% (v/w) solutions of different salts in comparison to 10% (v/w) ultrapure water. Dotted lines are plotted to facilitate the identification of possible shifts and correspond to the peaks introduced in Figure 13 and Table 14.

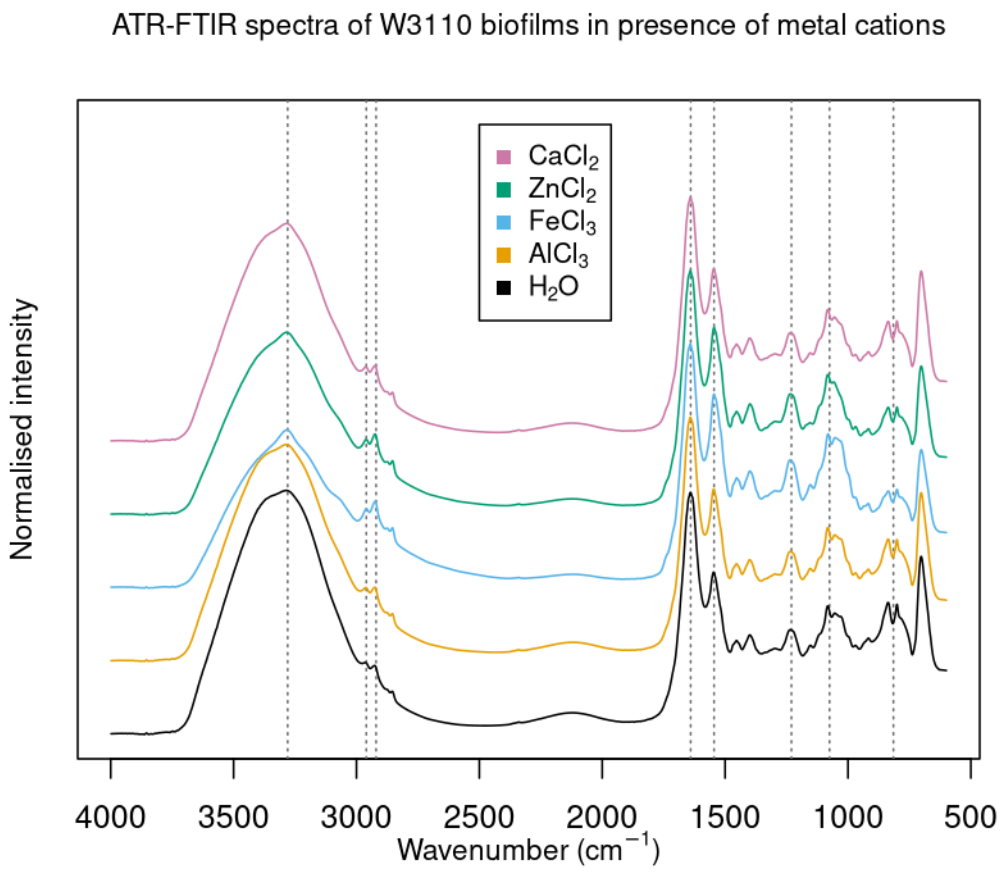

Figure 15. ATR-FTIR spectra of *E. coli* W3110 biofilms after homogenization with 10% (v/w) solutions of different salts in comparison to 10% (v/w) ultrapure water. Dotted lines are plotted to facilitate the identification of possible shifts and correspond to the peaks introduced in Figure 13 and Table 14.

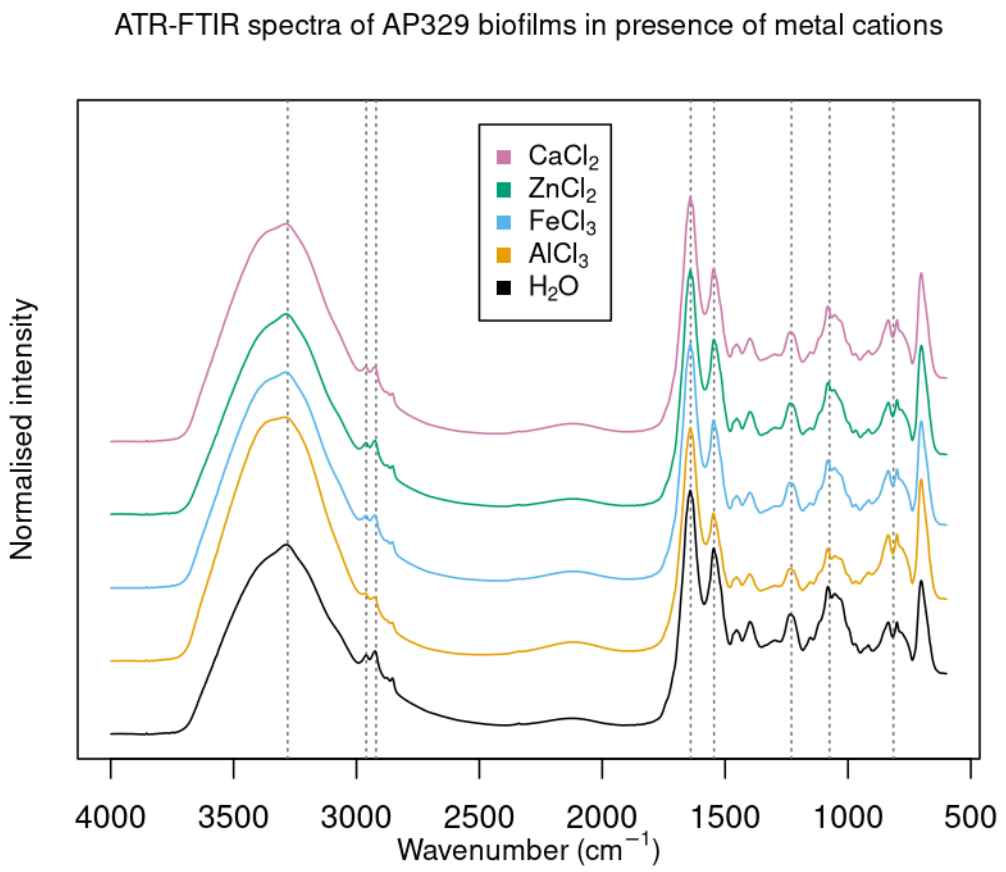

Figure 16. ATR-FTIR spectra of *E. coli* AP329 biofilms after homogenization with 10% (v/w) solutions of different salts in comparison to 10% (v/w) ultrapure water. Dotted lines are plotted to facilitate the identification of possible shifts and correspond to the peaks introduced in Figure 13 and Table 14.

Also in the presence of metal cations, the spectra of the biofilms are similar for the three strains. As indicated by the dotted lines, the maxima do not seem to shift for the different biofilm characteristic peaks (Figure 13 and Table 14). The shape of the broad peak around 3280 cm^{-1} appears to be the most variable feature. However, its shape change neither correlates with a particular solution nor matrix composition, as shown in the Annex Figures 27-29. These changes were thus not considered to be significant. Interestingly, this broad peak was one of the most affected peaks in spectra of *E. coli* biofilms grown on kaolin, after treatment with metal ions (Figure 4)[86]. The change in the ratio of the two peaks at 2960 and 2920 cm^{-1} in the strain producing only curli amyloid fibres (W3110) is another interesting change to mention. For most spectra incubated with ultrapure water or hydrochloric acid, the peak at 2960 cm^{-1} is higher while for most spectra incubated with any of the four salt solutions, the peak at 2920 cm^{-1} is higher (Figure 15, Annex Figure 28 and Table 30). A similar effect was observed by Quintelas et al. in the presence of metal ions (Figure 4). Those two

peaks correspond to the asymmetric stretching of CH_2 and CH_3 and could therefore possibly indicate an effect on lipids in the absence of pEtN-cellulose.

7.1.3. ATR-FTIR spectra of curli amyloid fibres in the presence of metal cations

The interaction between metal cations and either of the fibres could be masked by the bacteria themselves as well as other components of the matrix. To eliminate these possible contributions, purified fibres were characterized in the presence of different salt solutions. In the first step, the observed peaks were assigned with the corresponding functional groups based on the literature (Figure 17). At this stage, the spectra were analysed and plotted while preserving the contributions of the amino acid side chains.

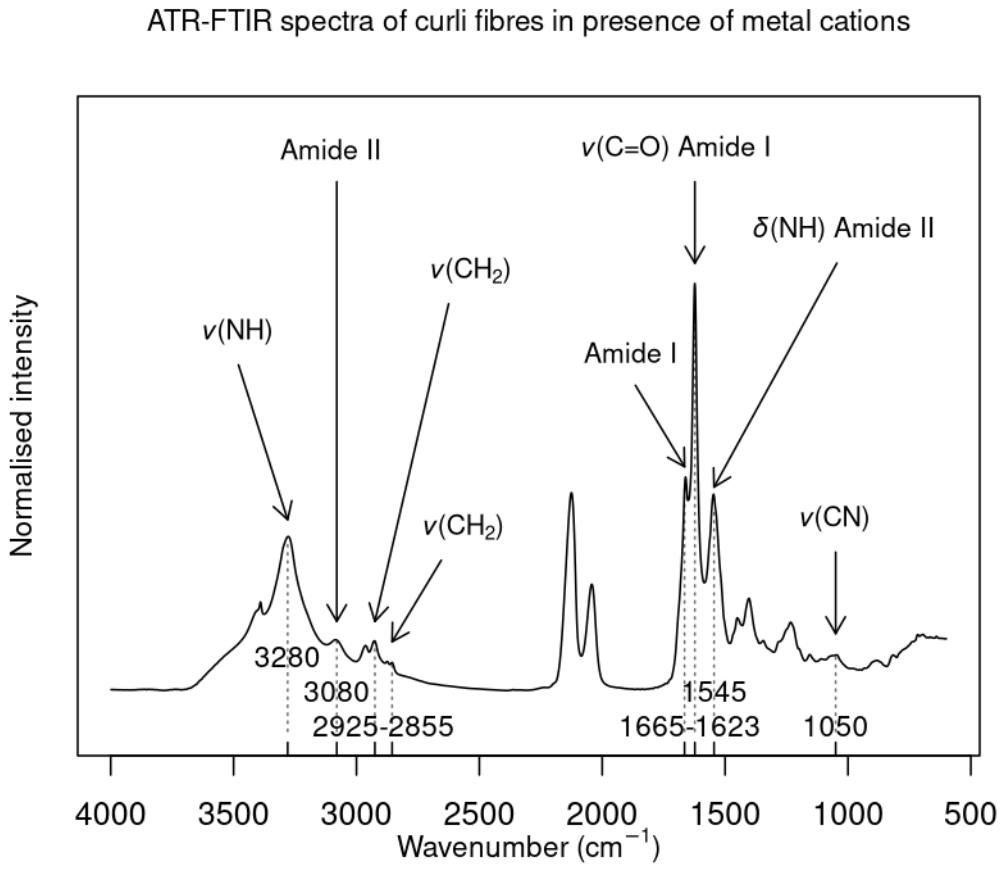

Figure 17. ATR-FTIR spectrum of curli amyloid fibres purified from *E. coli* W3110 biofilms mixed with ultrapure water. Peaks were assigned to functional groups based on the literature (see Table 15 for more information). *ν*: stretching of the respective bonds, *δ*: deformation vibration.

Most peaks can be related to functional groups known in the literature. The broad peak around 3280 cm^{-1} corresponds to the stretching of the NH groups along the polypeptide chain[86,179]. The small peak at 3080 cm^{-1} is the overtone of the amide II band[179]. The peaks at 2925 and 2855 cm^{-1} correspond to the asymmetric and symmetric stretching of CH_2 groups[179]. The peak at 1665 cm^{-1} is characteristic of the amide I band, possibly both in β-sheet and random coil conformation[179]. The peak at 1630 cm^{-1} possibly represents the stretching of C=0 in the amide I band and the peak at 1545 cm^{-1} is attributed to the deformation vibration of the NH in the amide II band[179]. Finally, the small peak at 1050 cm^{-1} could represent the stretching[177] or deformation vibration[179] of CN in aliphatic amine groups. These data are summarised in Table 15.

Table 15. Possible assignment of the peaks observed in curli fibre spectra based on the literature.

Wavenumber (cm^{-1})	Functional group	Biomolecules	Ref.
~3300	*v*(NH)	Polyglycine	179
~3100	Overtone of amide II band	Protein	179
~2925	Asymmetric *v*(CH_2)	Polyglycine	179
~2860	Symmetric *v*(CH_2)	Polyglycine	179
1675-1665	Amide I band	β-sheet structure	179
1670-1660	Amide I band	Random chain	179
~1630	*v*(C=O) in amide I band	Polyglycine	179
1550-1540	*δ*(NH) in amide II band	Polypeptide	179
1050	*v*(CN) or *δ*(CN) in aliphatic amines		177,179

v: stretching; *δ*: deformation vibration

With the goal of measuring curli amyloid fibres in the presence of metal cations, the concentration of the salt solutions (and thus the cation:curli ratio) was varied until an effect on the spectra was observed. This resulted in a cation concentration of 400 μM, as mentioned in the method section. This, for example, corresponds to a molar ratio between Fe(III) and CsgA monomers of 3.76:1 (calculations in the Annex). In the previous biofilm measurements, the contribution of the spectra of the respective salts was not considered because of the overall complexity of the sample. Here, also spectra of the salt solutions were acquired to facilitate a direct comparison of the individual components and the mixture (grey curves in Figure 18).

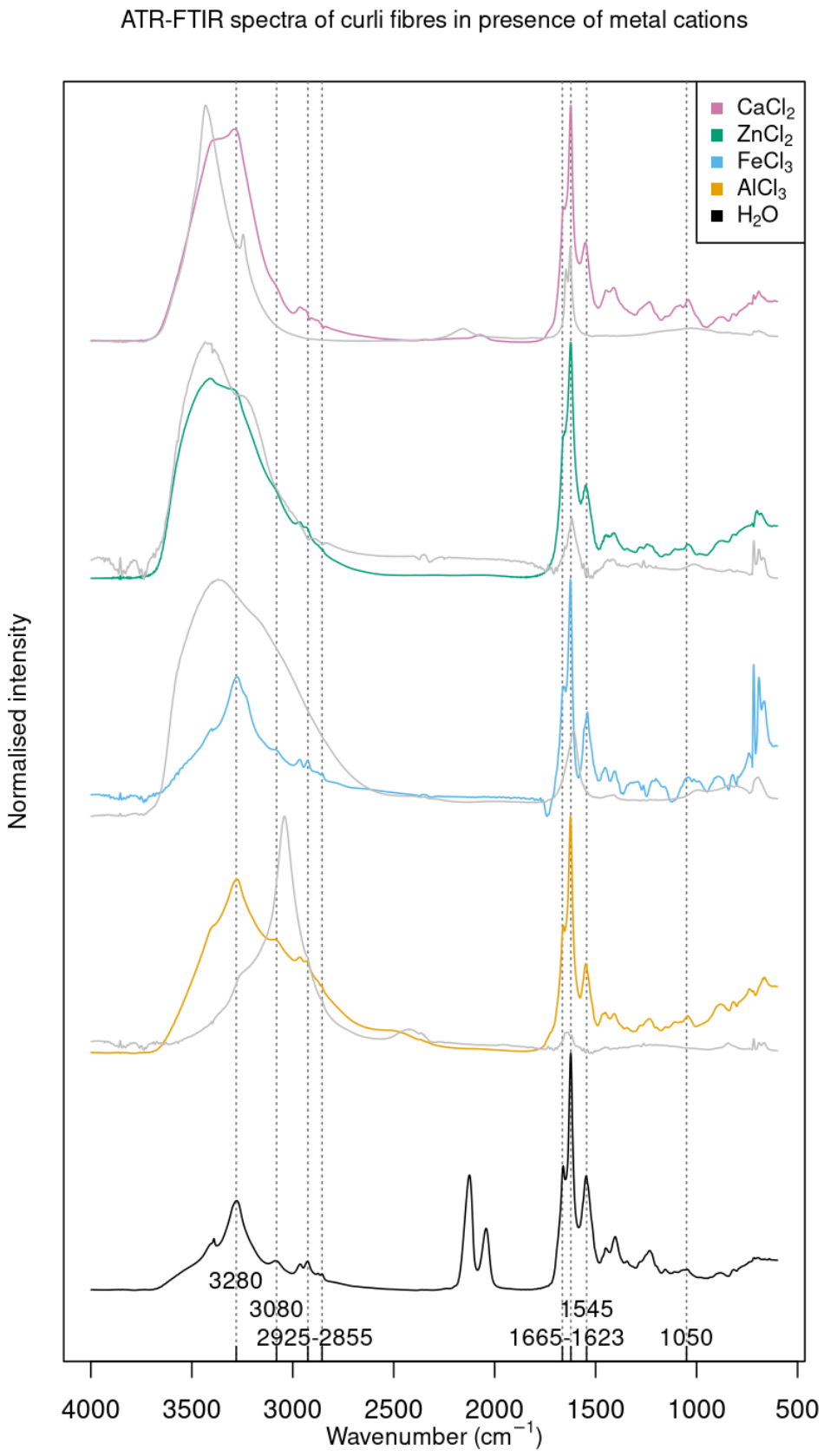

Figure 18. ATR-FTIR spectra of purified curli amyloid fibres in presence of different salt solutions and ultrapure water. Spectra of the corresponding salt solutions are plotted in grey. Dotted lines are plotted to facilitate the identification of possible shifts. The corresponding functional groups are identified in Figure 17 and Table 15.

The broad peak around 3280 cm^{-1} is hardly possible to separate from peaks in the salt solution. However, the absence of a shift in wavenumber can still be clearly seen from the chart (Figure 18). Unfortunately, the broad peaks in the salt solutions also encompass the wavenumbers (2925 and 2855 cm^{-1}) corresponding to the symmetric and asymmetric stretches of CH_2 groups. Concerning the amide I band (1665, 1623 cm^{-1}), the shapes of the peaks remain seemingly unchanged. Although small peaks are visible in that range for the spectra of the salt solutions, they appear to have no impact. The same observation applies for the amide II band δ(NH) at 1545 cm^{-1}.

7.1.4. Secondary structure analysis of curli amyloid fibres

Having qualitatively observed that the amide I band remained unchanged, an attempt was made to resolve subtle changes in secondary structure. A secondary structure analysis was thus performed in the region from 1700 and 1600 cm^{-1} to determine the relative contributions of α-helices, β-sheets, β-turns and random coils. To do so, the spectrum was deconvoluted in the aforesaid region after removal of the side chains contributions. Then, it was best-fitted with one curve for each peak that represents the contribution of one secondary structure component. When doing so, the originally overlapping peaks of the different components can be distinguished (Figure 19A). The results of this analysis on curli fibres are plotted in Figure 19B for mixtures with different metal salt solutions and ultrapure water.

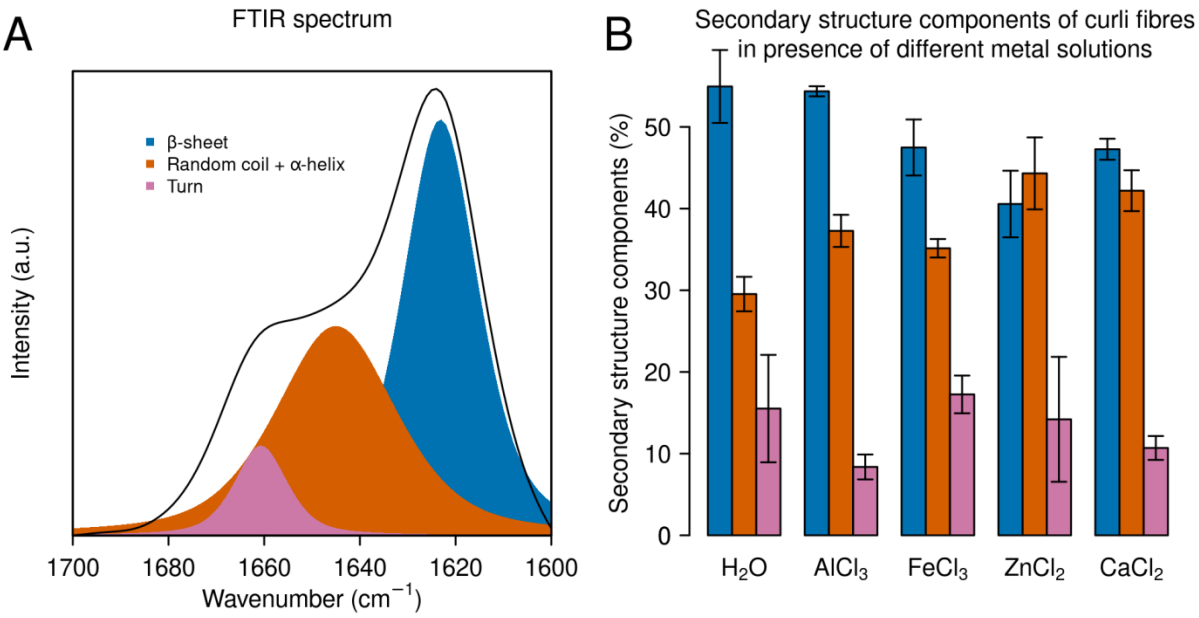

Figure 19. Secondary structure analysis based on the amide I band. A: Best-fitting of the FTIR spectrum between 1700 and 1600 cm-1 (example for $CaCl_2$) for the secondary structure component analysis. Random coil and α-helices could not be distinguished and were therefore fitted as one component. B: Distribution of the secondary structure components after mixing of the purified curli fibres with different salt solutions. The median values (n=2-4) are plotted and the error bars represent the standard error of the median computed by bootstrapping. A two samples Wilcoxon signed rank test was computed between median values representing the same secondary structures in the presence of different salt solutions, i.e. bars of the same colour. No significant differences were found (p=0.05).

As can be seen in figure 19, the different cations do also not cause any significant changes in the secondary structure of curli amyloid fibres. Considering the small number of replicates (n=2-4), the samples were not considered normally distributed and the median was plotted. The same types of secondary structure were compared for pairs of samples using a Wilcoxon signed rank test. All p-values were larger than 0.05, indicating that no significant differences exist between samples (Tables 31-33 in annex).

7.1.5. ATR-FTIR spectra of pEtN-cellulose fibres in the presence of metal cations

Just as for the curli fibres, also the spectra of purified pEtN-cellulose fibres were determined in the presence of the respective salt solutions. The amount of fibres in suspension could not be determined due to the small amount available. The salt concentration was kept the same as for the experiment on purified curli fibres. The FTIR spectra, including the peak assignments, are shown in Figure 20 and 21.

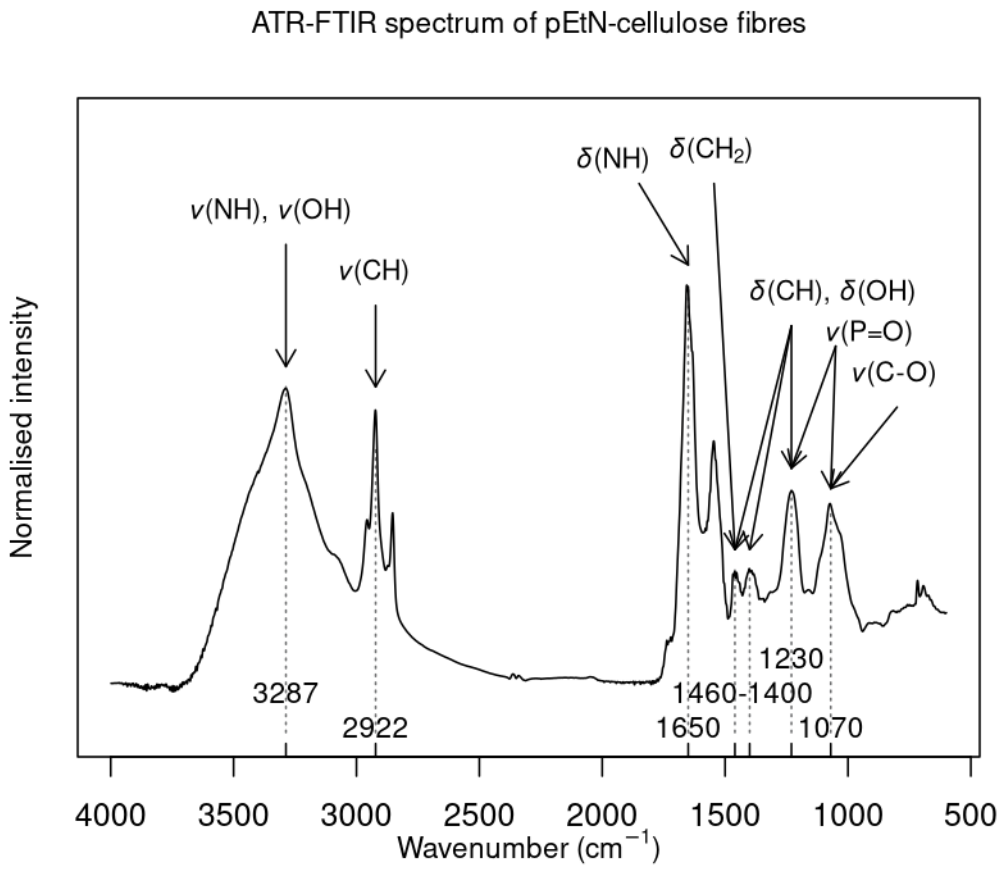

Figure 20. ATR-FTIR spectrum of pEtN-cellulose fibres purified from *E. coli* AP329 biofilms mixed with ultrapure water. Peaks were assigned to functional groups based on the literature (see Table 16 for more information). *ν*: stretching of the respective bonds, *δ*: deformation vibration.

Most of the peaks can be related to functional groups based on the literature. The broad peak around 3287 cm^{-1} corresponds to the stretching of the OH groups of glucose as well as the possible stretching of the NH group of the pEtN-modification[86,179]. The peak at 2922 cm^{-1} can be attributed to the stretching of CH in carbohydrates[179]. The peak at 1650 cm^{-1} corresponds to the deformation vibration of the primary amine[179] and must therefore represent the pEtN-modification. The three peaks at 1460, 1400 and 1230 cm^{-1} can represent deformation vibrations of CH and OH groups but the peak at 1460 cm^{-1} could also represent the deformation vibration of CH_2[179]. Moreover, the range for the numerous bands corresponding to the deformation vibrations of CH and OH are generally lower for cellulose than for other carbohydrates (Table 16). Therefore, if the peak at 1460 cm^{-1} represents $\delta(CH_2)$, 1400 cm^{-1} could also represent δ(CH). The last peak at 1070 cm^{-1} can either

represent the stretching of C-O groups[179] or the symmetric stretching of the P=O double bond in the pEtN-modification[178]. If it is the latter, then the peaks at 1230 cm^{-1} most likely represents the corresponding asymmetric stretching[178]. For clarity, the values from the literature used to assign possible functional groups to IR peaks are summarised in Table 16.

Table 16. Possible assignment of the peaks observed in pEtN-cellulose FTIR spectra based on the literature.

Wavenumber (cm^{-1})	Functional group	Biomolecule	Ref.
3575-3125	*v*(NH), *v* (OH)	Carbohydrates / cellulose	86,179
~2900	*v*(CH)	Carbohydrates	179
1650-1580	*δ*(NH), primary amine	(In this case: pEtN)	179
1480-1435	*δ*(CH_2)	Cellulose	179
1460-1200	*δ*(CH) and *δ*(OH)	Carbohydrates (numerous bands)	179
~1375	*δ*(CH)	Cellulose	179
1320-1030	*δ*(CH) and *δ*(OH)	Cellulose (numerous bands)	179
1240	*v*(P=O) asymmetric	(In this case: pEtN)	178
1160-1000	*v*(C-O)	Carbohydrates	179
1085	*v*(P=O) symmetric	(In this case: pEtN)	178

v: stretching; *δ*: deformation vibration

Now that the main peaks are identified, the spectra of the pEtN-cellulose fibres can be compared in the presence of the different metal salt solutions.

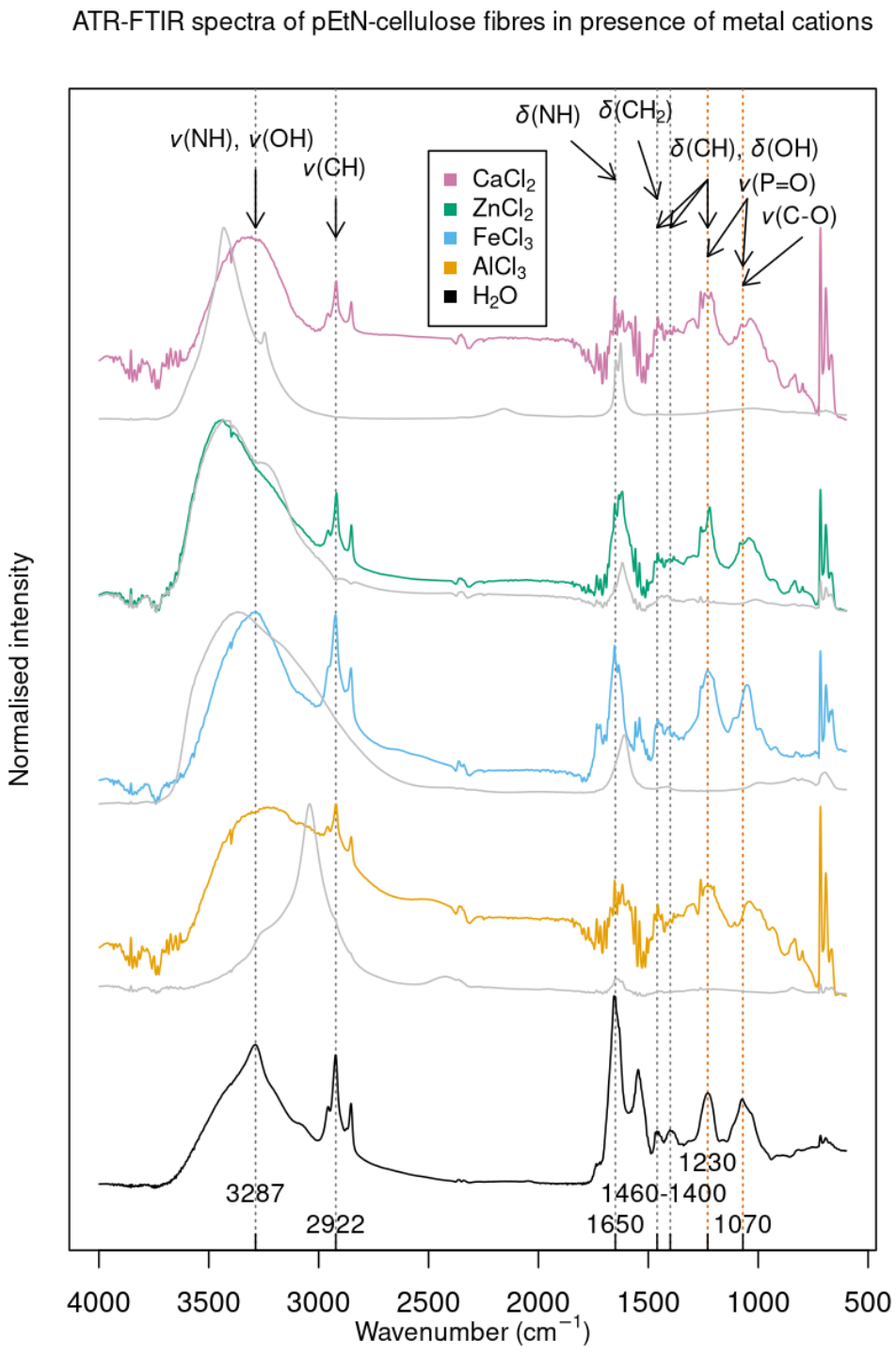

Figure 21. ATR-FTIR spectra of purified pEtN-cellulose fibres in presence of different salt solutions and ultrapure water. Dotted lines are plotted to facilitate the identification of possible shifts; in red for the peaks possibly corresponding to the P=O double bond. The corresponding functional groups are identified in Figure 20 and Table 16.

Both a change of shape and a shift can be observed for the *ν*(NH) and *ν*(OH) broad peak originally positioned at 3287 cm^{-1}. However, this wavenumber range also corresponds to a large peak in all salt solution spectra. Thus, the change of shape and shift could be a superposition of both spectra (fibre

+ solution). The triple peak centred at 2922 cm^{-1} (ν(CH)) seems unaffected both in its shape and its wavenumber. The effect on the primary amine NH deformation vibration at 1650 cm^{-1} is similar to what is observed with the first broad peak: a change of shape that coincides with a peak characteristic for the salt solutions. More meaningful could be the changes observed for several peaks at wavenumbers lower than 1500 cm^{-1}. The first two peaks at 1460 and 1400 cm^{-1} could still result from a superposition with the spectra of the metal ions. Yet, the peaks at 1230 and 1070 cm^{-1} (Figure 21, red dotted lines) significantly change in shape (shoulders appear for both) and this does not seem to be caused by the salt solutions. One explanation is that cations could have an effect on the CH and OH functional groups of the glucose residues. Another, more likely, hypothesis is that the cations stretch the P=O double bond by pulling on the electronegative oxygen. Yet, this does not seem to be cation- or even valence-specific, as can be seen from comparing the different replicates in Figure 30 of the annex.

7.2. Discussion

To obtain a molecular explanation for the metal cation-induced stiffening of biofilms (chapter 5.1.3), FTIR spectra of *E. coli* biofilms and their two main constituting fibres - curli amyloid and pEtN-cellulose - were measured in the presence and absence of salt solutions. First, the spectra of biofilms formed by the three *E. coli* strains AR3110 (curli + pEtN-cellulose), W3110 (curli only) and AP329 (pEtN-cellulose only) were investigated. No differences were observed between the spectra of the three bacterial strains. This suggests that the two main matrix fibres give little to no distinguishable contribution to the overall FTIR spectra of the entire biofilms. This correlates with recent observations that curli fibres represent only 0.146% of the biofilm dry mass[150]. Given that the curli to pEtN-cellulose ratio in the AR3110 matrix is 3:1[17], the contribution of pEtN-cellulose to the spectra is expected to be even less. This means that the spectra mostly report on the composition of the bacteria themselves. In addition, since the three bacterial strains are derived from one another (see

Materials and Methods), they can be considered to be almost identical, except for their matrix production.

Following this first observation, the spectra of the biofilms were compared after mixing them with different salt solutions. Again, the spectra were quite similar across strains. As mentioned previously, similar experiments were conducted on *E. coli* biofilms supported on kaolin in the presence of Fe(III), Cd(II), Ni(II) and Cr(VI) ions[86]. In this earlier study, the FTIR spectra of the biofilms were affected and several peaks shifted or changed in shape. The same peaks were detected in this work (Figure 13-16); however, most peaks remained unchanged. The only visible change in the presence of metal cations occurs for the peaks that correspond to the asymmetric stretching of CH_2 and CH_3 groups, which can be associated with lipid chains. This observation is not specific to the type or valence of the cation. In the presence of bacteria, it appears most likely that cations have an effect on bacterial membranes. Indeed, it has been shown that Al(III) impacts lipid-A membranes in two different ways. It can cross-link mono- or diphosphorylated lipid-A molecules and therefore stabilise their lamellar arrangement. It also affects lipid-A packing and membrane fluidity[180]. Ca(II) cations have been shown to cause the deformation of membranes containing negatively charged lipids[181]. In both cases, the effects can be counteracted by a high concentration of sodium ions. The effect was mostly visible in the biofilms formed by the *E. coli* W3110 strain, which produces only curli amyloid fibres. Whether this is due to the matrix fibres or to the lack of a larger sample is yet to be answered. While a very similar effect was indeed observed for the biofilms grown on kaolin[86], neither the bacterial strain nor the matrix composition were mentioned. The ion concentrations within the biofilms in those experiments could also have been significantly higher. Several concentrations of Fe(III) were adsorbed on the biofilm, with the uptake ranging from 1 mg(Fe)/g(biofilm) to 16 mg/g depending on the initial concentration in solution. The amounts used for the FTIR experiments were not specified. In this work, 1.22 mg of Fe(III) were added per g of biofilm, which is at the lower end of the range used in the aforementioned experiments.

Investigating purified curli fibres in the presence of metal salt solutions also allowed for a secondary structure components analysis. Surprisingly, neither the spectra over the entire range of wavenumbers nor the secondary structure analysis in the range from 1700 to 1600 cm^{-1} showed any effect of the metal cations on functional groups or the secondary structure of the curli fibres. This contrasts with expectations based on the literature on amyloid fibres. The metal cations Fe(III), Zn(II) and Cu(II) were shown to have a significant impact on the morphology and the IR spectra of Aβ plaques. However, such changes were obtained after co-incubation with a combination of those cations rather than the cations taken separately[87]. Glucagon is a peptidic hormone inducing gluconeogenesis and glycogenolysis, which exhibits at least three conformations *in vitro*: α-helical crystals, random-coil monomer, and β-sheet. Misfolded glucagon peptides generate amyloidogenic fibrils with a higher cytotoxicity than Aβ peptides. FTIR was used to show that Cu(II) promotes the conversion of glucagon peptides into amyloid fibrils while Fe(III) has the opposite effect. This transition in morphology corresponds to a change in secondary structure visible in the IR spectrum[182]. Nevertheless, the 48-hour incubation period makes the comparison with our own results difficult. Kinetic studies on the *in vitro* fibrillation of curli fibres from CsgA monomers monitored using the amyloid-binding fluorescent dye thioflavin T showed that fibrillation takes approximately six hours to reach a plateau[183]. If fibrillation occurs under such time scales, secondary structure transitions upon exposure to metal cations could be too slow to be visible in the presented experiments. Unlike for rheology, where the biofilms were incubated for 45 min, the fibre suspensions were measured directly after mixing with the metal salt solutions. In addition, Cu(II) and Fe(III) impact the formation of glucagon growing fibrils; Fe(III) does not reverse already existing fibrils into non-fibril aggregates. The purified CsgA already form amyloid fibrils, as confirmed with electron microscopy and AFM by Dr. Siri. Therefore, they may already be too stable for a change in secondary structure to occur. It is also worth mentioning that biofilms were buffered around pH=7 (see Table 6, section 5.1.3) while the fibres suspensions are not. The pH of the metal salt solutions at 400 µM are 3.0 ($FeCl_3$), 4.3 ($AlCl_3$), 5.9 ($ZnCl_2$) and 6.54 ($CaCl_2$). Therefore, aspartate and glutamate

residues will be protonated (i.e. not charged) in presence of Fe(III), partially protonated in presence of Al(III), potentially preventing them from interacting with trivalent cations the way they would in a buffered biofilm. Histidine residues will be biprotonated at acidic pH and therefore unlikely to interact with metal cations[184]. However, this situation is similar to the biofilm.

Finally, the same strategy was also applied to purified pEtN-cellulose fibres. In all salt solutions, two peaks at 1230 and 1070 cm^{-1} were shifted and their shapes changed. Most likely these peaks represent the asymmetric and symmetric stretches of the P=O double bond in the phosphodiester linkage of the pEtN-modification. Phosphodiesters were listed as one of the major functional groups for the biosorption of metal ions by Volesky et al.[185]. Moreover, phosphorylation of cellulose was shown to increase biosorption of both bivalent and trivalent ions[162]. Interactions between Fe(III) cations and phosphates of the EPS, including their P=O double bond, were observed for *B. subtilis* using ATR-FTIR[7]. Finally, Božič et al. have described similar changes in two peaks of the IR spectrum (1210 and 930 cm^{-1}) of phosphorylated cellulose fibres upon exposure to $MgCl_2$. They have shown the appearance of shoulders for the peaks corresponding to P=O and P-OH[143]. Here, this is also observed for the peaks at 1230 and 1070 cm^{-1} (Figure 21). The phosphodiester linkage of the pEtN-modification therefore appears as a good candidate for the interaction with the four metal cations tested, irrespective of their valence.

To come back to the three alternative hypotheses formulated at the beginning of this chapter: 1) trivalent cations are unlikely to specifically act as cross-linkers between both matrix fibres since no spectrum showed any specificity to valence. 2) ion condensation is likely to take place along pEtN-cellulose fibres, specifically involving the pEtN-modification. 3) bacteria membranes could possibly be affected by the cations, specifically in the absence of pEtN-cellulose, but this is unlikely to play a determining role and would not be valence-specific.

8. General discussion and outlook

8.1. Extrinsic factors

Various metal cations are known to be toxic to planktonic bacteria[145,186]. Metal cation sequestration in biofilms is therefore thought to have evolved as a defence mechanism against metal ion toxicity. Sequestration can also lead to a mechanical reinforcement of biofilms[56,57], thereby providing an additional evolutionary benefit. Which metal ions cause this reinforcement varies with bacterial species and matrix composition, just as the magnitude of the reinforcement. The goal of this work was to close an important gap in knowledge for the otherwise widely investigated bacterium *Escherichia coli*. *E. coli* produces a biofilm matrix mainly composed of pEtN-cellulose and curli amyloid fibres and the influence of metal cations on biofilm viscoelasticity was unexplored when starting this project.

In the first part of this work, bulk shear rheology was used to examine the possibility of tuning *E. coli* biofilm viscoelastic properties with metal cations. To account for the influence of matrix composition, mutant strains lacking either curli or pEtN-cellulose were used. The biofilms were incubated with cation concentrations significantly higher than those encountered in a natural environment in order to maximise possible effects. The final cation concentrations in the biofilms were 20 mM in our experiments. On the other hand, concentrations in Fe(III) cations of maximally 2 mM or 0.4 mM were measured in effluents from the textile industry[187] or the pharmaceutical industry[188], respectively. A similar approach of using high cation concentrations was already applied by Kretschmer et al. for *B. subtilis* biofilms[57]. While the cation concentrations used would not occur naturally in the environment, they could still be used in a laboratory setting to engineer biofilm properties. Considering increasing interest in biofilms as materials *per se*, methods to tune their viscoelastic properties without the need for genetic engineering are in high demand.

The bulk rheology experiments revealed that the biofilm slightly stiffened in the presence of trivalent cations, i.e. the storage and loss moduli approximately doubled. This stiffening only occurred for the bacterial strain producing both pEtN-cellulose and curli amyloid fibres. For bivalent

cations as well as for mutant strains producing only one type of fibre, a decrease in stiffness was observed. Compared to similar bulk rheology experiments conducted with *B. subtilis*[57] or *P. aeruginosa*[56] biofilms, where shear moduli increased by several orders of magnitude, much more modest changes in the moduli were observed. One possible explanation for the relatively small effect of metal cations could be the destruction of the biofilm matrix architecture during sample preparation for rheology experiments. While biofilms produced by different species also underwent similar destructive protocols, it is known that matrix composition affects biofilm stiffness[38]. As biofilm matrix composition varies between species, the partial destruction of the matrix could affect biofilms to different extents.

8.2. Intrinsic factors

In the next step, a series of experiments were designed to investigate the relationship between matrix architecture, composition and biofilm properties. Specifically, the viscoelastic properties of *E. coli* biofilms were probed with two different methods, namely bulk shear rheology and microindentation. Rheology, as previously stated, is destructive. It provides the shear modulus, i.e. a measure of the resistance of the biofilm to shear deformation. In contrast, microindentation preserves the architecture of the biofilm. It provides the Young's modulus, i.e. a measure of the biofilm stiffness in compression. Measurements were performed for biofilm samples formed by strains that produce any type of matrix composition, i.e. curli amyloid fibres and/or cellulose (with and without pEtN-modification) as well as no matrix. Microindentation experiments showed a higher stiffness for all strains producing curli fibres versus strains that did not. At the same time, no such difference was observed in rheology experiments. This highlights the importance of the native architecture for biofilm mechanical properties and suggests that biofilm homogenization at least partially destroys this architecture.

The rheology experiments, performed in the presence of metal cations, thus need to be re-evaluated in light of this new information. A native biofilm and a homogenized biofilm can be considered as

significantly different materials. In other words, the conclusions drawn from the rheology experiments after homogenization do not necessarily apply to biofilms with an intact matrix architecture. The magnitude of cation-induced changes in shear stiffness may be different for native biofilms; however, it may be assumed that the general trends observed for different matrix compositions remain the same. Indeed, during the rheology experiments, biofilms respond to metal cations as composite materials. While trivalent cations trigger a decrease in stiffness in strains producing either curli or pEtN-cellulose, they reinforce biofilms grown from bacteria that simultaneously produce both fibres. This suggests that the interactions between fibres that lead to composite material behaviour observed at the phenotypic level[46,53] persist to a certain extent after destruction of the matrix architecture.

Microrheology on native biofilms would be an elegant way of complementing these results as the native biofilm architecture can be preserved. Intact biofilms could be incubated with the solutions of interest by covering them in liquid and then removing the solution. This incubation method was already used by Kretschmer et al.[61]. Magnetic tweezers have already been used to map the viscoelasticity of *E. coli* MG1655 biofilms[66]. This strain does not produce (pEtN-)cellulose and the resulting biofilms may be less stiff than strains producing both curli and pEtN-cellulose. Using active microrheology for stiffer biofilms remains to be demonstrated. If possible, this method can also provide local information. Since the surface of the native biofilm is heterogenous, e.g. displaying wrinkles, localised effects of metal cations could possibly be highlighted.

Highly localised mechanical information could also be obtained with AFM nanoindentation. Biofilms formed by the *E. coli* strain AR3110 (producing both curli and pEtN-cellulose) were already mapped with AFM[74]. The main obstacle would be to standardise an indentation protocol suitable for the different matrix compositions with their different textures and adhesion properties. If this can be achieved, maps of biofilm stiffness in shear and in compression could be compared. A systematic comparison of both shear and Young's moduli at different locations in the biofilm is worth

investigating in itself, i.e. even in the absence of metal cations. Yet, this would be beyond the scope of this work.

8.3. At the molecular level

In the last chapter of this work, the molecular interactions between metal cations and matrix components were investigated by means of ATR-FTIR. At first, FTIR spectra were acquired for the three main bacterial strains used in this work. The strains, producing curli, pEtN-cellulose fibres or both, were mixed with one of the metal cation solutions ($AlCl_3$, $FeCl_3$, $ZnCl_2$ or $CaCl_2$), control solutions (NaCl, HCl) or water. The resulting spectra show only minor differences depending on matrix composition and metal cation added. Most likely, the biofilm spectra originate from the bacteria rather than from the biofilm matrix. This is consistent with the fact that both fibres together account for less than 1% of the biofilm dry mass[17,150]. While recent literature suggests the possibility of bacterial strain typing using FTIR[78], no protocol was followed that was specifically designed for this purpose, which relies on liquid cultures rather than bacteria embedded in their biofilms. Moreover, this field is quite recent and protocols for bacteria strain typing are still being developed. Measuring the spectra of planktonic bacteria for the different strains used within this work would be an interesting follow-up experiment. Comparing spectra from planktonic bacteria with biofilms could confirm whether the obtained spectra indeed mostly originate from the bacteria.

The most prominent change was detected for the ratio between two peaks that most likely correspond to lipid chains. This change discriminated between bivalent and trivalent cations on the one hand, and HCl and ultrapure water on the other hand. It was only observed for the *E. coli* W3110 strain, i.e., the strain producing curli amyloid fibres and no pEtN-cellulose. This change is so small that it cannot be termed significant, considering the small number of replicates (n=3 per bacterial strain). If significant, it could originate from an effect of cations on bacterial membranes, which has been described in the literature[180,181]. Irrespective of its origin, this effect cannot explain the rheology results, which discriminate between bivalent and trivalent cations, specifically in the strain producing both fibres. Further experiments in the absence of biofilm matrix would be needed to

clarify a possible interaction of metal cations with bacterial membranes in the biofilm. If an interaction between metal cations and membranes is confirmed, additional experiments could be performed to assess the interplay between metal cations, membranes and purified and artificially added pEtN-cellulose.

As the bacteria hid any possible effect of the cations on the matrix fibres, FTIR experiments were repeated with purified fibres. Fibres were purified from the two strains producing only one type of fibre (AP329 and W3110). For both matrix components, the spectra were compared in the wavenumber range from 4000 to 600 cm^{-1}. For curli amyloid fibres, an additional secondary structure component analysis was performed in the range from 1700 to 1600 cm^{-1}. Neither the overall spectra nor the secondary structure analysis yielded any significant differences between the different fibre samples. The earlier proposal of an interaction between trivalent cations and histidine, glutamate and aspartate residues can neither be infirmed nor confirmed based on the current results. Characteristic peaks[189] corresponding to their side chains were absent from the spectra of the curli fibres. Another method to investigate complexation of metal cations by curli fibres could be nuclear magnetic resonance (NMR), which was used to study metal complexation by Aβ peptides[137,139]. In addition, Raman spectroscopy was also used to investigate Zn(II) and Cu(II) complexation by histidine residues in histidine-rich domains[25].

The analysis of pEtN-cellulose was more informative. In the presence of both bivalent and trivalent cations, a change in the peaks corresponding to the phosphate group of the pEtN-modification was observed. This is strongly supported from the literature[7,143,162,185]. This is interesting for two reasons. (1) The interaction between cations and the pEtN-modification could possibly prevent the cations from acting on the membrane, as suggested in the experiments with biofilms. This in turn raises the question why the cation-membrane interaction was not observed in presence of curli. (2) The interaction between the phosphate group of pEtN-cellulose and the metal cations suggests that charge condensation is indeed possible along the pEtN-cellulose fibres for both bivalent and trivalent cations. Nevertheless, such effects occur only with pEtN-cellulose and do not discriminate between

valences, while the stiffening observed in the rheology experiments occurs specifically with trivalent cations and in presence of both fibres produced by the same bacteria. Therefore, charge condensation along the pEtN-cellulose fibres alone cannot explain the trends observed with the rheology experiments. It cannot explain either the texture of the cation-biofilm mixtures, which is also specific to trivalent cations.

8.4. Conclusion

To summarise and conclude, a key result of this work is the observation that trivalent cations specifically reinforce *E. coli* biofilms where pEtN-cellulose and curli amyloid fibres are co-produced by the same bacteria cell. This reinforcement is probably underestimated after partial destruction of the biofilm matrix architecture. No such reinforcement is observed for biofilms that contain only one type of matrix fibre as well as for bivalent cations. Although metal cations seemed to affect the FTIR spectrum of pEtN-cellulose, suggesting an interaction at the molecular scale, these observations alone cannot account for the reinforcement observed with bulk rheology. Possible mechanisms such as charge condensation or osmotic effects remain to be investigated. More generally, this works confirms the composite material nature of *E. coli* biofilms and highlights the importance of the native biofilm architecture for determining the biofilm material properties. This work further emphasizes the possibility of tuning biofilm viscoelasticity without the need for genetic engineering. It demonstrates that the underlying molecular mechanisms as well as the magnitude of achievable changes differ between bacterial species and within strains of the same species. Thus, every targeted organism and the interaction of its matrix components with metal cations needs to be investigated case by case.

9. References

(1) Ramage, G.; Rajendran, R.; Gutierrez-Correa, M.; Jones, B.; Williams, C. Aspergillus Biofilms: Clinical and Industrial Significance. *FEMS Microbiol. Lett.* **2011**, *324* (2), 89–97. https://doi.org/10.1111/j.1574-6968.2011.02381.x.

(2) Pierce, C.; Vila, T.; Romo, J.; Montelongo-Jauregui, D.; Wall, G.; Ramasubramanian, A.; Lopez-Ribot, J. The Candida Albicans Biofilm Matrix: Composition, Structure and Function. *J. Fungi* **2017**, *3* (1), 14. https://doi.org/10.3390/jof3010014.

(3) Flemming, H.-C.; Wuertz, S. Bacteria and Archaea on Earth and Their Abundance in Biofilms. *Nat. Rev. Microbiol.* **2019**, *17* (4), 247–260. https://doi.org/10.1038/s41579-019-0158-9.

(4) Reisner, A.; Maierl, M.; Jörger, M.; Krause, R.; Berger, D.; Haid, A.; Tesic, D.; Zechner, E. L. Type 1 Fimbriae Contribute to Catheter-Associated Urinary Tract Infections Caused by Escherichia Coli. *J. Bacteriol.* **2014**, *196* (5), 931–939. https://doi.org/10.1128/JB.00985-13.

(5) Shemesh, M.; Ostrov, I. Role of Bacillus Species in Biofilm Persistence and Emerging Antibiofilm Strategies in the Dairy Industry. *J. Sci. Food Agric.* **2020**, *100* (6), 2327–2336. https://doi.org/10.1002/jsfa.10285.

(6) Procópio, L. Microbially Induced Corrosion Impacts on the Oil Industry. *Arch. Microbiol.* **2022**, *204* (2), 138. https://doi.org/10.1007/s00203-022-02755-7.

(7) Zhang, C.; Huang, J.; Zhang, J.; Liu, S.; Cui, M.; An, B.; Wang, X.; Pu, J.; Zhao, T.; Fan, C.; Lu, T. K.; Zhong, C. Engineered Bacillus Subtilis Biofilms as Living Glues. *Mater. Today* **2019**, *28* (September), 40–48. https://doi.org/10.1016/j.mattod.2018.12.039.

(8) Duraj-Thatte, A. M.; Manjula-Basavanna, A.; Courchesne, N. M. D.; Cannici, G. I.; Sánchez-Ferrer, A.; Frank, B. P.; van't Hag, L.; Cotts, S. K.; Fairbrother, D. H.; Mezzenga, R.; Joshi, N. S. Water-Processable, Biodegradable and Coatable Aquaplastic from Engineered Biofilms. *Nat. Chem. Biol.* **2021**, *17* (6), 732–738. https://doi.org/10.1038/s41589-021-00773-y.

(9) Balasubramanian, S.; Aubin-Tam, M.-E.; Meyer, A. S. 3D Printing for the Fabrication of Biofilm-Based Functional Living Materials. *ACS Synth. Biol.* **2019**, *8* (7), 1564–1567. https://doi.org/10.1021/acssynbio.9b00192.

(10) Limoli, D. H.; Jones, C. J.; Wozniak, D. J. Bacterial Extracellular Polysaccharides in Biofilm Formation and Function. *Microbiol. Spectr.* **2015**, *3* (3), 1–30. https://doi.org/10.1128/microbiolspec.mb-0011-2014.

(11) Fong, J. N. C.; Yildiz, F. H. Biofilm Matrix Proteins. *Microbiol. Spectr.* **2015**, *3* (2). https://doi.org/10.1128/microbiolspec.MB-0004-2014.

(12) Flemming, H.-C.; Wingender, J.; Szewzyk, U.; Steinberg, P.; Rice, S. A.; Kjelleberg, S. Biofilms: An Emergent Form of Bacterial Life. *Nat. Rev. Microbiol.* **2016**, *14* (9), 563–575. https://doi.org/10.1038/nrmicro.2016.94.

(13) Mann, E. E.; Wozniak, D. J. Pseudomonas Biofilm Matrix Composition and Niche Biology. *FEMS Microbiol. Rev.* **2012**, *36* (4), 893–916. https://doi.org/10.1111/j.1574-6976.2011.00322.x.

(14) Erskine, E.; MacPhee, C. E.; Stanley-Wall, N. R. Functional Amyloid and Other Protein Fibers in the Biofilm Matrix. *J. Mol. Biol.* **2018**, *430* (20), 3642–3656. https://doi.org/10.1016/j.jmb.2018.07.026.

(15) Barnhart, M. M.; Chapman, M. R. Curli Biogenesis and Function. *Annu. Rev. Microbiol.* **2006**, *60* (1), 131–147. https://doi.org/10.1146/annurev.micro.60.080805.142106.

(16) Thongsomboon, W.; Serra, D. O.; Possling, A.; Hadjineophytou, C.; Hengge, R.; Cegelski, L. Phosphoethanolamine Cellulose: A Naturally Produced Chemically Modified Cellulose. *Science (80-.).* **2018**, *359* (6373), 334–338. https://doi.org/10.1126/science.aao4096.

(17) Jeffries, J.; Thongsomboon, W.; Visser, J. A.; Enriquez, K.; Yager, D.; Cegelski, L. Variation in the Ratio of Curli and Phosphoethanolamine Cellulose Associated with Biofilm Architecture and Properties. *Biopolymers* **2021**, *112* (1), 1–11. https://doi.org/10.1002/bip.23395.

(18) Ziege, R.; Tsirigoni, A.-M.; Large, B.; Serra, D. O.; Blank, K. G.; Hengge, R.; Fratzl, P.; Bidan, C. M. Adaptation of Escherichia Coli Biofilm Growth, Morphology, and Mechanical Properties to Substrate Water Content. *ACS Biomater. Sci. Eng.* **2021**, *7* (11), 5315–5325. https://doi.org/10.1021/acsbiomaterials.1c00927.

(19) Rühs, P. A.; Böni, L.; Fuller, G. G.; Inglis, R. F.; Fischer, P. In-Situ Quantification of the Interfacial Rheological Response of Bacterial Biofilms to Environmental Stimuli. *PLoS One* **2013**, *8* (11), e78524. https://doi.org/10.1371/journal.pone.0078524.

(20) Degtyar, E.; Harrington, M. J.; Politi, Y.; Fratzl, P. The Mechanical Role of Metal Ions in Biogenic Protein-Based Materials. *Angew. Chemie Int. Ed.* **2014**, *53* (45), 12026–12044. https://doi.org/10.1002/anie.201404272.

(21) Ukmar-Godec, T. Mineralization of Goethite in Limpet Radular Teeth. In *Iron Oxides*; Faivre, D., Ed.; Wiley, 2016; pp 207–224. https://doi.org/10.1002/9783527691395.ch9.

(22) Chan, C. S.; Fakra, S. C.; Edwards, D. C.; Emerson, D.; Banfield, J. F. Iron Oxyhydroxide Mineralization on Microbial Extracellular Polysaccharides. *Geochim. Cosmochim. Acta* **2009**, *73* (13), 3807–3818. https://doi.org/10.1016/j.gca.2009.02.036.

(23) Fratzl, P.; Gupta, H. S.; Paschalis, E. P.; Roschger, P. Structure and Mechanical Quality of the Collagen–Mineral Nano-Composite in Bone. *J. Mater. Chem.* **2004**, *14* (14), 2115–2123. https://doi.org/10.1039/B402005G.

(24) Baumgartner, J.; Faivre, D. Magnetite Biomineralization in Bacteria. In *Progress in molecular and subcellular biology*; 2011; Vol. 52, pp 3–27. https://doi.org/10.1007/978-3-642-21230-7_1.

(25) Jehle, F.; Fratzl, P.; Harrington, M. J. Metal-Tunable Self-Assembly of Hierarchical Structure in Mussel-Inspired Peptide Films. *ACS Nano* **2018**, *12* (3), 2160–2168. https://doi.org/10.1021/acsnano.7b07905.

(26) Khare, E.; Holten-Andersen, N.; Buehler, M. J. Transition-Metal Coordinate Bonds for Bioinspired Macromolecules with Tunable Mechanical Properties. *Nat. Rev. Mater.* **2021**, *6* (5), 421–436. https://doi.org/10.1038/s41578-020-00270-z.

(27) Mosharaf, M. K.; Tanvir, M. Z. H.; Haque, M. M.; Haque, M. A.; Khan, M. A. A.; Molla, A. H.; Alam, M. Z.; Islam, M. S.; Talukder, M. R. Metal-Adapted Bacteria Isolated from Wastewaters Produce Biofilms by Expressing Proteinaceous Curli Fimbriae and Cellulose Nanofibers. *Front. Microbiol.* **2018**, *9* (JUN), 1–17. https://doi.org/10.3389/fmicb.2018.01334.

(28) Tallawi, M.; Opitz, M.; Lieleg, O. Modulation of the Mechanical Properties of Bacterial Biofilms in Response to Environmental Challenges. *Biomater. Sci.* **2017**, *5* (5), 887–900. https://doi.org/10.1039/C6BM00832A.

(29) Klotz, M.; Kretschmer, M.; Goetz, A.; Ezendam, S.; Lieleg, O.; Opitz, M. Importance of the Biofilm Matrix for the Erosion Stability of Bacillus Subtilis NCIB 3610 Biofilms. *RSC Adv.* **2019**, *9* (20), 11521–11529. https://doi.org/10.1039/C9RA01955C.

(30) DePas, W. H.; Hufnagel, D. A.; Lee, J. S.; Blanco, L. P.; Bernstein, H. C.; Fisher, S. T.; James, G. A.; Stewart, P. S.; Chapman, M. R. Iron Induces Bimodal Population Development by Escherichia Coli. *Proc. Natl. Acad. Sci.* **2013**, *110* (7), 2629–2634. https://doi.org/10.1073/pnas.1218703110.

(31) Noffke, N.; Awramik, S. M. Stromatolites and MISS—Differences between Relatives. *GSA Today* **2013**, *23* (9), 4–9. https://doi.org/10.1130/GSATG187A.1.

(32) Schnurr, P. J.; Allen, D. G. Factors Affecting Algae Biofilm Growth and Lipid Production: A Review. *Renew. Sustain. Energy Rev.* **2015**, *52*, 418–429. https://doi.org/10.1016/j.rser.2015.07.090.

(33) Magalhães, R. P.; Vieira, T. F.; Fernandes, H. S.; Melo, A.; Simões, M.; Sousa, S. F. The Biofilms Structural Database. *Trends Biotechnol.* **2020**, *38* (9), 937–940. https://doi.org/10.1016/j.tibtech.2020.04.002.

(34) Khatoon, Z.; McTiernan, C. D.; Suuronen, E. J.; Mah, T.-F.; Alarcon, E. I. Bacterial Biofilm Formation on Implantable Devices and Approaches to Its Treatment and Prevention. *Heliyon* **2018**, *4* (12), e01067. https://doi.org/10.1016/j.heliyon.2018.e01067.

(35) Schulze, A.; Mitterer, F.; Pombo, J. P.; Schild, S. Biofilms by Bacterial Human Pathogens: Clinical Relevance - Development, Composition and Regulation - Therapeutical Strategies. *Microb. Cell* **2021**, *8* (2), 28–56. https://doi.org/10.15698/mic2021.02.741.

(36) Wagner, E. M.; Fischel, K.; Rammer, N.; Beer, C.; Palmetzhofer, A. L.; Conrady, B.; Roch, F.-F.; Hanson, B. T.; Wagner, M.; Rychli, K. Bacteria of Eleven Different Species Isolated from Biofilms in a Meat Processing Environment Have Diverse Biofilm Forming Abilities. *Int. J. Food Microbiol.* **2021**, *349* (April), 109232. https://doi.org/10.1016/j.ijfoodmicro.2021.109232.

(37) Cairns, L. S.; Hobley, L.; Stanley-Wall, N. R. Biofilm Formation by Bacillus Subtilis : New Insights into Regulatory Strategies and Assembly Mechanisms. *Mol. Microbiol.* **2014**, *93* (4), 587–598. https://doi.org/10.1111/mmi.12697.

(38) Kesel, S.; Grumbein, S.; Gümperlein, I.; Tallawi, M.; Marel, A.-K.; Lieleg, O.; Opitz, M. Direct Comparison of Physical Properties of Bacillus Subtilis NCIB 3610 and B-1 Biofilms. *Appl. Environ. Microbiol.* **2016**, *82* (8), 2424–2432. https://doi.org/10.1128/AEM.03957-15.

(39) Kovach, K.; Davis-Fields, M.; Irie, Y.; Jain, K.; Doorwar, S.; Vuong, K.; Dhamani, N.; Mohanty, K.; Touhami, A.; Gordon, V. D. Evolutionary Adaptations of Biofilms Infecting Cystic Fibrosis Lungs Promote Mechanical Toughness by Adjusting Polysaccharide Production. *npj Biofilms Microbiomes* **2017**, *3* (1), 1. https://doi.org/10.1038/s41522-016-0007-9.

(40) Jennings, L. K.; Storek, K. M.; Ledvina, H. E.; Coulon, C.; Marmont, L. S.; Sadovskaya, I.; Secor, P. R.; Tseng, B. S.; Scian, M.; Filloux, A.; Wozniak, D. J.; Howell, P. L.; Parsek, M. R. Pel Is a Cationic Exopolysaccharide That Cross-Links Extracellular DNA in the Pseudomonas Aeruginosa Biofilm Matrix. *Proc. Natl. Acad. Sci.* **2015**, *112* (36), 11353–11358. https://doi.org/10.1073/pnas.1503058112.

(41) Tenaillon, O.; Skurnik, D.; Picard, B.; Denamur, E. The Population Genetics of Commensal Escherichia Coli. *Nat. Rev. Microbiol.* **2010**, *8* (3), 207–217. https://doi.org/10.1038/nrmicro2298.

(42) Bachmann, B. J. Pedigrees of Some Mutant Strains of Escherichia Coli K-12. *Bacteriol. Rev.* **1972**, *36* (4), 525–557. https://doi.org/10.1128/MMBR.36.4.525-557.1972.

(43) Blattner, F. R.; Plunkett, G.; Bloch, C. A.; Perna, N. T.; Burland, V.; Riley, M.; Collado-Vides, J.; Glasner, J. D.; Rode, C. K.; Mayhew, G. F.; Gregor, J.; Davis, N. W.; Kirkpatrick, H. A.; Goeden, M. A.; Rose, D. J.; Mau, B.; Shao, Y. The Complete Genome Sequence of Escherichia Coli K-12. *Science (80-.).* **1997**, *277* (5331), 1453–1462. https://doi.org/10.1126/science.277.5331.1453.

(44) Hayashi, K.; Morooka, N.; Yamamoto, Y.; Fujita, K.; Isono, K.; Choi, S.; Ohtsubo, E.; Baba, T.; Wanner, B. L.; Mori, H.; Horiuchi, T. Highly Accurate Genome Sequences of Escherichia Coli K-12 Strains MG1655 and W3110. *Mol. Syst. Biol.* **2006**, *2* (1). https://doi.org/10.1038/msb4100049.

(45) Hengge, R. Principles of C-Di-GMP Signalling in Bacteria. *Nat. Rev. Microbiol.* **2009**, *7* (4), 263–273. https://doi.org/10.1038/nrmicro2109.

(46) Serra, D. O.; Richter, A. M.; Hengge, R. Cellulose as an Architectural Element in Spatially Structured Escherichia Coli Biofilms. *J. Bacteriol.* **2013**, *195* (24), 5540–5554. https://doi.org/10.1128/JB.00946-13.

(47) Evans, M. L.; Chapman, M. R. Curli Biogenesis: Order out of Disorder. *Biochim. Biophys. Acta - Mol. Cell Res.* **2014**, *1843* (8), 1551–1558. https://doi.org/10.1016/j.bbamcr.2013.09.010.

(48) Anderson, A. C.; Burnett, A. J. N.; Hiscock, L.; Maly, K. E.; Weadge, J. T. The Escherichia Coli Cellulose Synthase Subunit G (BcsG) Is a Zn 2+ -Dependent Phosphoethanolamine Transferase. *J. Biol. Chem.* **2020**, *295* (18), 6225–6235. https://doi.org/10.1074/jbc.RA119.011668.

(49) Ogasawara, H.; Yamamoto, K.; Ishihama, A. Regulatory Role of MlrA in Transcription Activation of CsgD, the Master Regulator of Biofilm Formation in Escherichia Coli. *FEMS Microbiol. Lett.* **2010**, *312* (2), 160–168. https://doi.org/10.1111/j.1574-6968.2010.02112.x.

(50) Mika, F.; Hengge, R. Small RNAs in the Control of RpoS, CsgD, and Biofilm Architecture of Escherichia Coli. *RNA Biol.* **2014**, *11* (5), 494–507. https://doi.org/10.4161/rna.28867.

(51) Bougdour, A.; Lelong, C.; Geiselmann, J. Crl, a Low Temperature-Induced Protein in Escherichia Coli That Binds Directly to the Stationary Phase σ Subunit of RNA Polymerase. *J. Biol. Chem.* **2004**, *279* (19), 19540–19550. https://doi.org/10.1074/jbc.M314145200.

(52) Dunbar, M.; DeBenedictis, E.; Keten, S. Dimerization Energetics of Curli Fiber Subunits CsgA and CsgB. *npj Comput. Mater.* **2019**, *5* (1), 27. https://doi.org/10.1038/s41524-019-0164-5.

(53) Serra, D. O.; Klauck, G.; Hengge, R. Vertical Stratification of Matrix Production Is Essential for Physical Integrity and Architecture of Macrocolony Biofilms of E Scherichia Coli. *Environ. Microbiol.* **2015**, *17* (12), 5073–5088. https://doi.org/10.1111/1462-2920.12991.

(54) Klauck, G.; Serra, D. O.; Possling, A.; Hengge, R. Spatial Organization of Different Sigma Factor Activities and C-Di-GMP Signalling within the Three-Dimensional Landscape of a Bacterial Biofilm. *Open Biol.* **2018**, *8* (8). https://doi.org/10.1098/rsob.180066.

(55) Serra, D. O.; Richter, A. M.; Klauck, G.; Mika, F.; Hengge, R. Microanatomy at Cellular Resolution and Spatial Order of Physiological Differentiation in a Bacterial Biofilm. *MBio* **2013**, *4* (2). https://doi.org/10.1128/mBio.00103-13.

(56) Lieleg, O.; Caldara, M.; Baumgärtel, R.; Ribbeck, K. Mechanical Robustness of Pseudomonas Aeruginosa Biofilms. *Soft Matter* **2011**, *7* (7), 3307. https://doi.org/10.1039/c0sm01467b.

(57) Kretschmer, M.; Lieleg, O. Chelate Chemistry Governs Ion-Specific Stiffening of: Bacillus Subtilis B-1 and Azotobacter Vinelandii Biofilms. *Biomater. Sci.* **2020**, *8* (7), 1923–1933. https://doi.org/10.1039/c9bm01763a.

(58) Shaw, T.; Winston, M.; Rupp, C. J.; Klapper, I.; Stoodley, P. Commonality of Elastic Relaxation Times in Biofilms. *Phys. Rev. Lett.* **2004**, *93* (9), 098102. https://doi.org/10.1103/PhysRevLett.93.098102.

(59) Yan, J.; Moreau, A.; Khodaparast, S.; Perazzo, A.; Feng, J.; Fei, C.; Mao, S.; Mukherjee, S.; Košmrlj, A.; Wingreen, N. S.; Bassler, B. L.; Stone, H. A. Bacterial Biofilm Material Properties Enable Removal and Transfer by Capillary Peeling. *Adv. Mater.* **2018**, *30* (46), 1–10. https://doi.org/10.1002/adma.201804153.

(60) Pavlovsky, L.; Younger, J. G.; Solomon, M. J. In Siturheology of Staphylococcus Epidermidis Bacterial Biofilms. *Soft Matter* **2013**, *9* (1), 122–131. https://doi.org/10.1039/C2SM27005F.

(61) Kretschmer, M.; Schüßler, C. A.; Lieleg, O. Biofilm Adhesion to Surfaces Is Modulated by Biofilm Wettability and Stiffness. *Adv. Mater. Interfaces* **2021**, *8* (5), 2001658. https://doi.org/10.1002/admi.202001658.

(62) Pandit, S.; Fazilati, M.; Gaska, K.; Derouiche, A.; Nypelö, T.; Mijakovic, I.; Kádár, R. The Exo-Polysaccharide Component of Extracellular Matrix Is Essential for the Viscoelastic Properties of Bacillus Subtilis Biofilms. *Int. J. Mol. Sci.* **2020**, *21* (18), 6755. https://doi.org/10.3390/ijms21186755.

(63) Mao, Y.; Nielsen, P.; Ali, J. Passive and Active Microrheology for Biomedical Systems. *Front. Bioeng. Biotechnol.* **2022**, *10* (July). https://doi.org/10.3389/fbioe.2022.916354.

(64) Rogers, S. S.; van der Walle, C.; Waigh, T. A. Microrheology of Bacterial Biofilms In Vitro: Staphylococcus Aureus and Pseudomonas Aeruginosa. *Langmuir* **2008**, *24* (23), 13549–13555. https://doi.org/10.1021/la802442d.

(65) Cheong, F. C.; Duarte, S.; Lee, S.-H.; Grier, D. G. Holographic Microrheology of Polysaccharides from Streptococcus Mutans Biofilms. *Rheol. Acta* **2009**, *48* (1), 109–115. https://doi.org/10.1007/s00397-008-0320-1.

(66) Galy, O.; Latour-Lambert, P.; Zrelli, K.; Ghigo, J.-M.; Beloin, C.; Henry, N. Mapping of Bacterial Biofilm Local Mechanics by Magnetic Microparticle Actuation. *Biophys. J.* **2012**, *103* (6), 1400–1408. https://doi.org/10.1016/j.bpj.2012.07.001.

(67) Stojković, B.; Sretenovic, S.; Dogsa, I.; Poberaj, I.; Stopar, D. Viscoelastic Properties of Levan-DNA Mixtures Important in Microbial Biofilm Formation as Determined by Micro- and Macrorheology. *Biophys. J.* **2015**, *108* (3), 758–765. https://doi.org/10.1016/j.bpj.2014.10.072.

(68) Poppele, E. H.; Hozalski, R. M. Micro-Cantilever Method for Measuring the Tensile Strength of Biofilms and Microbial Flocs. *J. Microbiol. Methods* **2003**, *55* (3), 607–615. https://doi.org/10.1016/S0167-7012(03)00198-2.

(69) Cense, A. W.; Peeters, E. A. G.; Gottenbos, B.; Baaijens, F. P. T.; Nuijs, A. M.; van Dongen, M. E. H. Mechanical Properties and Failure of Streptococcus Mutans Biofilms, Studied Using a Microindentation Device. *J. Microbiol. Methods* **2006**, *67* (3), 463–472. https://doi.org/10.1016/j.mimet.2006.04.023.

(70) Chen, M. J.; Zhang, Z.; Bott, T. R. Effects of Operating Conditions on the Adhesive Strength of Pseudomonas Fluorescens Biofilms in Tubes. *Colloids Surfaces B Biointerfaces* **2005**, *43* (2), 61–71. https://doi.org/10.1016/j.colsurfb.2005.04.004.

(71) Aggarwal, S.; Poppele, E. H.; Hozalski, R. M. Development and Testing of a Novel Microcantilever Technique for Measuring the Cohesive Strength of Intact Biofilms. *Biotechnol. Bioeng.* **2010**, *105* (5), n/a-n/a. https://doi.org/10.1002/bit.22605.

(72) Vadillo-Rodriguez, V.; Beveridge, T. J.; Dutcher, J. R. Surface Viscoelasticity of Individual Gram-Negative Bacterial Cells Measured Using Atomic Force Microscopy. *J. Bacteriol.* **2008**, *190* (12), 4225–4232. https://doi.org/10.1128/JB.00132-08.

(73) López-Guerra, E. A.; Shen, H.; Solares, S. D.; Shuai, D. Acquisition of Time–Frequency Localized Mechanical Properties of Biofilms and Single Cells with High Spatial Resolution. *Nanoscale* **2019**, *11* (18), 8918–8929. https://doi.org/10.1039/C8NR10287B.

(74) Kreis, C. T.; Sullan, R. M. A. Interfacial Nanomechanical Heterogeneity of the E. Coli Biofilm Matrix. *Nanoscale* **2020**, *12* (32), 16819–16830. https://doi.org/10.1039/D0NR03646C.

(75) Miller, E.; Garcia, T.; Hultgren, S.; Oberhauser, A. F. The Mechanical Properties of E. Coli Type 1 Pili Measured by Atomic Force Microscopy Techniques. *Biophys. J.* **2006**, *91* (10), 3848–3856. https://doi.org/10.1529/biophysj.106.088989.

(76) Forero, M.; Yakovenko, O.; Sokurenko, E. V.; Thomas, W. E.; Vogel, V. Uncoiling Mechanics of Escherichia Coli Type I Fimbriae Are Optimized for Catch Bonds. *PLoS Biol.* **2006**, *4* (9), e298. https://doi.org/10.1371/journal.pbio.0040298.

(77) Berthomieu, C.; Hienerwadel, R. Fourier Transform Infrared (FTIR) Spectroscopy. *Photosynth. Res.* **2009**, *101* (2–3), 157–170. https://doi.org/10.1007/s11120-009-9439-x.

(78) Chirman, D.; Pleshko, N. Characterization of Bacterial Biofilm Infections with Fourier Transform Infrared Spectroscopy: A Review. *Appl. Spectrosc. Rev.* **2021**, *56* (8–10), 673–701. https://doi.org/10.1080/05704928.2020.1864392.

(79) Novais, Â.; Freitas, A. R.; Rodrigues, C.; Peixe, L. Fourier Transform Infrared Spectroscopy: Unlocking Fundamentals and Prospects for Bacterial Strain Typing. *Eur. J. Clin. Microbiol. Infect. Dis.* **2019**, *38* (3), 427–448. https://doi.org/10.1007/s10096-018-3431-3.

(80) Gieroba, B.; Krysa, M.; Wojtowicz, K.; Wiater, A.; Tomczyk, M. 20-IJMS_ The FT-IR _ Raman Spectrosc as Tools for Biofilm Character Created by Cariogenic Streptococci.Pdf. 1–20.

(81) Singhalage, I. D.; Seneviratne, G.; Madawala, H. M. S. P.; Manawasinghe, I. S. Characterization of Structural Properties of Fungal-Bacterial Biofilms by Fourier Transform Infrared Spectroscopy. *Ceylon J. Sci.* **2018**, *47* (1), 77. https://doi.org/10.4038/cjs.v47i1.7490.

(82) Ariafar, M. N.; Iğci, N.; Akçelik, M.; Akçelik, N. Investigation of the Effect of Different Environmental Conditions on Biofilm Structure of Salmonella Enterica Serotype Virchow via FTIR Spectroscopy. *Arch. Microbiol.* **2019**, *201* (9), 1233–1248. https://doi.org/10.1007/s00203-019-01681-5.

(83) Sano, K.; Kanematsu, H.; Kogo, T.; Hirai, N.; Tanaka, T. Corrosion and Biofilm for a Composite Coated Iron Observed by FTIR-ATR and Raman Spectroscopy. *Trans. IMF* **2016**, *94* (3), 139–145. https://doi.org/10.1080/00202967.2016.1167315.

(84) Villa, F.; Secundo, F.; Forlani, F.; Cattò, C.; Cappitelli, F. Biochemical and Molecular Changes of the Zosteric Acid-Treated Escherichia Coli Biofilm on a Mineral Surface. *Ann. Microbiol.* **2021**, *71* (1), 3. https://doi.org/10.1186/s13213-020-01617-1.

(85) Zalewska-Piątek, B.; Wilkanowicz, S.; Bruździak, P.; Piątek, R.; Kur, J. Biochemical Characteristic of Biofilm of Uropathogenic Escherichia Coli Dr + Strains. *Microbiol. Res.* **2013**, *168* (6), 367–378. https://doi.org/10.1016/j.micres.2013.01.001.

(86) Quintelas, C.; Rocha, Z.; Silva, B.; Fonseca, B.; Figueiredo, H.; Tavares, T. Removal of Cd(II), Cr(VI), Fe(III) and Ni(II) from Aqueous Solutions by an E. Coli Biofilm Supported on Kaolin. *Chem. Eng. J.* **2009**, *149* (1–3), 319–324. https://doi.org/10.1016/j.cej.2008.11.025.

(87) Ryu, J.; Girigoswami, K.; Ha, C.; Ku, S. H.; Park, C. B. Influence of Multiple Metal Ions on β-Amyloid Aggregation and Dissociation on a Solid Surface. *Biochemistry* **2008**, *47* (19), 5328–5335. https://doi.org/10.1021/bi800012e.

(88) Sundar, S. T.; Sain, M. M.; Oksman, K. Characterization of Microcrystalline Cellulose and Cellulose Long Fiber Modified by Iron Salt. *Carbohydr. Polym.* **2010**, *80* (1), 35–43. https://doi.org/10.1016/j.carbpol.2009.10.072.

(89) Sportelli, M. C.; Kranz, C.; Mizaikoff, B.; Cioffi, N. Recent Advances on the Spectroscopic Characterization of Microbial Biofilms: A Critical Review. *Anal. Chim. Acta* **2022**, *1195*, 339433. https://doi.org/10.1016/j.aca.2022.339433.

(90) Pratt, L. A.; Kolter, R. Genetic Analyses of Bacterial Biofilm Formation. *Curr. Opin. Microbiol.* **1999**, *2* (6), 598–603. https://doi.org/10.1016/S1369-5274(99)00028-4.

(91) Mahto, K. U.; Kumari, S.; Das, S. Unraveling the Complex Regulatory Networks in Biofilm Formation in Bacteria and Relevance of Biofilms in Environmental Remediation. *Crit. Rev. Biochem. Mol. Biol.* **2022**, *57* (3), 305–332. https://doi.org/10.1080/10409238.2021.2015747.

(92) Tolker-Nielsen, T. Biofilm Development. *Microbiol. Spectr.* **2015**, *3* (2), 100043. https://doi.org/10.1128/microbiolspec.MB-0001-2014.

(93) Fei, C.; Mao, S.; Yan, J.; Alert, R.; Stone, H. A.; Bassler, B. L.; Wingreen, N. S.; Košmrlj, A. Nonuniform Growth and Surface Friction Determine Bacterial Biofilm Morphology on Soft Substrates. *Proc. Natl. Acad. Sci.* **2020**, *117* (14), 7622–7632. https://doi.org/10.1073/pnas.1919607117.

(94) Yan, J.; Nadell, C. D.; Stone, H. A.; Wingreen, N. S.; Bassler, B. L. Extracellular-Matrix-Mediated Osmotic Pressure Drives Vibrio Cholerae Biofilm Expansion and Cheater Exclusion. *Nat. Commun.* **2017**, *8* (1), 327. https://doi.org/10.1038/s41467-017-00401-1.

(95) Lucia Stecchini, M.; Del Torre, M.; Donda, S.; Maltini, E.; Pacor, S. Influence of Agar Content on the Growth Parameters of Bacillus Cereus. *Int. J. Food Microbiol.* **2001**, *64* (1–2), 81–88. https://doi.org/10.1016/S0168-1605(00)00436-0.

(96) Wang, X.; Kong, Y.; Zhao, H.; Yan, X. Dependence of the Bacillus Subtilis Biofilm Expansion Rate on Phenotypes and the Morphology under Different Growing Conditions. *Dev. Growth Differ.* **2019**, *61* (7–8), 431–443. https://doi.org/10.1111/dgd.12627.

(97) Roberson, E. B.; Firestone, M. K. Relationship between Desiccation and Exopolysaccharide Production in a Soil Pseudomonas Sp. *Appl. Environ. Microbiol.* **1992**, *58* (4), 1284–1291. https://doi.org/10.1128/aem.58.4.1284-1291.1992.

(98) Wilking, J. N.; Zaburdaev, V.; De Volder, M.; Losick, R.; Brenner, M. P.; Weitz, D. A. Liquid Transport Facilitated by Channels in Bacillus Subtilis Biofilms. *Proc. Natl. Acad. Sci.* **2013**, *110* (3), 848–852. https://doi.org/10.1073/pnas.1216376110.

(99) Allen, A.; Habimana, O.; Casey, E. The Effects of Extrinsic Factors on the Structural and Mechanical Properties of Pseudomonas Fluorescens Biofilms: A Combined Study of Nutrient Concentrations and Shear Conditions. *Colloids Surfaces B Biointerfaces* **2018**, *165*, 127–134. https://doi.org/10.1016/j.colsurfb.2018.02.035.

(100) Stoodley, P.; Lewandowski, Z.; Boyle, J. D.; Lappin-Scott, H. M. The Formation of Migratory Ripples in a Mixed Species Bacterial Biofilm Growing in Turbulent Flow. *Environ. Microbiol.* **1999**, *1* (5), 447–455. https://doi.org/10.1046/j.1462-2920.1999.00055.x.

(101) Dunsmore, B. C.; Jacobsen, A.; Hall-Stoodley, L.; Bass, C. J.; Lappin-Scott, H. M.; Stoodley, P. The Influence of Fluid Shear on the Structure and Material Properties of Sulphate-Reducing Bacterial Biofilms. *J. Ind. Microbiol. Biotechnol.* **2002**, *29* (6), 347–353. https://doi.org/10.1038/sj.jim.7000302.

(102) Weaver, W. M.; Milisavljevic, V.; Miller, J. F.; Di Carlo, D. Fluid Flow Induces Biofilm Formation in Staphylococcus Epidermidis Polysaccharide Intracellular Adhesin-Positive Clinical Isolates. *Appl. Environ. Microbiol.* **2012**, *78* (16), 5890–5896. https://doi.org/10.1128/AEM.01139-12.

(103) Song, J. L.; Au, K. H.; Huynh, K. T.; Packman, A. I. Biofilm Responses to Smooth Flow Fields and Chemical Gradients in Novel Microfluidic Flow Cells. *Biotechnol. Bioeng.* **2014**, *111* (3), 597–607. https://doi.org/10.1002/bit.25107.

(104) Song, X.; Ma, Y.; Fu, J.; Zhao, A.; Guo, Z.; Malakar, P. K.; Pan, Y.; Zhao, Y. Effect of Temperature on Pathogenic and Non-Pathogenic Vibrio Parahaemolyticus Biofilm Formation. *Food Control* **2017**, *73*, 485–491. https://doi.org/10.1016/j.foodcont.2016.08.041.

(105) Stepanović, S.; Ćirković, I.; Mijač, V.; Švabić-Vlahović, M. Influence of the Incubation Temperature, Atmosphere and Dynamic Conditions on Biofilm Formation by Salmonella Spp. *Food Microbiol.* **2003**, *20* (3), 339–343. https://doi.org/10.1016/S0740-0020(02)00123-5.

(106) Kadam, S. R.; den Besten, H. M. W.; van der Veen, S.; Zwietering, M. H.; Moezelaar, R.; Abee, T. Diversity Assessment of Listeria Monocytogenes Biofilm Formation: Impact of Growth Condition, Serotype and Strain Origin. *Int. J. Food Microbiol.* **2013**, *165* (3), 259–264. https://doi.org/10.1016/j.ijfoodmicro.2013.05.025.

(107) Di Ciccio, P.; Vergara, A.; Festino, A. R.; Paludi, D.; Zanardi, E.; Ghidini, S.; Ianieri, A. Biofilm Formation by Staphylococcus Aureus on Food Contact Surfaces: Relationship with Temperature and Cell Surface Hydrophobicity. *Food Control* **2015**, *50*, 930–936. https://doi.org/10.1016/j.foodcont.2014.10.048.

(108) Oliveira, R.; Melo, L.; Oliveira, A.; Salgueiro, R. Polysaccharide Production and Biofilm Formation by Pseudomonas Fluorescens: Effects of PH and Surface Material. *Colloids Surfaces B Biointerfaces* **1994**, *2* (1–3), 41–46. https://doi.org/10.1016/0927-7765(94)80016-2.

(109) Ho, Y.-R.; Li, C.-M.; Yu, C.-H.; Lin, Y.-J.; Wu, C.-M.; Harn, I.-C.; Tang, M.-J.; Chen, Y.-T.; Shen, F.-C.; Lu, C.-Y.; Tsai, T.-C.; Wu, J.-J. The Enhancement of Biofilm Formation in Group B Streptococcal Isolates at Vaginal PH. *Med. Microbiol. Immunol.* **2013**, *202* (2), 105–115.

https://doi.org/10.1007/s00430-012-0255-0.

(110) Manetti, A. G. O.; Köller, T.; Becherelli, M.; Buccato, S.; Kreikemeyer, B.; Podbielski, A.; Grandi, G.; Margarit, I. Environmental Acidification Drives S. Pyogenes Pilus Expression and Microcolony Formation on Epithelial Cells in a FCT-Dependent Manner. *PLoS One* **2010**, *5* (11), e13864. https://doi.org/10.1371/journal.pone.0013864.

(111) Florea, M.; Hagemann, H.; Santosa, G.; Abbott, J.; Micklem, C. N.; Spencer-Milnes, X.; de Arroyo Garcia, L.; Paschou, D.; Lazenbatt, C.; Kong, D.; Chughtai, H.; Jensen, K.; Freemont, P. S.; Kitney, R.; Reeve, B.; Ellis, T. Engineering Control of Bacterial Cellulose Production Using a Genetic Toolkit and a New Cellulose-Producing Strain. *Proc. Natl. Acad. Sci.* **2016**, *113* (24), E3431–E3440. https://doi.org/10.1073/pnas.1522985113.

(112) Feng, J.; Gu, Y.; Quan, Y.; Zhang, W.; Cao, M.; Gao, W.; Song, C.; Yang, C.; Wang, S. Recruiting a New Strategy to Improve Levan Production in Bacillus Amyloliquefaciens. *Sci. Rep.* **2015**, *5* (1), 13814. https://doi.org/10.1038/srep13814.

(113) Tay, P. K. R.; Nguyen, P. Q.; Joshi, N. S. A Synthetic Circuit for Mercury Bioremediation Using Self-Assembling Functional Amyloids. *ACS Synth. Biol.* **2017**, *6* (10), 1841–1850. https://doi.org/10.1021/acssynbio.7b00137.

(114) Moser, F.; Tham, E.; González, L. M.; Lu, T. K.; Voigt, C. A. Light-Controlled, High-Resolution Patterning of Living Engineered Bacteria Onto Textiles, Ceramics, and Plastic. *Adv. Funct. Mater.* **2019**, *29* (30), 1901788. https://doi.org/10.1002/adfm.201901788.

(115) Jin, X.; Riedel-Kruse, I. H. Biofilm Lithography Enables High-Resolution Cell Patterning via Optogenetic Adhesin Expression. *Proc. Natl. Acad. Sci.* **2018**, *115* (14), 3698–3703. https://doi.org/10.1073/pnas.1720676115.

(116) Jiang, L.; Song, X.; Li, Y.; Xu, Q.; Pu, J.; Huang, H.; Zhong, C. Programming Integrative Extracellular and Intracellular Biocatalysis for Rapid, Robust, and Recyclable Synthesis of Trehalose. *ACS Catal.* **2018**, *8* (3), 1837–1842. https://doi.org/10.1021/acscatal.7b03445.

(117) Dong, H.; Zhang, W.; Xuan, Q.; Zhou, Y.; Zhou, S.; Huang, J.; Wang, P. Binding Peptide-Guided Immobilization of Lipases with Significantly Improved Catalytic Performance Using Escherichia Coli BL21(DE3) Biofilms as a Platform. *ACS Appl. Mater. Interfaces* **2021**, *13* (5), 6168–6179. https://doi.org/10.1021/acsami.0c18298.

(118) Tay, P. K. R.; Manjula-Basavanna, A.; Joshi, N. S. Repurposing Bacterial Extracellular Matrix for Selective and Differential Abstraction of Rare Earth Elements. *Green Chem.* **2018**, *20* (15), 3512–3520. https://doi.org/10.1039/C8GC01355A.

(119) Pu, J.; Liu, Y.; Zhang, J.; An, B.; Li, Y.; Wang, X.; Din, K.; Qin, C.; Li, K.; Cui, M.; Liu, S.; Huang, Y.; Wang, Y.; Lv, Y.; Huang, J.; Cui, Z.; Zhao, S.; Zhong, C. Virus Disinfection from Environmental Water Sources Using Living Engineered Biofilm Materials. *Adv. Sci.* **2020**, *7* (14), 1–8. https://doi.org/10.1002/advs.201903558.

(120) Kalyoncu, E.; Ahan, R. E.; Olmez, T. T.; Safak Seker, U. O. Genetically Encoded Conductive Protein Nanofibers Secreted by Engineered Cells. *RSC Adv.* **2017**, *7* (52), 32543–32551. https://doi.org/10.1039/C7RA06289C.

(121) Duraj-Thatte, A. M.; Praveschotinunt, P.; Nash, T. R.; Ward, F. R.; Nguyen, P. Q.; Joshi, N. S. Modulating Bacterial and Gut Mucosal Interactions with Engineered Biofilm Matrix Proteins. *Sci. Rep.* **2018**, *8* (1), 3475. https://doi.org/10.1038/s41598-018-21834-8.

(122) An, B.; Wang, Y.; Jiang, X.; Ma, C.; Mimee, M.; Moser, F.; Li, K.; Wang, X.; Tang, T.-C.; Huang, Y.; Liu, Y.; Lu, T. K.; Zhong, C. Programming Living Glue Systems to Perform Autonomous Mechanical Repairs. *Matter* **2020**, *3* (6), 2080–2092. https://doi.org/10.1016/j.matt.2020.09.006.

(123) Duraj-Thatte, A. M.; Manjula-Basavanna, A.; Rutledge, J.; Xia, J.; Hassan, S.; Sourlis, A.; Rubio, A. G.; Lesha, A.; Zenkl, M.; Kan, A.; Weitz, D. A.; Zhang, Y. S.; Joshi, N. S. Programmable Microbial Ink for 3D Printing of Living Materials Produced from Genetically Engineered Protein Nanofibers. *Nat. Commun.* **2021**, *12* (1), 6600. https://doi.org/10.1038/s41467-021-26791-x.

(124) Balasubramanian, S.; Yu, K.; Cardenas, D. V.; Aubin-Tam, M.-E.; Meyer, A. S. Emergent Biological Endurance Depends on Extracellular Matrix Composition of Three-Dimensionally Printed Escherichia Coli Biofilms. *ACS Synth. Biol.* **2021**, *10* (11), 2997–3008. https://doi.org/10.1021/acssynbio.1c00290.

(125) Schofield, R. M. .; Nesson, M. .; Richardson, K. .; Wyeth, P. Zinc Is Incorporated into Cuticular "Tools" after Ecdysis: The Time Course of the Zinc Distribution in "Tools" and Whole Bodies of an Ant and a Scorpion. *J. Insect Physiol.* **2003**, *49* (1), 31–44. https://doi.org/10.1016/S0022-1910(02)00224-X.

(126) Politi, Y.; Priewasser, M.; Pippel, E.; Zaslansky, P.; Hartmann, J.; Siegel, S.; Li, C.; Barth, F. G.; Fratzl, P. A Spider's Fang: How to Design an Injection Needle Using Chitin-Based Composite Material. *Adv. Funct. Mater.* **2012**, *22* (12), 2519–2528. https://doi.org/10.1002/adfm.201200063.

(127) Broomell, C. C.; Mattoni, M. A.; Zok, F. W.; Waite, J. H. Critical Role of Zinc in Hardening of Nereis Jaws. *J. Exp. Biol.* **2006**, *209* (16), 3219–3225. https://doi.org/10.1242/jeb.02373.

(128) Birkedal, H.; Khan, R. K.; Slack, N.; Broomell, C.; Lichtenegger, H. C.; Zok, F.; Stucky, G. D.; Waite, J. H. Halogenated Veneers: Protein Cross-Linking and Halogenation in the Jaws of Nereis, a Marine Polychaete Worm. *ChemBioChem* **2006**, *7* (9), 1392–1399. https://doi.org/10.1002/cbic.200600160.

(129) Harrington, M. J.; Masic, A.; Holten-Andersen, N.; Waite, J. H.; Fratzl, P. Iron-Clad Fibers: A Metal-Based Biological Strategy for Hard Flexible Coatings. *Science (80-.).* **2010**, *328* (5975), 216–220. https://doi.org/10.1126/science.1181044.

(130) Holten-Andersen, N.; Mates, T. E.; Toprak, M. S.; Stucky, G. D.; Zok, F. W.; Waite, J. H. Metals and the Integrity of a Biological Coating: The Cuticle of Mussel Byssus. *Langmuir* **2009**, *25* (6), 3323–3326. https://doi.org/10.1021/la8027012.

(131) Braun, M.; Menges, M.; Opoku, F.; Smith, A. M. The Relative Contribution of Calcium, Zinc and Oxidation-Based Cross-Links to the Stiffness of Arion Subfuscus Glue. *J. Exp. Biol.* **2012**, *216* (8), 1475–1483. https://doi.org/10.1242/jeb.077149.

(132) Stewart, R. J.; Weaver, J. C.; Morse, D. E.; Waite, J. H. The Tube Cement of Phragmatopoma Californica: A Solid Foam. *J. Exp. Biol.* **2004**, *207* (26), 4727–4734. https://doi.org/10.1242/jeb.01330.

(133) Almeida, M.; Reis, R. L.; Silva, T. H. Marine Invertebrates Are a Source of Bioadhesives with Biomimetic Interest. *Mater. Sci. Eng. C* **2020**, *108* (September 2019), 110467. https://doi.org/10.1016/j.msec.2019.110467.

(134) Schmitt, C. N. Z.; Politi, Y.; Reinecke, A.; Harrington, M. J. Role of Sacrificial Protein–Metal

Bond Exchange in Mussel Byssal Thread Self-Healing. *Biomacromolecules* **2015**, *16* (9), 2852–2861. https://doi.org/10.1021/acs.biomac.5b00803.

(135) House, E.; Collingwood, J.; Khan, A.; Korchazkina, O.; Berthon, G.; Exley, C. Aluminium, Iron, Zinc and Copper Influence the in Vitro Formation of Amyloid Fibrils of Aβ42 in a Manner Which May Have Consequences for Metal Chelation Therapy in Alzheimer's Disease. *J. Alzheimer's Dis.* **2004**, *6* (3), 291–301. https://doi.org/10.3233/JAD-2004-6310.

(136) Mujika, J. I.; Rodríguez-Guerra Pedregal, J.; Lopez, X.; Ugalde, J. M.; Rodríguez-Santiago, L.; Sodupe, M.; Maréchal, J.-D. Elucidating the 3D Structures of Al(Iii)–Aβ Complexes: A Template Free Strategy Based on the Pre-Organization Hypothesis. *Chem. Sci.* **2017**, *8* (7), 5041–5049. https://doi.org/10.1039/C7SC01296A.

(137) Faller, P.; Hureau, C. Bioinorganic Chemistry of Copper and Zinc Ions Coordinated to Amyloid-β Peptide. *Dalt. Trans.* **2009**, No. 7, 1080–1094. https://doi.org/10.1039/B813398K.

(138) Hureau, C. Coordination of Redox Active Metal Ions to the Amyloid Precursor Protein and to Amyloid-β Peptides Involved in Alzheimer Disease. Part 1: An Overview. *Coord. Chem. Rev.* **2012**, *256* (19–20), 2164–2174. https://doi.org/10.1016/j.ccr.2012.03.037.

(139) Nair, N. G.; Perry, G.; Smith, M. A.; Reddy, V. P. NMR Studies of Zinc, Copper, and Iron Binding to Histidine, the Principal Metal Ion Complexing Site of Amyloid-β Peptide. *J. Alzheimer's Dis.* **2010**, *20* (1), 57–66. https://doi.org/10.3233/JAD-2010-1346.

(140) Hidalgo, G.; Chen, X.; Hay, A. G.; Lion, L. W. Curli Produced by Escherichia Coli Phl628 Provide Protection from Hg(Ii)∇. *Appl. Environ. Microbiol.* **2010**, *76* (20), 6939–6941. https://doi.org/10.1128/AEM.01254-10.

(141) Khoo, R. Z.; Chow, W. S.; Ismail, H. Sugarcane Bagasse Fiber and Its Cellulose Nanocrystals for Polymer Reinforcement and Heavy Metal Adsorbent: A Review. *Cellulose* **2018**, *25* (8), 4303–4330. https://doi.org/10.1007/s10570-018-1879-z.

(142) Jamshaid, A.; Hamid, A.; Muhammad, N.; Naseer, A.; Ghauri, M.; Iqbal, J.; Rafiq, S.; Shah, N. S. Cellulose-Based Materials for the Removal of Heavy Metals from Wastewater - An Overview. *ChemBioEng Rev.* **2017**, *4* (4), 240–256. https://doi.org/10.1002/cben.201700002.

(143) Božič, M.; Liu, P.; Mathew, A. P.; Kokol, V. Enzymatic Phosphorylation of Cellulose Nanofibers to New Highly-Ions Adsorbing, Flame-Retardant and Hydroxyapatite-Growth Induced Natural Nanoparticles. *Cellulose* **2014**, *21* (4), 2713–2726. https://doi.org/10.1007/s10570-014-0281-8.

(144) Olar, R.; Badea, M.; Chifiriuc, M. C. Metal Complexes—A Promising Approach to Target Biofilm Associated Infections. *Molecules* **2022**, *27* (3), 758. https://doi.org/10.3390/molecules27030758.

(145) Deng, C.; Li, X.; Xue, X.; Pashley, R. M. The Effects of Low Levels of Trivalent Ions on a Standard Strain of Escherichia Coli (ATCC 11775) in Aqueous Solutions. *Microbiologyopen* **2018**, *7* (3), e00574. https://doi.org/10.1002/mbo3.574.

(146) Ogasawara, H.; Shinohara, S.; Yamamoto, K.; Ishihama, A. Novel Regulation Targets of the Metal-Response BasS–BasR Two-Component System of Escherichia Coli. *Microbiology* **2012**, *158* (6), 1482–1492. https://doi.org/10.1099/mic.0.057745-0.

(147) Jubelin, G.; Vianney, A.; Beloin, C.; Ghigo, J.-M.; Lazzaroni, J.-C.; Lejeune, P.; Dorel, C. CpxR/OmpR Interplay Regulates Curli Gene Expression in Response to Osmolarity in

Escherichia Coli. *J. Bacteriol.* **2005**, *187* (6), 2038–2049. https://doi.org/10.1128/JB.187.6.2038-2049.2005.

(148) Myers, J. A.; Curtis, B. S.; Curtis, W. R. Improving Accuracy of Cell and Chromophore Concentration Measurements Using Optical Density. *BMC Biophys.* **2013**, *6* (1), 4. https://doi.org/10.1186/2046-1682-6-4.

(149) Zeng, G.; Vad, B. S.; Dueholm, M. S.; Christiansen, G.; Nilsson, M.; Tolker-Nielsen, T.; Nielsen, P. H.; Meyer, R. L.; Otzen, D. E. Functional Bacterial Amyloid Increases Pseudomonas Biofilm Hydrophobicity and Stiffness. *Front. Microbiol.* **2015**, *6* (OCT), 1–14. https://doi.org/10.3389/fmicb.2015.01099.

(150) Siri, M.; Mangiarotti, A.; Vazquez-Davila, M.; Bidan, C. M. Curli Fibers in Escherichia Coli Biofilms: The Influence of Water Availability on Amyloid Structure and Properties. *bioRxiv* **2022**. https://doi.org/https://doi.org/10.1101/2022.11.21.517345.

(151) Chapman, M. R.; Robinson, L. S.; Pinkner, J. S.; Roth, R.; Heuser, J.; Hammar, M.; Normark, S.; Hultgren, S. J. Role of Escherichia Coli Curli Operons in Directing Amyloid Fiber Formation. *Science (80-.).* **2002**, *295* (5556), 851–855. https://doi.org/10.1126/science.1067484.

(152) Barth, A.; Haris, P. I.; Goormaghtigh, E. FTIR Data Processing and Analysis Tools. *Biol. Biomed. infrared Spectrosc.* **2009**, *2*, 104–108. https://doi.org/10.3233/978-1-60750-045-2-104.

(153) Goormaghtigh, E.; Ruysschaert, J.-M. Subtraction of Atmospheric Water Contribution in Fourier Transform Infrared Spectroscopy of Biological Membranes and Proteins. *Spectrochim. Acta Part A Mol. Spectrosc.* **1994**, *50* (12), 2137–2144. https://doi.org/10.1016/0584-8539(94)00167-7.

(154) GOORMAGHTIGH, E.; CABIAUX, V.; RUYSSCHAERT, J.-M. Secondary Structure and Dosage of Soluble and Membrane Proteins by Attenuated Total Reflection Fourier-Transform Infrared Spectroscopy on Hydrated Films. *Eur. J. Biochem.* **1990**, *193* (2), 409–420. https://doi.org/10.1111/j.1432-1033.1990.tb19354.x.

(155) Sarroukh, R.; Goormaghtigh, E.; Ruysschaert, J.-M.; Raussens, V. ATR-FTIR: A “Rejuvenated” Tool to Investigate Amyloid Proteins. *Biochim. Biophys. Acta - Biomembr.* **2013**, *1828* (10), 2328–2338. https://doi.org/10.1016/j.bbamem.2013.04.012.

(156) Stanley-Gray, J.; Zhang, Z.; Venkataraman, D. Updated Coordination Geometry Table of the D-Block Elements and Their Ions. *J. Chem. Educ.* **2021**, *98* (7), 2476–2481. https://doi.org/10.1021/acs.jchemed.1c00364.

(157) Bhardwaj, N. C.; Jadon, S. C. S.; Singh, R. V. Aluminium(III) Complexes with Usual and Unusual Coordination Numbers. *Synth. React. Inorg. Met. Chem.* **1994**, *24* (8), 1267–1279. https://doi.org/10.1080/00945719408002143.

(158) Katz, A. K.; Glusker, J. P.; Beebe, S. A.; Bock, C. W. Calcium Ion Coordination: A Comparison with That of Beryllium, Magnesium, and Zinc. *J. Am. Chem. Soc.* **1996**, *118* (24), 5752–5763. https://doi.org/10.1021/ja953943i.

(159) Horvat, M.; Pannuri, A.; Romeo, T.; Dogsa, I.; Stopar, D. Viscoelastic Response of Escherichia Coli Biofilms to Genetically Altered Expression of Extracellular Matrix Components. *Soft Matter* **2019**, *15* (25), 5042–5051. https://doi.org/10.1039/C9SM00297A.

(160) Periasamy, S.; Nair, H. A. S.; Lee, K. W. K.; Ong, J.; Goh, J. Q. J.; Kjelleberg, S.; Rice, S. A. Pseudomonas Aeruginosa PAO1 Exopolysaccharides Are Important for Mixed Species Biofilm

Community Development and Stress Tolerance. *Front. Microbiol.* **2015**, *6* (AUG), 1–10. https://doi.org/10.3389/fmicb.2015.00851.

(161) Li, W.-W.; Yu, H.-Q. Insight into the Roles of Microbial Extracellular Polymer Substances in Metal Biosorption. *Bioresour. Technol.* **2014**, *160*, 15–23. https://doi.org/10.1016/j.biortech.2013.11.074.

(162) Oshima, T.; Kondo, K.; Ohto, K.; Inoue, K.; Baba, Y. Preparation of Phosphorylated Bacterial Cellulose as an Adsorbent for Metal Ions. *React. Funct. Polym.* **2008**, *68* (1), 376–383. https://doi.org/10.1016/j.reactfunctpolym.2007.07.046.

(163) Hosny, W. M.; Basta, A. H.; El-Saied, H. *Metal Chelates with Some Cellulose Derivatives: Synthesis and V. Characterization of Some Iron(III) Complexes with Cellulose Ethers*; 1997; Vol. 42.

(164) Jumper, J.; Evans, R.; Pritzel, A.; Green, T.; Figurnov, M.; Ronneberger, O.; Tunyasuvunakool, K.; Bates, R.; Žídek, A.; Potapenko, A.; Bridgland, A.; Meyer, C.; Kohl, S. A. A.; Ballard, A. J.; Cowie, A.; Romera-Paredes, B.; Nikolov, S.; Jain, R.; Adler, J.; Back, T.; Petersen, S.; Reiman, D.; Clancy, E.; Zielinski, M.; Steinegger, M.; Pacholska, M.; Berghammer, T.; Bodenstein, S.; Silver, D.; Vinyals, O.; Senior, A. W.; Kavukcuoglu, K.; Kohli, P.; Hassabis, D. Highly Accurate Protein Structure Prediction with AlphaFold. *Nature* **2021**, *596* (7873), 583–589. https://doi.org/10.1038/s41586-021-03819-2.

(165) Varadi, M.; Anyango, S.; Deshpande, M.; Nair, S.; Natassia, C.; Yordanova, G.; Yuan, D.; Stroe, O.; Wood, G.; Laydon, A.; Žídek, A.; Green, T.; Tunyasuvunakool, K.; Petersen, S.; Jumper, J.; Clancy, E.; Green, R.; Vora, A.; Lutfi, M.; Figurnov, M.; Cowie, A.; Hobbs, N.; Kohli, P.; Kleywegt, G.; Birney, E.; Hassabis, D.; Velankar, S. AlphaFold Protein Structure Database: Massively Expanding the Structural Coverage of Protein-Sequence Space with High-Accuracy Models. *Nucleic Acids Res.* **2022**, *50* (D1), D439–D444. https://doi.org/10.1093/nar/gkab1061.

(166) van Gestel, J.; Weissing, F. J.; Kuipers, O. P.; Kovács, Á. T. Density of Founder Cells Affects Spatial Pattern Formation and Cooperation in Bacillus Subtilis Biofilms. *ISME J.* **2014**, *8* (10), 2069–2079. https://doi.org/10.1038/ismej.2014.52.

(167) Lambert, G.; Bergman, A.; Zhang, Q.; Bortz, D.; Austin, R. Physics of Biofilms: The Initial Stages of Biofilm Formation and Dynamics. *New J. Phys.* **2014**, *16* (4), 045005. https://doi.org/10.1088/1367-2630/16/4/045005.

(168) Teitzel, G. M.; Parsek, M. R. Heavy Metal Resistance of Biofilm and Planktonic Pseudomonas Aeruginosa. *Appl. Environ. Microbiol.* **2003**, *69* (4), 2313–2320. https://doi.org/10.1128/AEM.69.4.2313-2320.2003.

(169) Epstein, W.; Schultz, S. G. Cation Transport in Escherichia Coli. *J. Gen. Physiol.* **1965**, *49* (2), 221–234. https://doi.org/10.1085/jgp.49.2.221.

(170) Flory, P. J.; Rehner, J. Statistical Mechanics of Cross-Linked Polymer Networks II. Swelling. *J. Chem. Phys.* **1943**, *11* (11), 521–526. https://doi.org/10.1063/1.1723792.

(171) Ziege, R. Growth Dynamics and Mechanical Properties of E. Coli Biofilms, Universität Potsdam, 2022. https://doi.org/https://doi.org/10.25932/publishup-55986.

(172) Tyrikos-Ergas, T.; Gim, S.; Huang, J.-Y.; Pinzón Martín, S.; Varón Silva, D.; Seeberger, P. H.; Delbianco, M. Synthetic Phosphoethanolamine-Modified Oligosaccharides Reveal the Importance of Glycan Length and Substitution in Biofilm-Inspired Assemblies. *Nat. Commun.*

2022, *13* (1), 3954. https://doi.org/10.1038/s41467-022-31633-5.

(173) Abdelwahab, M. T.; Kalyoncu, E.; Onur, T.; Baykara, M. Z.; Seker, U. O. S. Genetically-Tunable Mechanical Properties of Bacterial Functional Amyloid Nanofibers. *Langmuir* **2017**, *33* (17), 4337–4345. https://doi.org/10.1021/acs.langmuir.7b00112.

(174) Geisel, S.; Secchi, E.; Vermant, J. Experimental Challenges in Determining the Rheological Properties of Bacterial Biofilms. *Interface Focus* **2022**, *12* (6). https://doi.org/10.1098/rsfs.2022.0032.

(175) Charlton, S. G. V.; Kurz, D. L.; Geisel, S.; Jimenez-Martinez, J.; Secchi, E. The Role of Biofilm Matrix Composition in Controlling Colony Expansion and Morphology. *Interface Focus* **2022**, *12* (6). https://doi.org/10.1098/rsfs.2022.0035.

(176) Hollenbeck, E. C.; Antonoplis, A.; Chai, C.; Thongsomboon, W.; Fuller, G. G.; Cegelski, L. Phosphoethanolamine Cellulose Enhances Curli-Mediated Adhesion of Uropathogenic Escherichia Coli to Bladder Epithelial Cells. *Proc. Natl. Acad. Sci.* **2018**, *115* (40), 10106–10111. https://doi.org/10.1073/pnas.1801564115.

(177) Park, D.; Yun, Y.-S.; Park, J. M. Studies on Hexavalent Chromium Biosorption by Chemically-Treated Biomass of Ecklonia Sp. *Chemosphere* **2005**, *60* (10), 1356–1364. https://doi.org/10.1016/j.chemosphere.2005.02.020.

(178) Yu, C.; Irudayaraj, J. Spectroscopic Characterization of Microorganisms by Fourier Transform Infrared Microspectroscopy. *Biopolymers* **2005**, *77* (6), 368–377. https://doi.org/10.1002/bip.20247.

(179) Socrates, G. *Infrared and Raman Characteristic Group Frequencies: Tables and Charts*, Third Edit.; John Wiley & Sons, L., Ed.; John Wiley & Sons, LTD: Chichester, 2001.

(180) Messias, A.; Santos, D. E. S.; Pontes, F. J. S.; Soares, T. A. The Tug of War between Al 3+ and Na + for Order–Disorder Transitions in Lipid-A Membranes. *Phys. Chem. Chem. Phys.* **2021**, *23* (28), 15127–15137. https://doi.org/10.1039/D1CP02173G.

(181) Graber, Z. T.; Shi, Z.; Baumgart, T. Cations Induce Shape Remodeling of Negatively Charged Phospholipid Membranes. *Phys. Chem. Chem. Phys.* **2017**, *19* (23), 15285–15295. https://doi.org/10.1039/C7CP00718C.

(182) Zhou, X.; Tan, J.; Zheng, L.; Pillai, S.; Li, B.; Xu, P.; Zhang, B.; Zhang, Y. The Opposite Effects of Cu(Ii) and Fe(Iii) on the Assembly of Glucagon Amyloid Fibrils. *RSC Adv.* **2012**, *2* (12), 5418. https://doi.org/10.1039/c2ra20651j.

(183) Dueholm, M. S.; Nielsen, S. B.; Hein, K. L.; Nissen, P.; Chapman, M.; Christiansen, G.; Nielsen, P. H.; Otzen, D. E. Fibrillation of the Major Curli Subunit CsgA under a Wide Range of Conditions Implies a Robust Design of Aggregation. *Biochemistry* **2011**, *50* (39), 8281–8290. https://doi.org/10.1021/bi200967c.

(184) Zhou, L.; Li, S.; Su, Y.; Yi, X.; Zheng, A.; Deng, F. Interaction between Histidine and Zn(II) Metal Ions over a Wide PH as Revealed by Solid-State NMR Spectroscopy and DFT Calculations. *J. Phys. Chem. B* **2013**, *117* (30), 8954–8965. https://doi.org/10.1021/jp4041937.

(185) Volesky, B. Biosorption and Me. *Water Res.* **2007**, *41* (18), 4017–4029. https://doi.org/10.1016/j.watres.2007.05.062.

(186) Grumbein, S.; Opitz, M.; Lieleg, O. Selected Metal Ions Protect Bacillus Subtilis Biofilms from

Erosion. *Metallomics* **2014**, *6* (8), 1441–1450. https://doi.org/10.1039/c4mt00049h.

(187) Joshi, V. J.; Santani, D. D. Physicochemical Characterization and Heavy Metal Concentration in Effluent of Textile Industry. *Univers. J. Environ. Res. Technol.* **2012**, *2* (2).

(188) Sankpal, S. T.; Naikwade, P. V. Heavy Metal Concentration in Effluent Discharge of Pharmaceutical Industries. *Sci. Res. Report.* **2012**, *2* (1), 88–90.

(189) Barth, A. The Infrared Absorption of Amino Acid Side Chains. *Prog. Biophys. Mol. Biol.* **2000**, *74* (3–5), 141–173. https://doi.org/10.1016/S0079-6107(00)00021-3.

(190) Manning, G. S. Limiting Laws and Counterion Condensation in Polyelectrolyte Solutions I. Colligative Properties. *J. Chem. Phys.* **1969**, *51* (3), 924–933. https://doi.org/10.1063/1.1672157.

(191) Manning, G. S. Counterion Condensation on Charged Spheres, Cylinders, and Planes. *J. Phys. Chem. B* **2007**, *111* (29), 8554–8559. https://doi.org/10.1021/jp0670844.

(192) Zhivkov, A. M. Electric Properties of Carboxymethyl Cellulose. In *Cellulose - Fundamental Aspects*; InTech, 2013. https://doi.org/10.5772/56935.

10. Declaration of originality / Eidesstattliche Erklärung

I hereby declare in lieu of an oath that this thesis with the title "Tuning the viscoelasticity of *Escherichia coli* biofilms: interplay between extrinsic and intrinsic factors" has not previously been submitted to any other university and that it was written independently and exclusively with the sources and aids indicated.

Hiermit versichere ich an Eides statt, dass ich, Adrien Sarlet, die Arbeit zum Thema „Modulation der Viskoelastizität von *Escherichia col*i Biofilmen: Zusammenspiel zwischen extrinsischen und intrinsischen Faktoren“ bisher an keiner anderen Hochschule eingereicht habe. Die Arbeit wurde selbständig und ausschließlich mit den angegebenen Quellen und Hilfsmittel angefertigt.

Potsdam-Golm, 08.02.2023

Adrien Sarlet

11. Acknowledgments

First of all, I would like to thank my two supervisors Cécile Bidan and Kerstin Blank for their valuable teaching, coaching, input and guidance throughout the doctoral studies period as well as for having entrusted me with this project. It goes without saying that I have learnt a lot from you scientifically but I also did in soft skills such as writing, presenting, team work and I must forget many others. I hope that this legacy was at least partially reflected in the present work.

I also want to say thank you to Christine Pilz-Allen, Reinhild Dünnebacke and Jeannette Steffen for incessantly bringing order out of chaos and maintaining functional laboratories, without which no research could be performed. I kindly remember and appreciate the help provided by Valentin Ruffine already years ago, at the very beginning of this project. With them, I would also like to thank every member of the Biofilm-based Materials and Mechano(bio)chemistry research groups for their support, advice and constructive discussions. In particular, I would like to thank once more Christine for having introduced me to biofilm culture and Geonho Song to rheology. I also thank Ricardo Ziege for the microindentation data and Macarena Siri for her help in acquiring and processing the FTIR spectra. A special thank goes to Laura Zorzetto for being the most enjoyable person to work with. My only regret is that our projects never overlapped so that we could never collaborate as much as I did with the others.

I am grateful to Regine Hengge and Diego Serra for kindly providing the *E. coli* strains used in this work.

Another series of thanks goes to the International Max Planck Research School (IMPRS) on Multiscale Bio-Systems for funding and supporting my PhD; particularly, Angelo Valleriani, Susann Weber and Valerie Lecker for coordinating the IMPRS; and my mentor Rumiana Dimova for her questions and the resulting inputs. More generally, I also want to thank all IMPRS students and involved PIs for the interesting workshops.

Last but not least, I would like to thank the whole Biomaterials Department for the very pleasant atmosphere I was privileged to work in for more than three years. It is a department where the only

closed doors are those of the laboratories. It is a community where everyone is always ready to lend a hand, answer a question or share a thought. For this reason among others, I would like to thank Peter Fratzl for being the maestro of the biomaterials orchestra and having made possible for me to work in such a unique working environment.

12. Annex

12.1. Influence of metal cations on the viscoelastic properties of *Escherichia coli* biofilms

12.1.1. Osmolality measurement

NaCl solutions, spanning the concentration range from 200 to 550 mM, were prepared as three independent replicates for each point. The osmolalities of these standard solutions were measured, a linear regression was fitted using the least squares method with the *lm* function in R (R Core Team; version 4.0.5) and the resulting calibration curve was plotted. Subsequently, the osmolality of all used salt solutions (220 mM) was determined from three aliquots of the same solution. For the osmolality control solution used for biofilm experiments, a NaCl solution was prepared with a concentration (409 mM) that matched the osmolality of the 220 mM $FeCl_3$ solution of 754 mOsm kg^{-1} (Annex Figure 22).

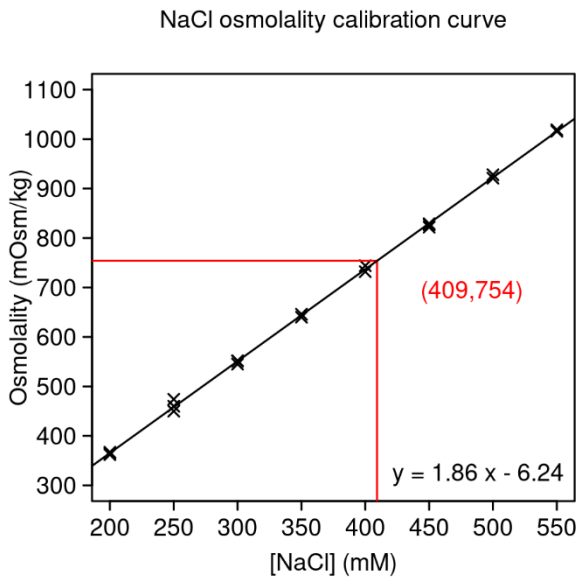

Figure 22. Osmolality calibration curve obtained with NaCl solutions of different concentrations. The 220 mM $FeCl_3$ solution has an osmolality of 754 mOsm kg^{-1}. This corresponds to a NaCl concentration of 409 mM.

12.1.2. Amplitude sweeps for AR3110 samples with ascending and descending strain amplitude

Amplitude sweeps were performed for AR3110 biofilms with and without the addition of 10% (v/w) ultrapure water (Annex Figure 23). The oscillation frequency was set to 10 rad s^{-1}. The strain amplitude was increased from 0.01% to 100% with 7 points per decade and then decreased again.

These cycles of ascending and descending strain amplitude were repeated 3x. One experiment with 3 cycles lasted approximately 45 min.

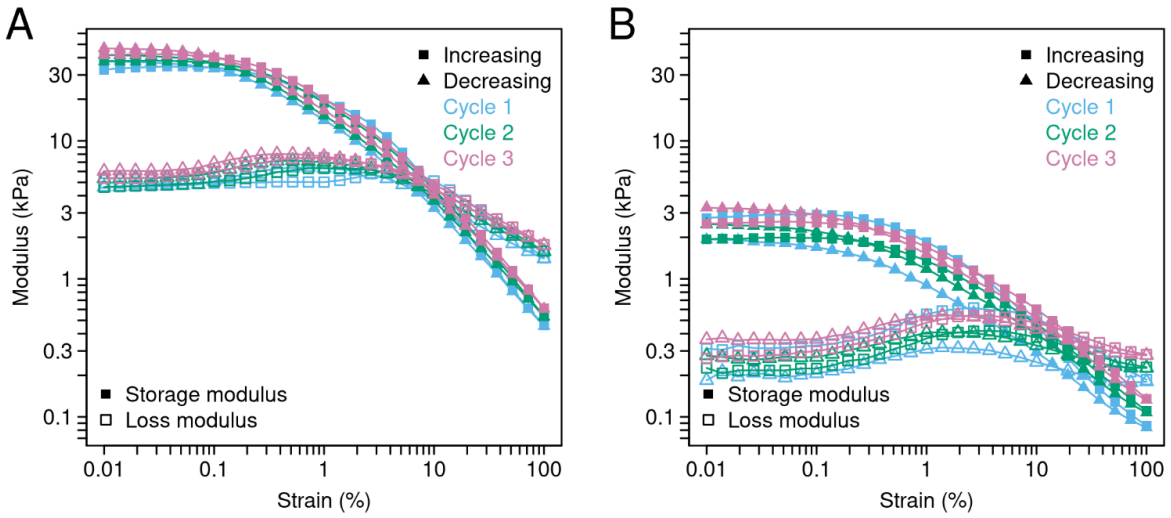

Figure 23. Amplitude sweeps of the strain AR3110. A: Amplitude sweep of a neat sample, consisting of three cycles of ascending and descending strain amplitudes. B: Amplitude sweep of a sample diluted with 10% (v/w) ultrapure water, consisting of three cycles of ascending and descending strain amplitudes. The amplitude sweeps were performed at a frequency of 10 rad s^{-1}.

12.1.3. Frequency sweeps for AR3110 samples prepared under different conditions

Frequency sweeps were performed for AR3110 samples (1) with and without the addition of 10% (v/w) ultrapure water, (2) preceded or not by an amplitude sweep or (3) starting from the highest (descending) or the lowest (ascending) frequency. The applied strain (γ = 0.02%) was determined from the linear viscoelastic range of the amplitude sweeps (Annex Figure 23). The frequency range of two decades was centred on the frequency used for the amplitude sweeps (ω = 10 rad s^{-1}) (Annex Figure 24).

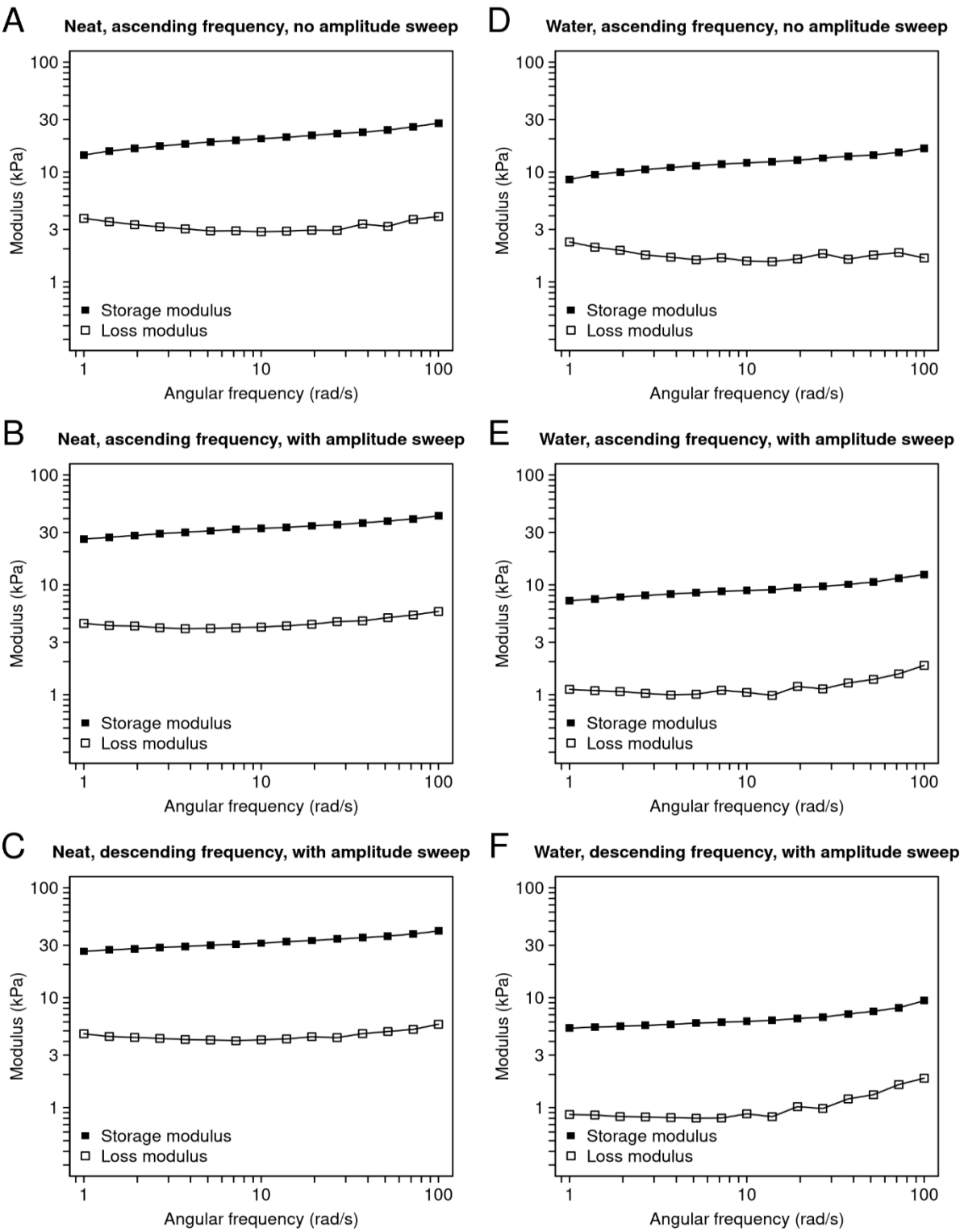

Figure 24. Frequency sweeps of the strain AR3110. A: Frequency sweep of a neat sample, performed with ascending frequency and γ = 0.02%). B: Frequency sweep of a neat sample, performed with ascending frequency and γ = 0.02%. Before the frequency sweep, the sample was subjected to one cycle of ascending and descending strain amplitudes. C: Frequency sweep of a neat sample, performed with descending frequency and γ = 0.02%. Before the frequency sweep, the sample was subjected to one cycle of ascending and descending strain amplitudes. D: Frequency sweep of a sample diluted with 10% (v/w) ultrapure water. The frequency sweep was performed with ascending frequency and γ = 0.02%. E: Frequency sweep of a sample diluted with 10% (v/w) ultrapure water. The frequency sweep was performed with ascending frequency and γ = 0.02%. Before the frequency sweep, the sample was subjected to one cycle of ascending and descending strain amplitudes. F: Frequency sweep of a sample diluted with 10% (v/w) ultrapure water. The frequency sweep was performed with descending frequency and γ = 0.02%. Before the frequency sweep, the sample was subjected to one cycle of ascending and descending strain amplitudes.

In addition, a frequency sweep was performed over five decades (ω = 0.001-100 rad s^{-1}), using a neat or diluted sample (with preceding amplitude sweep and descending strain amplitude). The measurement was performed to determine the relaxation time of the biofilm samples; however, drying of the samples significantly affected the data in the low frequency range (Annex Figure 25).

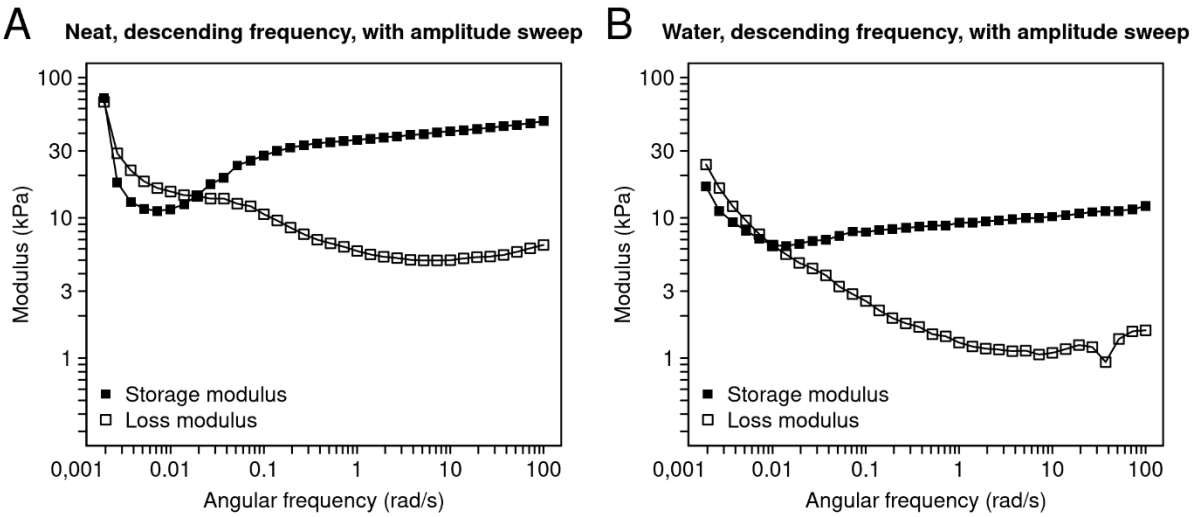

Figure 25. Extended frequency sweeps of the strain AR3110. A: Frequency sweep of a neat sample, performed with descending frequency and γ = 0.02%. Before the frequency sweep, the sample was subjected to one cycle of ascending and descending strain amplitudes. B: Frequency sweep of a sample diluted with 10% (v/w) ultrapure water. The frequency sweep was performed with descending frequency and γ = 0.02%. Before the frequency sweep, the sample was subjected to one cycle of ascending and descending strain amplitudes.

12.1.4. Effect of diluting biofilm samples with ultrapure water

To determine the effect of adding 10% (v/w) ultrapure water to the different biofilm samples, storage and loss moduli were extracted from the amplitude sweeps of ≥3 independent biofilm samples (see Materials and Methods). The extracted values, as well as their median values, are reported in Tables 17 and 18.

Table 17. Storage moduli (G'_0) of neat biofilms (-) and biofilms diluted (+) with 10% (v/w) ultrapure water.

Matrix composition	Curli pEtN-cellulose		Curli		pEtN-cellulose		Curli pEtN-cellulose (mixed)		Curli pEtN-cellulose (co-seeded)	
Water	**-**	**+**	**-**	**+**	**-**	**+**	**-**	**+**	**-**	**+**
	37933	1940	27500	2703	18200	576	27000	1423	54400	8333
	24400	2933	10017	1213	9157	190	31267	2673	24067	2857
G'_0 (Pa)	28267	5373	16533	1580	30567	1057	45200	6797	51167	5617
	32833	4510								
	20367	4613								
Median	**28267**	**4510**	**16533**	**1580**	**18200**	**576**	**31267**	**2673**	**51167**	**5617**

Table 18. Loss moduli (G''_0) of neat biofilms (-) and biofilms diluted (+) with 10% (v/w) ultrapure water.

Matrix composition	Curli pEtN-cellulose		Curli		pEtN-cellulose		Curli pEtN-cellulose (mixed)		Curli pEtN-cellulose (co-seeded)	
Water	**-**	**+**	**-**	**+**	**-**	**+**	**-**	**+**	**-**	**+**
	4663	217	4360	399	2187	61	3413	134	6390	843
	3197	359	1390	156	1180	11	3137	225	3430	367
G''_0 (Pa)	3297	539	2047	170	3367	107	4923	654	6550	695
	4330	479								
	1950	442								
Median	**3297**	**442**	**2047**	**170**	**2187**	**61**	**3413**	**225**	**6390**	**695**

12.1.5. Dilution experiments with metal cation solutions

To determine the effect of adding solutions of metal cations to the different biofilm samples, storage and loss moduli were extracted from the amplitude sweeps of ≥5 independent biofilm samples (see

Materials and Methods). The extracted values, as well as their median values, are reported in Tables 19 to 28.

Table 19. Storage moduli (G'_0) of AR3110 biofilms incubated with 10% (v/w) ultrapure water or a solution of interest. Pairs of values located in the same line correspond to biofilms grown in the same Petri dish. Samples incubated with NaCl and HCl were grown in the same Petri dish, which is why they share the same water control values.

Matrix composition							**Curli pEtN-cellulose**					
Solution	**$AlCl_3$**	**Water**	**$FeCl_3$**	**Water**	**$ZnCl_2$**	**Water**	**$CaCl_2$**	**Water**	**NaCl**	**Water**	**HCl**	**Water**
	7100	3913	40100	23200	7097	14733	12067	6750	3997	9623	10733	9623
	13333	4893	38400	34333	11367	13767	12700	19167	1803	11000	8163	11000
	7520	2270	33133	24633	14267	20500	8800	21767	2603	12633	4400	12633
	5543	3460	32700	21400	11000	14800	11367	18933	608	1042	1187	1042
	6797	4927	38500	25367	8553	16633	16033	23033	2023	9537	4600	9537
G'_0 (Pa)	3193	2780	171000	52767	17467	16033	23733	20567				
	117667	19133										
	14567	4713										
	20600	5830										
	8073	3973										
	11033	6050										
Q1	**6948**	**3687**	**34450**	**23558**	**9165**	**14750**	**11542**	**18992**	**1803**	**9537**	**4400**	**9537**
Q2 (median)	**8073**	**4713**	**38450**	**25000**	**11183**	**15417**	**12383**	**19867**	**2023**	**9623**	**4600**	**9623**
Q3	**13950**	**5378**	**39700**	**32092**	**13542**	**16483**	**15200**	**21467**	**2603**	**11000**	**8163**	**11000**

Table 20. Loss moduli (G''_0) for AR3110 biofilm samples incubated with 10% (v/w) ultrapure water or a solution of interest. Pairs of values located in the same line correspond to biofilms grown in the same Petri dish. Samples incubated with NaCl and HCl were grown in the same Petri dish, which is why they share the same water control values.

Matrix composition						**Curli pEtN-cellulose**						
Solution	**$AlCl_3$**	**Water**	**$FeCl_3$**	**Water**	**$ZnCl_2$**	**Water**	**$CaCl_2$**	**Water**	**NaCl**	**Water**	**HCl**	**Water**
	1043	587	5690	2820	1457	2067	2520	968	447	878	1067	878
	2187	794	5613	4397	2253	1653	2250	2613	242	1373	1127	1373
	1270	333	4763	2883	2613	2483	1553	2847	380	1770	583	1770
	977	517	4650	2513	2017	1860	2053	2360	99	158	114	158
	1277	979	5383	2990	1630	2487	3093	2993	278	1240	542	1240
G''_0 (Pa)	572	329	22800	6117	2987	1830	4803	3517				
	14633	2060										
	2073	563										
	2850	676										
	1203	582										
	1760	1227										
Q1	**1123**	**540**	**4918**	**2836**	**1727**	**1838**	**2103**	**2423**	**242**	**878**	**542**	**878**
Q2 (median)	**1277**	**587**	**5498**	**2937**	**2135**	**1963**	**2385**	**2730**	**278**	**1240**	**583**	**1240**
Q3	**2130**	**886**	**5671**	**4045**	**2523**	**2379**	**2950**	**2957**	**380**	**1373**	**1067**	**1373**

Table 21. Storage moduli (G'_0) for W3110 biofilms incubated with 10% (v/w) ultrapure water or a solution of interest. Pairs of values located in the same line correspond to biofilms grown in the same Petri dish.

Matrix composition	**Curli**							
Solution	**$AlCl_3$**	**Water**	**$FeCl_3$**	**Water**	**$ZnCl_2$**	**Water**	**$CaCl_2$**	**Water**
G'_0 (Pa)	3550	8737	3287	6630	6427	20967	3900	10133
	21400	9613	9393	11000	2413	4793	3737	8587
	11133	10833	2247	5153	2857	10133	3210	14667
	10500	4973	8290	23067	4717	7167	5777	15367
	9940	6103	3350	5763	1323	5283	4050	10667
	12267	6543	4947	6000	4990	8360	11333	11933
Q1	**10080**	**6213**	**3302**	**5823**	**2524**	**5754**	**3777**	**10267**
Q2 (median)	**10817**	**7640**	**4148**	**6315**	**3787**	**7763**	**3975**	**11300**
Q3	**11983**	**9394**	**7454**	**9908**	**4922**	**9690**	**5345**	**13983**

Table 22. Loss moduli (G''_0) for W3110 biofilms incubated with 10% (v/w) ultrapure water or a solution of interest. Pairs of values located in the same line correspond to biofilms grown in the same Petri dish.

Matrix composition	**Curli**							
Solution	**$AlCl_3$**	**Water**	**$FeCl_3$**	**Water**	**$ZnCl_2$**	**Water**	**$CaCl_2$**	**Water**
G''_0 (Pa)	584	2187	479	1507	1353	3287	710	2093
	4393	2433	2030	2650	481	939	714	1780
	2353	2677	351	1042	516	1780	599	2637
	2063	1253	1630	3467	920	1317	1083	2477
	1833	1697	548	1197	236	861	763	1880
	2327	1477	888	1140	955	1510	2513	2097
Q1	**1891**	**1532**	**496**	**1154**	**490**	**1034**	**711**	**1933**
Q2 (median)	**2195**	**1942**	**718**	**1352**	**718**	**1413**	**739**	**2095**
Q3	**2347**	**2372**	**1445**	**2364**	**946**	**1713**	**1003**	**2382**

Table 23. Storage moduli (G'_0) for AP329 biofilms incubated with 10% (v/w) ultrapure water or a solution of interest. Pairs of values located in the same line correspond to biofilms grown in the same Petri dish.

Matrix composition					**pEtN-cellulose**			
Solution	**$AlCl_3$**	**Water**	**$FeCl_3$**	**Water**	**$ZnCl_2$**	**Water**	**$CaCl_2$**	**Water**
G'_0 (Pa)	5337	3470	1353	1443	1977	3250	5137	11133
	2107	4933	1417	6847	1600	10367	4773	21267
	3530	9213	1623	8413	3153	16500	6960	18933
	9580	10800	6233	9103	2173	10600	4857	17233
	12533	17067	8857	16933	1203	8540	8577	14767
	7843	16567			1870	10233	8157	19800
	10100	4043						
	10767	7387						
Q1	**4885**	**4711**	**1417**	**6847**	**1668**	**8963**	**4927**	**15383**
Q2 (median)	**8712**	**8300**	**1623**	**8413**	**1923**	**10300**	**6048**	**18083**
Q3	**10267**	**12242**	**6233**	**9103**	**2124**	**10542**	**7857**	**19583**

Table 24. Loss moduli (G''_0) for AP329 biofilms incubated with 10% (v/w) ultrapure water or a solution of interest. Pairs of values located in the same line correspond to biofilms grown in the same Petri dish.

Matrix composition					**pEtN-cellulose**			
Solution	**$AlCl_3$**	**Water**	**$FeCl_3$**	**Water**	**$ZnCl_2$**	**Water**	**$CaCl_2$**	**Water**
G''_0 (Pa)	707	345	179	152	375	370	1002	1397
	363	536	185	800	265	1220	933	2660
	571	1077	216	975	558	1970	1377	2450
	1913	1533	988	1190	380	1250	976	2297
	2450	2450	1377	2353	213	969	1800	2013
	1150	1980			334	1100	1680	2703
	1563	448						
	1680	862						
Q1	**673**	**514**	**185**	**800**	**282**	**1002**	**983**	**2084**
Q2 (median)	**1357**	**969**	**216**	**975**	**355**	**1160**	**1189**	**2373**
Q3	**1738**	**1645**	**988**	**1190**	**379**	**1243**	**1604**	**2608**

Table 25. Storage moduli (G'_0) for samples consisting of mixed W3110 and AP329 biofilms incubated with 10% (v/w) ultrapure water or a solution of interest. Pairs of values located in the same line correspond to biofilms grown in the same Petri dish.

Matrix composition	**Curli pEtN-cellulose (mixed)**							
Solution	**$AlCl_3$**	**Water**	**$FeCl_3$**	**Water**	**$ZnCl_2$**	**Water**	**$CaCl_2$**	**Water**
G'_0 (Pa)	1950	15900	4107	20767	4153	9840	8053	19400
	20900	14833	17867	22167	4663	13000	7267	19733
	8627	6020	6640	10600	11467	29333	11800	47767
	6847	11400	15167	19833	8180	14933	6157	46500
	13167	28100	16933	21233	5023	36500	15033	57600
	11833	15700					11967	30400
Q1	**7292**	**12258**	**6640**	**19833**	**4663**	**13000**	**7463**	**22400**
Q2 (median)	**10230**	**15267**	**15167**	**20767**	**5023**	**14933**	**9927**	**38450**
Q3	**12833**	**15850**	**16933**	**21233**	**8180**	**29333**	**11925**	**47450**

Table 26. Loss moduli (G''_0) for samples consisting of mixed W3110 and AP329 biofilms, incubated with 10% (v/w) ultrapure water or a solution of interest. Pairs of values located in the same line correspond to biofilms grown in the same Petri dish.

Matrix composition	**Curli pEtN-cellulose (mixed)**							
Solution	**$AlCl_3$**	**Water**	**$FeCl_3$**	**Water**	**$ZnCl_2$**	**Water**	**$CaCl_2$**	**Water**
G''_0 (Pa)	266	2863	582	3570	770	1757	1420	2983
	3170	2387	3110	4253	830	1850	1280	2690
	1250	818	912	1827	2130	5413	2493	7087
	969	1653	2360	3567	1603	2640	1060	6787
	2020	4257	2367	3840	870	6443	3230	8387
	1727	2567					2443	5707
Q1	**1039**	**1837**	**912**	**3567**	**830**	**1850**	**1315**	**3664**
Q2 (median)	**1488**	**2477**	**2360**	**3570**	**870**	**2640**	**1932**	**6247**
Q3	**1947**	**2789**	**2367**	**3840**	**1603**	**5413**	**2481**	**7012**

Table 27. Storage moduli (G'_0) for co-seeded W3110 and AP329 biofilms incubated with 10% (v/w) ultrapure water or a solution of interest. Pairs of values located in the same line correspond to biofilms grown in the same Petri dish.

Matrix composition	**Curli pEtN-cellulose (co-seeded)**							
Solution	**$AlCl_3$**	**Water**	**$FeCl_3$**	**Water**	**$ZnCl_2$**	**Water**	**$CaCl_2$**	**Water**
G'_0 (Pa)	8263	7487	4540	9743	6423	15733	2890	19033
	16867	12100	2717	13833	8297	12500	8750	13233
	22300	20733	8023	20433	14500	17033	4700	16067
	24867	13667	25700	19400	7617	11367	5157	20500
	28167	27333	16200	18833	16933	21200	14867	13733
	19267	19500	21767	26167	5650	29200	3073	17900
Q1	**17467**	**12492**	**5411**	**15083**	**6722**	**13308**	**3480**	**14317**
Q2 (median)	**20783**	**16583**	**12112**	**19117**	**7957**	**16383**	**4928**	**16983**
Q3	**24225**	**20425**	**20375**	**20175**	**12949**	**20158**	**7852**	**18750**

Table 28. Loss moduli (G''_0) for co-seeded W3110 and AP329 biofilms incubated with 10% (v/w) ultrapure water or a solution of interest. Pairs of values located in the same line correspond to biofilms grown in the same Petri dish.

Matrix composition	**Curli pEtN-cellulose (co-seeded)**							
Solution	**$AlCl_3$**	**Water**	**$FeCl_3$**	**Water**	**$ZnCl_2$**	**Water**	**$CaCl_2$**	**Water**
G''_0 (Pa)	1133	900	679	1277	1060	2183	456	2570
	2433	1583	327	1687	1597	1673	1697	1747
	3807	2557	1227	2817	2847	2357	789	1973
	3557	1767	3770	2833	1410	1457	826	2860
	4257	3537	2693	2520	3277	2663	2950	1667
	2877	2480	3163	3370	927	3600	472	2167
Q1	**2544**	**1629**	**816**	**1895**	**1148**	**1801**	**551**	**1803**
Q2 (median)	**3217**	**2123**	**1960**	**2668**	**1503**	**2270**	**807**	**2070**
Q3	**3744**	**2537**	**3046**	**2829**	**2534**	**2587**	**1479**	**2469**

12.1.6. Counter ion condensation in pEtN-cellulose

To assess whether counter ion condensation could occur along the pEtN-cellulose fibres, the following Manning's criterion was calculated, taking into account the valence of the cation possibly involved. Counter ion condensation occurs when:

$$\xi = \frac{l_B}{b} > \xi_{crit} = 1/z \quad ,^{190,191}$$

where *z* is the valence of the counter ion, *b* the length per unit of charge (i.e. the distance between two neighbouring charges along the pEtN-cellulose chain) and l_B the Bjerrum length with

$$l_B = \frac{e^2}{4\pi\varepsilon_0\varepsilon k_B T} \cong 0.712\ nm \text{ in water at 20°C,}$$

and *e* the elementary charge, ε the relative permittivity, ε_0 the electric constant, k_B the Boltzmann constant and *T* the temperature.

The distance between two glucose units is 0.515 nm (data for carboxymethycellulose),[192] and half of the glucoses are substituted on their carbon 6 with phosphoethanolamine.[16] Considering one negative charge per phosphate, the following relationship is obtained for bivalent and trivalent ions:

$$b = 2 * 0.515 = 1.030\ nm \text{ and } \xi = \frac{0.712}{1.030} = 0.691 > \frac{1}{z}$$

This means that counter ion condensation along the pEtN-cellulose chain can take place for both bivalent and trivalent ions.

Table 29. Quantities required for computing Manning's criterion in the case of pEtN-cellulose.

Symbol	Quantity	Value
e	Elementary charge	1.602 10^{-19} C
ε_0	Vacuum permittivity	8.854 10^{-12} F.m^{-1}
ε	Relative permittivity (water, 20°C)	80.08
k_B	Boltzmann constant	1.381 J.K^{-1}
T	Absolute temperature	293.15 K
b	Axial distance per elementary charge	1.030 nm

12.2. Contribution of the biofilm macroscopic architecture to its viscoelastic properties

12.2.1. Calculation of the median error by bootstrapping

From the original sample X of size N, N elements were randomly chosen with replacement to create a boostrapped sample Y of size N. The median m of Y was calculated and stored in the vector M of size 1000. The previous steps were repeated 1000 times, whence the length of M.

The standard deviation of M was taken as the error associated to the median of X.

In the case of N=3, rather than 1000 iterations, the medians were calculated for the exact 27 (3^3) combinations instead.

12.3. Molecular interactions between metal cations and the biofilm matrix

12.3.1. Figures

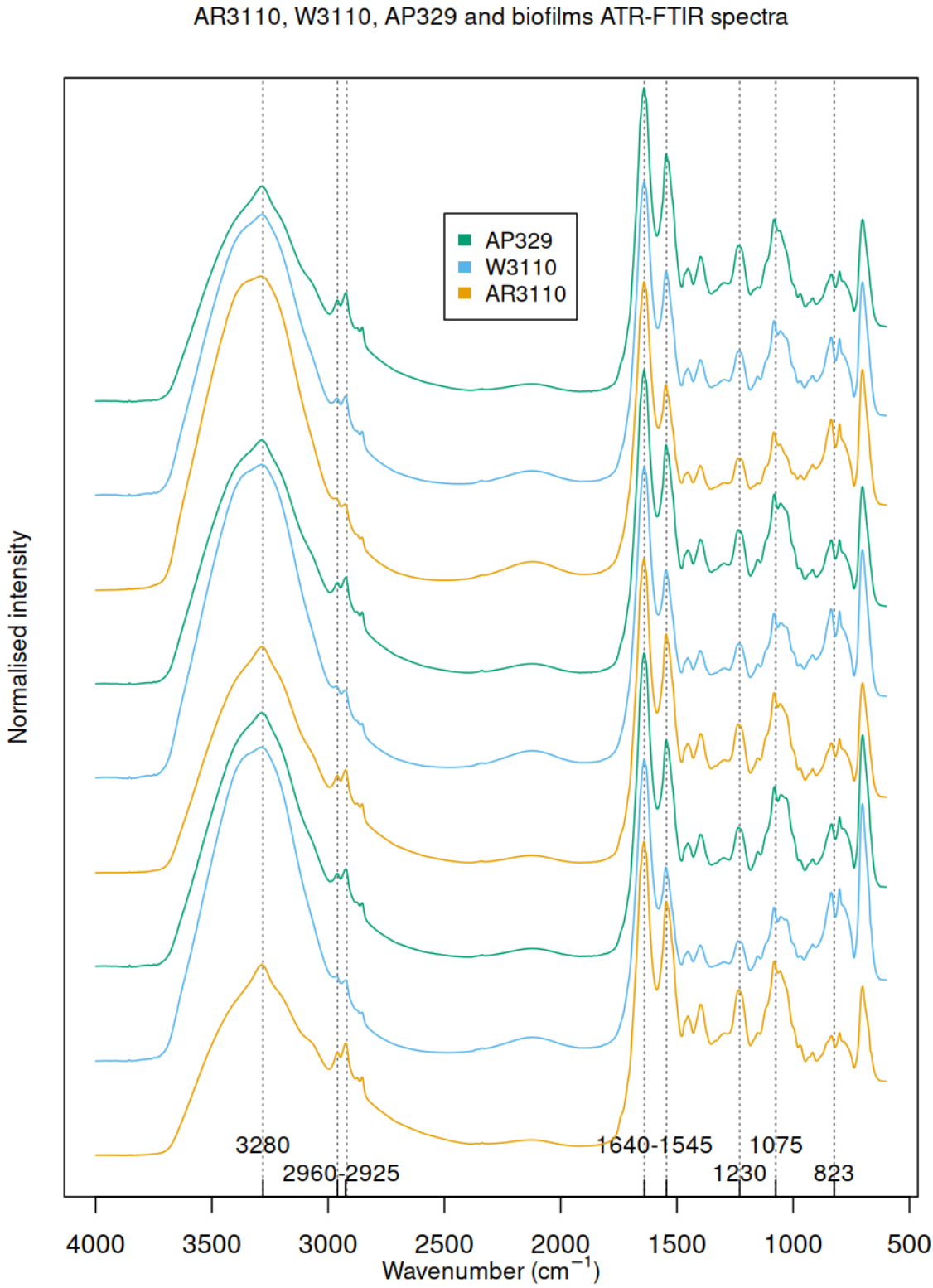

Figure 26. ATR-FTIR spectra of biofilms formed by three *E. coli* strains after homogenization with 10% (v/w) ultrapure water. AR3110 produces both pEtN-cellulose and curli amyloid fibres. W3110 produces only curli amyloid fibres. AP329 produces only pEtN-cellulose fibres. All replicates included.

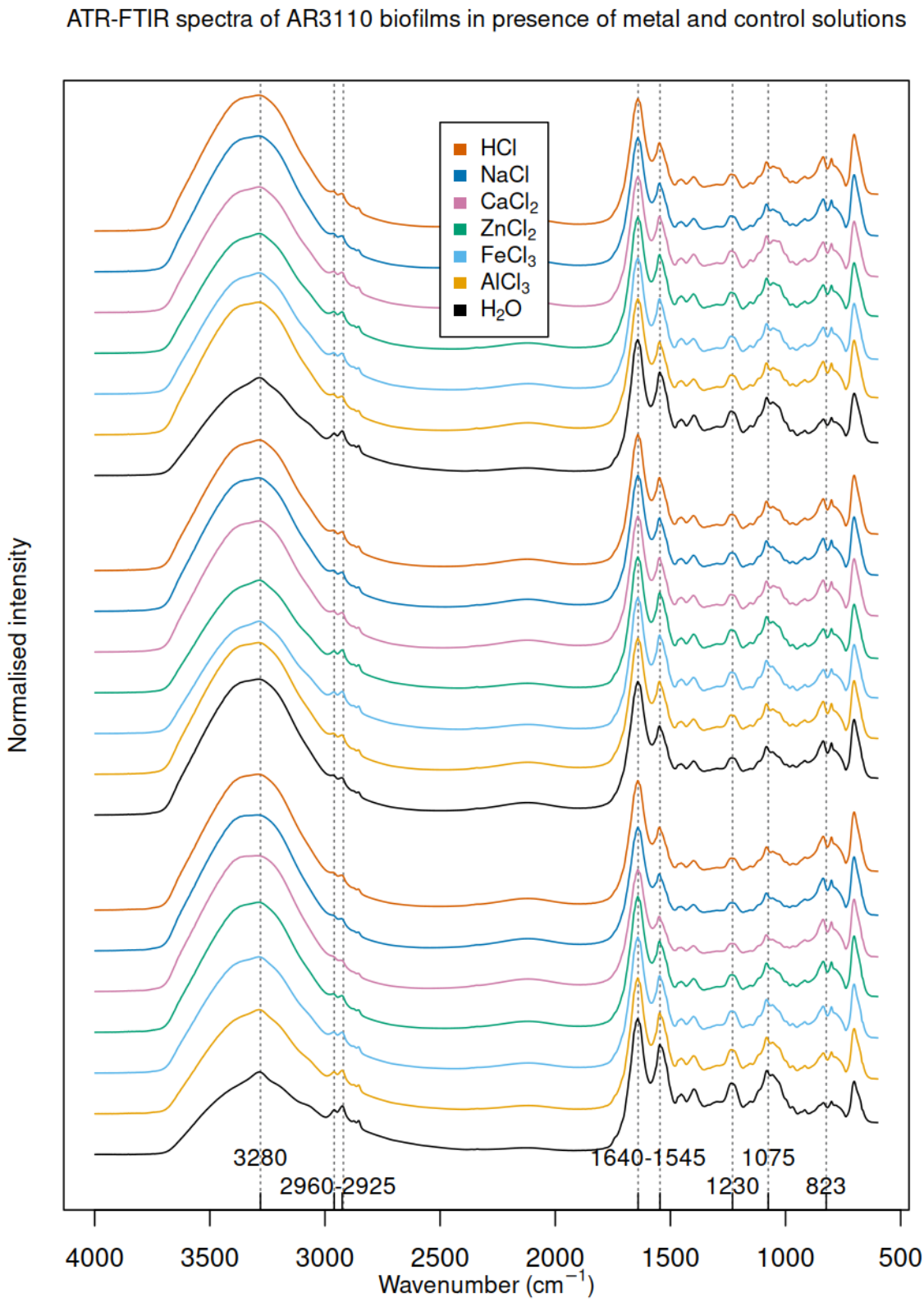

Figure 27. ATR-FTIR spectra of biofilms formed by *E. coli* AR3110 strain after homogenization with 10% (v/w) ultrapure water, $AlCl_3$, $FeCl_3$, $ZnCl_2$, $CaCl_2$, NaCl and HCl. AR3110 produces both pEtN-cellulose and curli amyloid fibres. The three vertical groups were measured on the same day. Dotted lines are plotted to facilitate the identification of possible shifts and correspond to the peaks introduced in Figure 13 and Table 14.

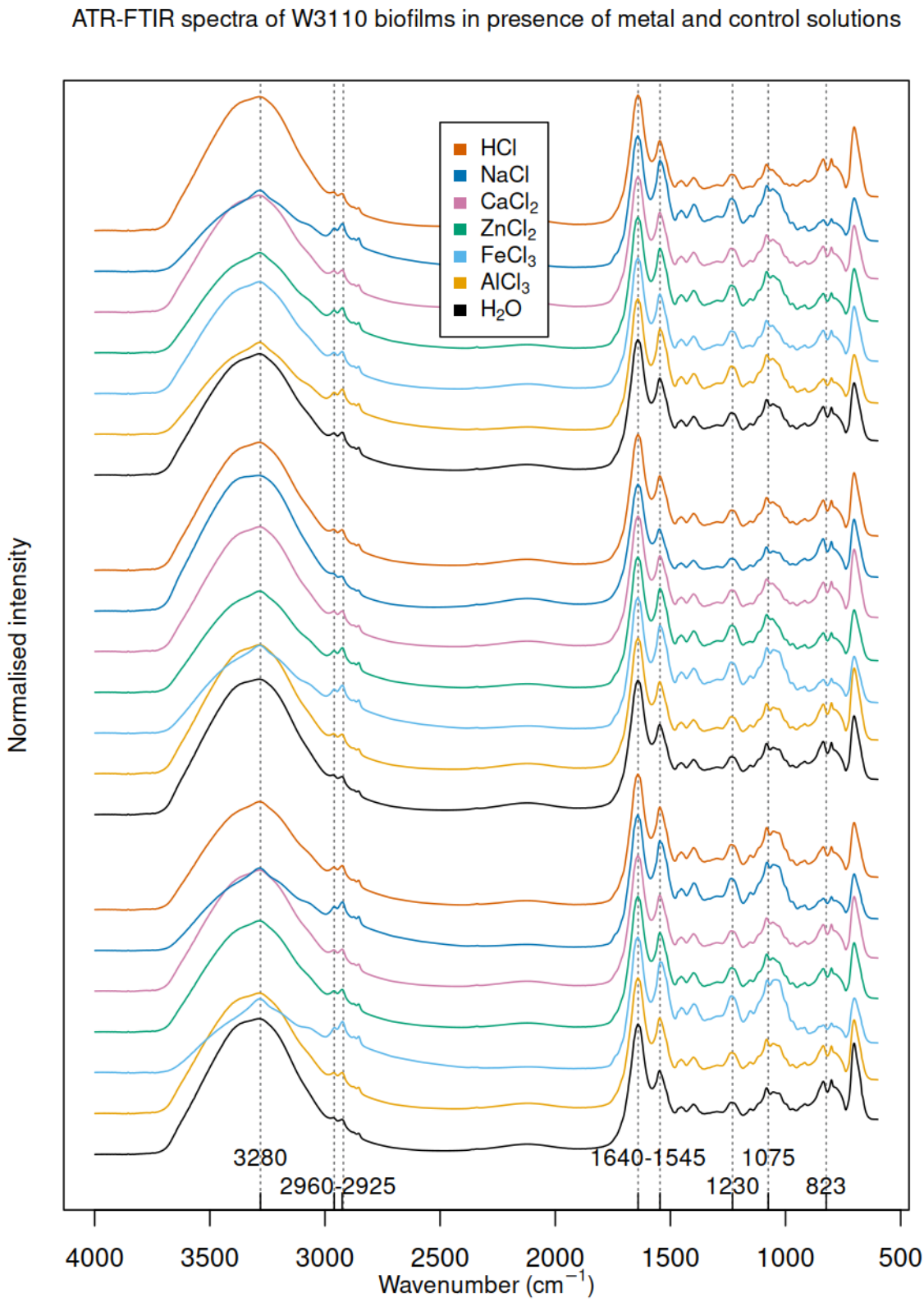

Figure 28. ATR-FTIR spectra of biofilms formed by *E. coli* W3110 strain after homogenization with 10% (v/w) ultrapure water, $AlCl_3$, $FeCl_3$, $ZnCl_2$, $CaCl_2$, NaCl and HCl. W3110 produces only curli amyloid fibres. The three vertical groups were measured on the same day. Dotted lines are plotted to facilitate the identification of possible shifts and correspond to the peaks introduced in Figure 13 and Table 14.

Table 30. Intensity ratio of the peaks at 2920 and 2960 cm^{-1} in the spectra of W3110 biofilms in presence of different solutions. Conditions for which the peak at 2960 cm^{-1} is higher are in bold.

Solution	Peak ratios: 2920 cm^{-1}/2960 cm^{-1}		
H_2O	**0.95325**	**0.95769**	1.01992
$AlCl_3$	1.00377	**0.98877**	1.07400
$FeCl_3$	1.13380	1.09251	1.02318
$ZnCl_2$	1.03339	1.07181	1.05861
$CaCl_2$	1.01648	1.0072	1.01709
NaCl	1.10629	**0.91927**	1.10429
HCl	1.03484	**0.98973**	**0.96336**

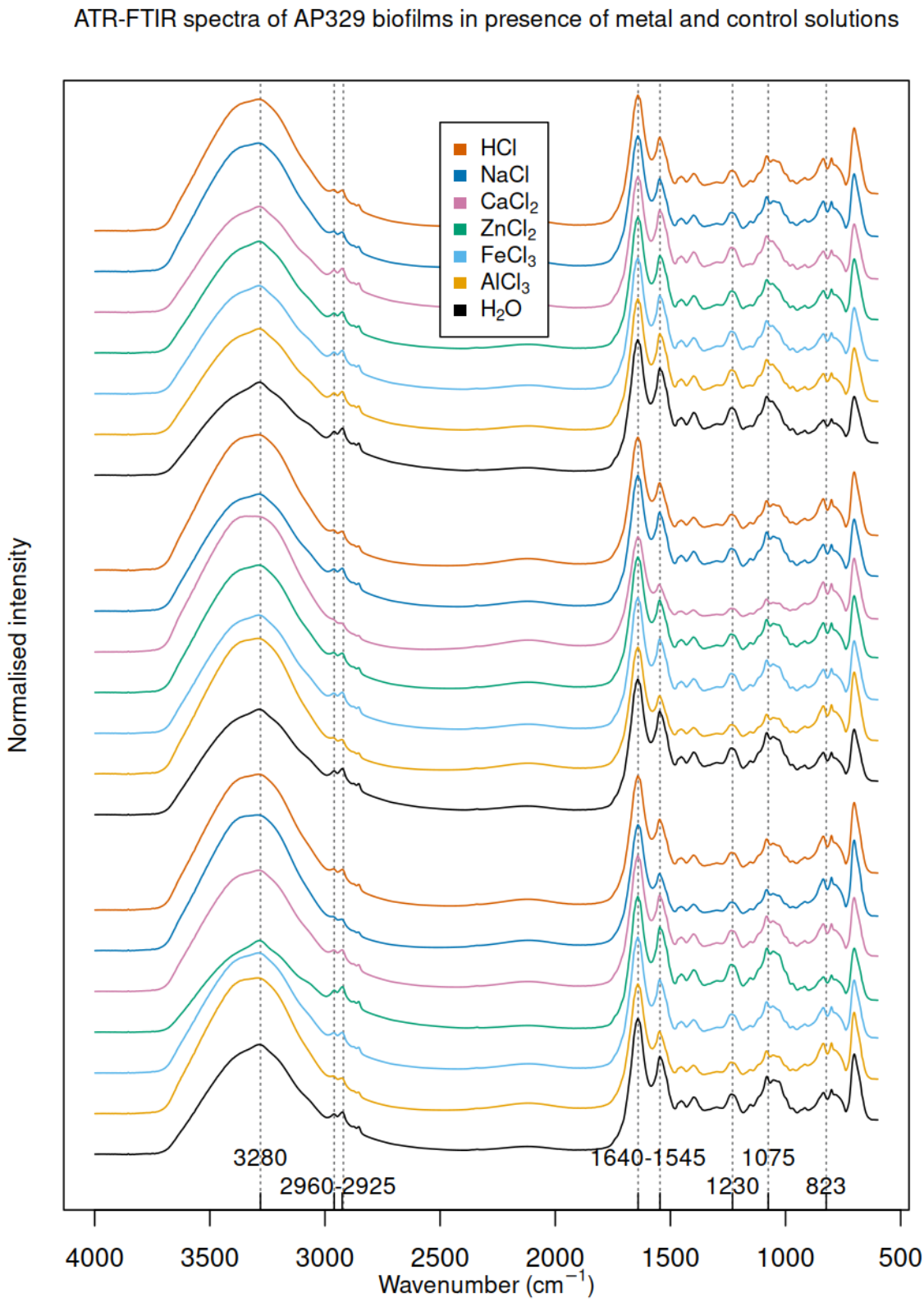

Figure 29. ATR-FTIR spectra of biofilms formed by the *E. coli* AP329 strain after homogenization with 10% (v/w) ultrapure water, $AlCl_3$, $FeCl_3$, $ZnCl_2$, $CaCl_2$, NaCl and HCl. AP329 produces only pEtN-cellulose. The three vertical groups were measured on the same day. Dotted lines are plotted to facilitate the identification of possible shifts and correspond to the peaks introduced in Figure 13 and Table 14.

12.3.2. Metal to CsgA monomer molar ratio in the FTIR experiments

Biofilm spectra

The final concentration of the metal salt solutions after mixing with the biofilm is 20 mM. Assuming a density of 1, this corresponds to 20 mmol of metal per kg of wet biofilm or 20 µmol of metal per g of wet biofilm. Assuming a water percentage of the biofilm equal to 78%[171], this means that 20 µmol of metal was added per 0.22 g of dry biofilm. Knowing curli mass percentage in the dry biofilm (0.146%[150]) and CsgA molar mass (15049 g/mol), this corresponds to a molar ratio 937:1 (metal:CsgA).

Curli fibre spectra

The approximate concentration of curli fibres in suspension is known in terms of CsgA monomers and corresponds to 425 mM. The metal salt solutions were diluted to 400 µM and both were mixed in a 1:4 ratio (see Materials and Methods). This corresponds to 1600/425=3.76 times more Fe(III) than CsgA (mol/mol).

12.3.3. Curli fibres secondary structure: two samples Wilcoxon signed rank test

Table 31. β-sheets: p-values of the two samples Wilcoxon signed rank test.

	H_2O	$AlCl_3$	$FeCl_3$	$ZnCl_2$	$CaCl_2$
H_2O	1	0.8	0.2	0.2	0.133
$AlCl_3$		1	0.4	0.2	0.229
$FeCl_3$			1	0.7	0.857
$ZnCl_2$				1	0.4
$CaCl_2$					1

Table 32. Alpha-helices and random coils: p-values of the two samples Wilcoxon signed rank test.

	H_2O	$AlCl_3$	$FeCl_3$	$ZnCl_2$	$CaCl_2$
H_2O	1	0.2	0.2	0.2	0.133
$AlCl_3$		1	0.4	0.7	0.229
$FeCl_3$			1	0.4	0.057
$ZnCl_2$				1	0.857
$CaCl_2$					1

Table 33. Turns: p-values of the two samples Wilcoxon signed rank test

	H_2O	$AlCl_3$	$FeCl_3$	$ZnCl_2$	$CaCl_2$
H_2O	1	0.4	1	1	0.533
$AlCl_3$		1	0.1	0.7	0.857
$FeCl_3$			1	0.7	0.057
$ZnCl_2$				1	0.629
$CaCl_2$					1

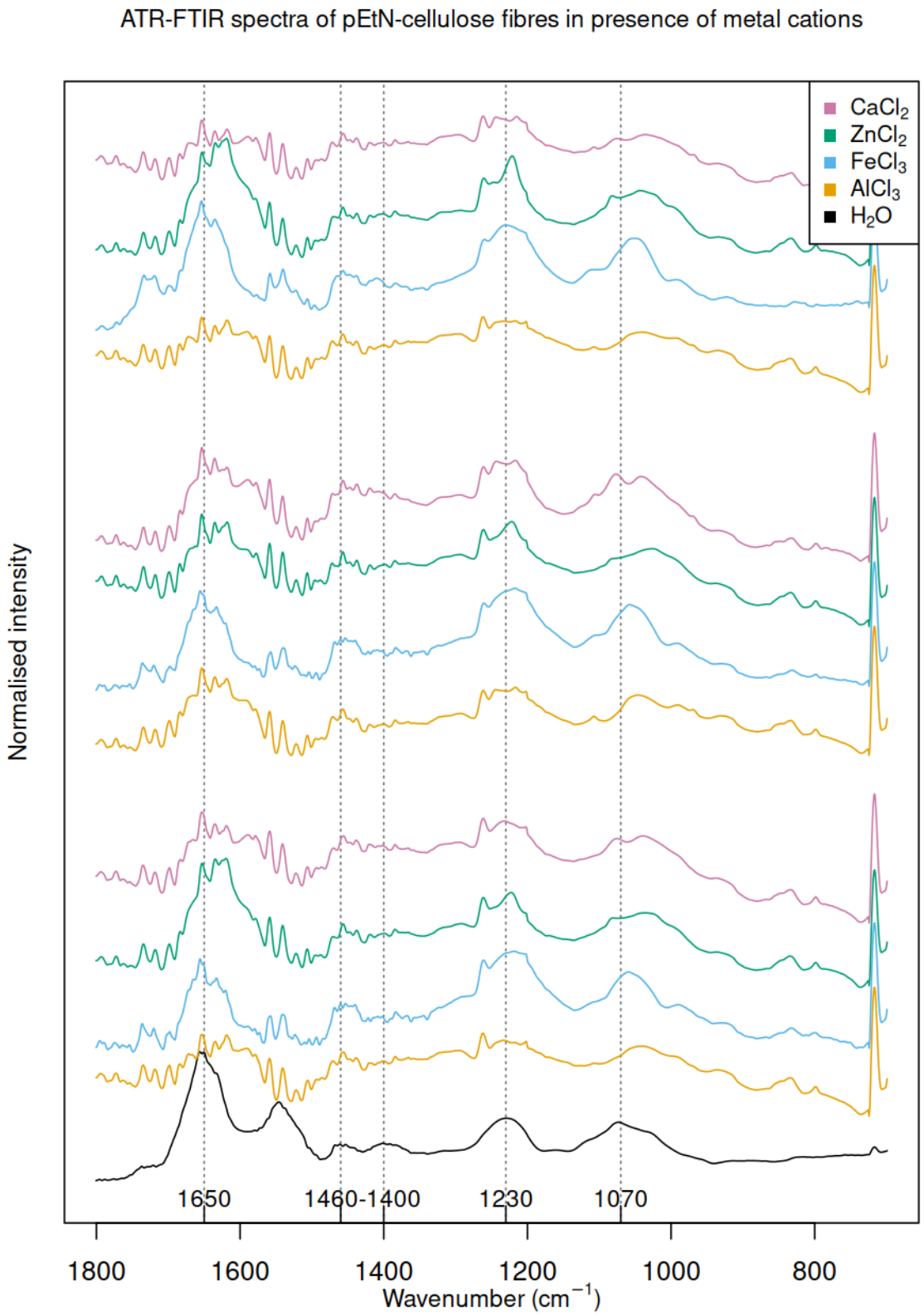

Figure 30. ATR-FTIR spectrum of purified pEtN-cellulose fibres in presence of ultrapure water, $AlCl_3$, $FeCl_3$, $ZnCl_2$ and $CaCl_2$. Dotted lines are plotted to facilitate the identification of possible shifts. The corresponding functional groups are identified in Figure 20 and Table 16.